

Cavity Beam Position Monitor for the
TESLA-cryomodule.
Cross-Talk minimization

Vorgelegt von
Dipl.-Ing Vahagn Sargsyan
aus Jerewan

Von der Fakultät IV
-Elektrotechnik und Informatik- der
Technischen Universität Berlin
zur Erlangung des akademischen Grades
Doktor der Ingenieurwissenschaften
- Dr.-Ing -

genehmigte Dissertation
Promotionsausschuss:

Vorsitzender: Prof Dr.-Ing H. Klar
Berichter: Prof Dr.-Ing H. Henke
Berichter: Prof Dr.-Ing G. Mönich

Tag der wissenschaftlichen Aussprache: 16.10.2003

D 83

Berlin 2003

Contents

| | |
|---|-----------|
| Zusammenfassung | 9 |
| Introduction | 1 |
| 1 The TESLA cryomodule | 6 |
| 2 Survey of the BPMs | 11 |
| 2.1 Pickup BPMs | 13 |
| 2.1.1 Stripline BPM | 15 |
| 2.2 Cylindrical Pill-box cavity BPM | 21 |
| 2.2.1 Shunt impedances of the pill-box cavity without a beam-pipe | 26 |
| 2.2.2 Magnetic and electric coupling of the pill-box cavity without a beam-pipe | 29 |
| 2.2.3 Linearity of the dipole mode | 39 |
| 2.2.4 Damping time of the cavity and the distance between bunches | 40 |
| 2.2.5 Cutoff frequencies of the beam-pipe | 42 |
| 3 Cross-talk problem in pill-box cavity BPMs | 43 |
| 3.1 Cavity without coupling antennas | 43 |
| 3.1.1 Cavity with four coupling antennas | 44 |
| 3.1.2 Reality | 45 |
| 3.1.3 Solution | 47 |
| 3.2 Cross-Talk calibration | 50 |
| 3.3 Perturbation of cavity walls | 54 |
| 4 The Prototype | 58 |
| 4.1 The pick-up station of the prototype | 58 |
| 4.1.1 Theoretical evaluation of the signals coupled at the dipole mode frequency | 62 |

| | | |
|-------|--|------------|
| 4.1.2 | Estimation of the prototype absolute resolution | 69 |
| 4.1.3 | Frequency scan and Q_L measurement of the cavity . . | 72 |
| 4.1.4 | Q_0 - measurements | 73 |
| 4.1.5 | Cross-talk measurement | 74 |
| 4.1.6 | Power dissipation caused by the resonating modes of the BPM | 76 |
| 4.1.7 | Test of leakage factor | 77 |
| 4.2 | Electronics | 79 |
| 4.2.1 | Electronics Components | 81 |
| 4.2.2 | Electronics test measurements | 85 |
| 4.3 | Laboratory test of the BPM | 88 |
| 4.3.1 | Alternative electronics | 91 |
| | Summary | 93 |
| | Acknowledgments | 95 |
| | Appendix A: Technical design of the cavity; part I | 96 |
| | Appendix B: Technical design of the cavity; part II | 97 |
| | Appendix C: Technical design of the coupling antenna | 98 |
| | Appendix D: The prototype cavity simulating GdfidL code | 99 |
| | Bibliography | 103 |

List of Figures

| | | |
|------|--|----|
| 1 | TESLA electron-positron linear collider | 1 |
| 2 | Beam accelerating module | 2 |
| 1.1 | Propagation of a photon in a TESLA cavity | 7 |
| 1.2 | Photon density distribution through a TESLA accelerating module | 8 |
| 1.3 | Energy loss within the cryomodule as a function of the BPM conductivity | 9 |
| 2.1 | BPM architecture | 11 |
| 2.2 | a: Electric field of a charged particle at rest. b: Electromagnetic fields of a relativistic charged particle ($\gamma \gg 1$) | 13 |
| 2.3 | a: Beam pipe configuration for application of Faraday's Law. b: Beam going off center through the beam pipe. The dark lines on both sides are the pickup electrodes. | 15 |
| 2.4 | Difference in intercepted image current between the two electrodes shown in figure 2.3,b versus actual beam displacement | 15 |
| 2.5 | Cross-section of a stripline pick-up station and horizontal view of one electrode | 16 |
| 2.6 | Operation principle of the stripline monitor | 17 |
| 2.7 | Cylindrical pick-up station | 21 |
| 2.8 | TM_{110} -mode pattern in cavity cross-section; the black spot shows the position of the bunch | 22 |
| 2.9 | Voltage along z axis of the TM_{110} -mode depending on the displacement x [m] | 22 |
| 2.10 | a: electric coupling, b: magnetic coupling, c: electro-magnetic coupling | 24 |
| 2.11 | Voltages of the first and second monopole modes compared with the TM_{110} dipole mode | 25 |
| 2.12 | a: Cross-section of the cavity without a beam-pipe; b: Electrical field of the dipole mode | 26 |

| | | |
|------|---|----|
| 2.13 | a: Cross-section of the cavity without a beam-pipe; b: Electric field of the first monopole mode | 28 |
| 2.14 | a: Cross-section of the cavity without a beam-pipe; b: Maximums of the electric field of the second monopole mode | 28 |
| 2.15 | a: TM_{010} mode pattern in the cavity without a beam-pipe. Blue point shows the maximum of electric field, red circle shows maximum of magnetic field; b: Magnetic field of the first monopole mode TM_{010} | 30 |
| 2.16 | The cavity coupled by loop | 30 |
| 2.17 | The cavity coupled by pin-antenna: The blue full lines are electrical flux, dashed blue lines show wall current of TM_{010} mode inside the cavity with radius b | 36 |
| 2.18 | The top view on the cavity with the coupling pin-antenna | 37 |
| 2.19 | Beam-pipe and pill-box cavity | 39 |
| 2.20 | TESLA beam | 41 |
| 2.21 | a: The cross-section of the beam-pipe with E field of the TE_{11} wave; b: the cross-section of the beam-pipe with E field of the TM_{01} wave | 42 |
| 3.1 | The cut of cylindrical cavity with small ellipticity and magnetic fields of two excited dipole modes. Their polarizations are perpendicular to each other. The black spot is at the position of the beam | 44 |
| 3.2 | The possible polarizations of the dipole modes in a perfectly symmetrical cavity with four antennas. The small four black spots are the coupling antennas, the bigger one is the beam: a) the dipole mode polarizations are matched with coupling antennas axis. b) the dipole mode polarizations and coupling antennas axes have $\pi/4$ mismatch. | 45 |
| 3.3 | Various locations of the major axis of the ellipse. | 46 |
| 3.4 | Forced ellipticity with desired orientation of the axis | 47 |
| 3.5 | The first dipole mode polarized in y direction | 48 |
| 3.6 | The second dipole mode polarized in x polarization | 48 |
| 3.7 | Layout of the cross-talk measurement | 49 |
| 3.8 | Pill-box cavity with negligible ellipticity: blue and green parts illustrate electric field maximums of dipole modes in x and y directions respectively. The four black spots represent four coupling antennas, a dashed bigger circle shows the displacement of the bunch | 50 |

| | | |
|------|--|----|
| 3.9 | The same pill-box cavity as in figure 3.8 but the antenna 1 once shifted to the antenna 4 a), and once it is shifted to the antenna 2 b) | 51 |
| 3.10 | By purpose shifted antennas | 53 |
| 3.11 | The pick-up station together with the hybrids | 53 |
| 3.12 | a: Original cavity; b: perturbed cavity | 54 |
| 3.13 | Unperturbed pill-box cavity | 56 |
| 3.14 | The coupling antenna | 57 |
| 4.1 | Prototype of the pick-up station with four symmetrically arranged feed-throughs | 59 |
| 4.2 | One of the four coupling antennas | 60 |
| 4.3 | Two parts of the antenna | 60 |
| 4.4 | The interior of the cavity | 61 |
| 4.5 | Photon(high order mode from the accelerating module) interactions in the cavity | 61 |
| 4.6 | Cross-section of the cavity with two rectangular recesses | 61 |
| 4.7 | The electric field of TM_{110} mode calculated by GdfidL | 63 |
| 4.8 | The voltage of the TM_{110} mode along the x axis; ($E_z e^{i\omega \frac{z}{c}}$ integrated over z | 64 |
| 4.9 | The electric field of TM_{010} mode calculated by GdfidL | 64 |
| 4.10 | The voltage of the TM_{010} mode along the x axis; ($E_z e^{i\omega \frac{z}{c}}$ integrated over z) | 65 |
| 4.11 | Resonant curve of some resonating contour R , L , C with resonant frequency f_0 and quality factor Q | 66 |
| 4.12 | The electric field of TM_{020} mode calculated by GdfidL | 67 |
| 4.13 | The voltage of the TM_{020} mode along the x axis; ($E_z e^{i\omega \frac{z}{c}}$ integrated over z | 67 |
| 4.14 | Leakage factor of the second monopole mode into the dipole mode frequency | 68 |
| 4.15 | Layout of the hybrid test measurement | 70 |
| 4.16 | Result of the hybrid Σ port measurement | 70 |
| 4.17 | Result of the hybrid Δ port measurement | 71 |
| 4.18 | Resonating modes | 72 |
| 4.19 | Frequency scan measurement | 72 |
| 4.20 | Q_0 -measurement | 74 |
| 4.21 | Schematic illustration of the cross-talk measurement | 75 |
| 4.22 | Signal level in [dB] against frequency. The signal level is graded by 10 dB. The reference 0 dB-line is the middle one of the plots | 75 |

| | |
|---|----|
| 4.23 Relations between bunches, beams and repetition frequency, see table 1 | 76 |
| 4.24 Q_0 -measurement | 78 |
| 4.25 Electronics box | 79 |
| 4.26 The whole electronics circuit for new pill-box BPM; bunch charge and position measurement | 80 |
| 4.27 Photo of the open electronics box | 80 |
| 4.28 Test plot of 8 mixers | 81 |
| 4.29 180° hybrid | 82 |
| 4.30 Test measurement of the bandpass filter | 83 |
| 4.31 Components of the lowpass filter | 84 |
| 4.32 Central frequency and band width of the resonating circuit R, L, C | 85 |
| 4.33 Layout of electronics test measurement | 86 |
| 4.34 Signal diagram of I_x -channel | 86 |
| 4.35 Layout of the complete BPM test measurement | 88 |
| 4.36 Resolution test-measurement with the electronics | 89 |
| 4.37 The BPM sensitivity | 89 |
| 4.38 Resolution plot of the BPM | 90 |
| 4.39 Alternative electronics box | 91 |
| 4.40 The signal after the down-conversion | 92 |

List of Tables

| | | |
|------|---|----|
| 1 | Some parameters of the beam and TESLA structure | 2 |
| 1.1 | Monopole mode single bunch losses in one cryomodule | 6 |
| 1.2 | Elements of TESLA accelerating module | 7 |
| 1.3 | Energy losses in the TESLA accelerating module | 8 |
| 1.4 | Energy dissipation values in the TESLA accelerating module depending on the BPM conductivity | 9 |
| 2.1 | Test of the theoretical computation of the coupling factor | 32 |
| 2.2 | Test of the theoretical computation of the coupling factor of the dipole mode | 34 |
| 2.3 | Test of the theoretical computations of pin-antenna coupling | 37 |
| 2.4 | Test of the of theoretical computations of the electric coupling of the dipole mode | 38 |
| 3.1 | Prototype parameters and cross-talk isolation; frequency difference refers to figure 3.2 and figure 3.4, respectively | 49 |
| 3.2 | Δf computed by perturbation theory and GdfidL | 56 |
| 3.3 | Perturbation caused by couplig antennas | 57 |
| 4.1 | Dimensions of the cavity and material parameters | 58 |
| 4.2 | Sensitivity of the different mechanical parameters | 62 |
| 4.3 | Calculated data of the modes of the prototype | 63 |
| 4.4 | Voltages at the dipole mode frequency for a 10 μm offset | 69 |
| 4.5 | Voltages at dipole mode frequency 1.5 GHz after the hybrid | 70 |
| 4.6 | Data of frequency scan | 73 |
| 4.7 | Data of Q_0 -measurement | 74 |
| 4.8 | Signals from the pick-up station | 79 |
| 4.9 | Power values on the hybrid inputs and outputs at f_{110} | 83 |
| 4.10 | Results of the electronics channel test measurements | 87 |

Zusammenfassung

Der zukünftige, etwa 33 km lange e^+e^- Linearbeschleuniger TESLA hat fundamentale Bedeutung für die Entwicklung der Teilchenphysik, Festkörperphysik, Chemie, Materialwissenschaften und Biologie. TESLA benötigt zum Betrieb viele Beam-Position-Monitore (BPMs), um die Elektronenstrahlage immer unter Kontrolle zu haben. Ein grosser Teil davon (1752 Stück) soll in einer 2 K kalten kryogenischen Umgebung betrieben werden.

Diese BPMs sollen folgende Anforderungen erfüllen:

- Die erste Anforderung kommt durch die grosse Anzahl (1752 Stück) der BPMs. **Das Design und dementsprechend die Fertigung soll möglichst einfach sein.**
- Die zweite Anforderung folgt aus der 2 K kryogenischen Umgebung. Es ist teuer, Wärme aus einer solchen Umgebung abzuführen. 2.5 Watt Energieverluste pro Kryomodul wurden in DESY-Hamburg berechnet, davon gehen 1.1 Watt auf den BPM. Die zweite Anforderung ist also, dass **der BPM wesentlich weniger als 1.1 Watt Energieverluste pro Kryomodule verursachen soll.**
- Die dritte Anforderung betrifft die Auflösung. **Die Elektronstrahlauflösung soll nicht schlechter als 10 μm sein.**
- Es gibt Übersprechungseffekte innerhalb eines BPMs, welche die vertikalen und horizontalen Signalen verkoppeln. Daraus folgt, eine weitere Anforderung: **Das Übersprechen soll möglichst klein und stabil sein.**

Zwei BPM Arten wurden durchstudiert. Ausgewählt wurde eine pill-box Kavität. Ihr Inneres ist verkupfert, womit die Energieverluste von 1.1 W auf 0.46 W sinken. Zusätzlich wurde darauf geachtet, dass die resonanten Moden der Kavität schnell genug abklingen, um Bunch zu Bunch Messungen durchführen zu können.

Theoretische Rechnungen haben gezeigt, dass der BPM eine absolute Auflösung von 78.6 nm hat. Aber die Interpretation der Labormessungen zeigte, dass der Prototyp 371 nm Auflösung hat.

Der Test des Prototyps unter realen Bedingungen im Linearbeschleuniger ELBE in Rossendorf ist für den Winter 2003/2004 geplant.

Die Konstruktion des Prototyps ist unkompliziert. Es hat grösstenteils radiale Symmetrie, was seine Fertigung präziser und einfacher macht. Das Übersprechen wurde durch zusätzliche Konstruktion minimiert und stabilisiert. Dafür wurden durch Elektro-Erosion zwei Ausbuchtungen ins Innere der Kavität eingebracht.

Im Laufe der Arbeit ist auch eine neue Idee für die Auswerteelektronik entstanden. Die Elektronik ist gebaut, aber noch nicht getestet. Falls die Elektronik wie beabsichtigt funktioniert, kann auf eine zusätzliche Kavität zur Erzeugung des Referenzsignals verzichtet werden.

Introduction

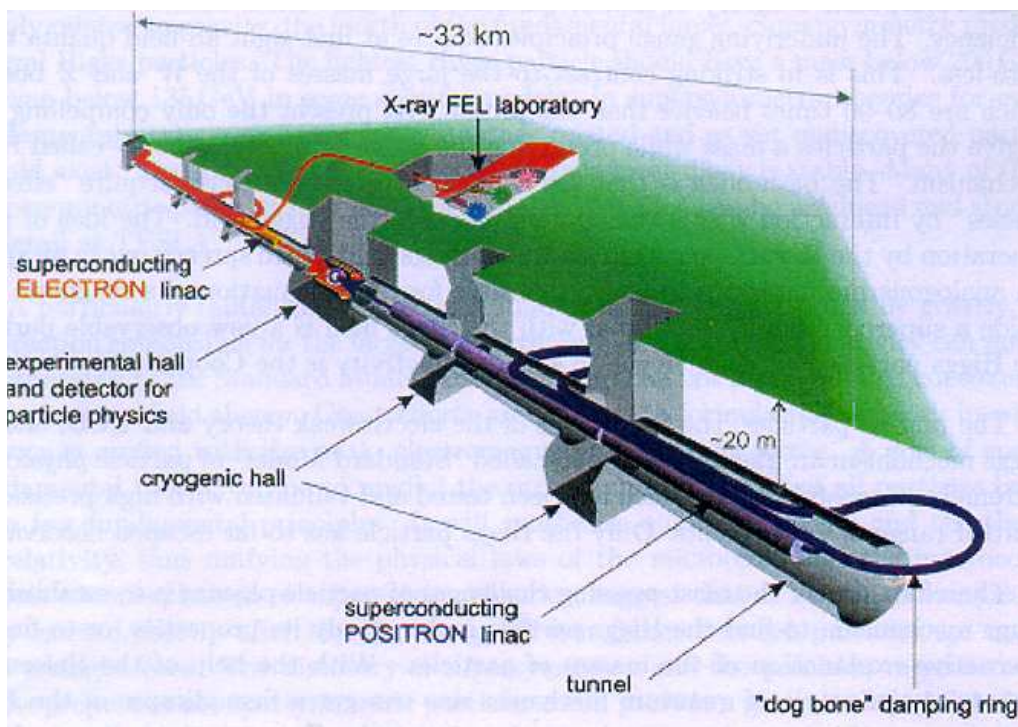


Figure 1: TESLA electron-positron linear collider

To reach higher energies in accelerators linear colliders are more promising than synchrotrons. The main point is that in case of synchrotrons due to synchrotron radiation we have always energy losses from the beam [1]. As an example SLAC (Stanford Linear Collider) shows how effective linacs are [2].

These ideas brought scientists to the TESLA project (TeV Electron Superconducting Linear Accelerator) and TESLA-Collaboration [3]. TESLA is a ~ 33 km long e^+e^- linear collider with 500 GeV energy, (Figure 1). Some parameters of the beam and TESLA structure are listed in the table below.

| TESLA | |
|-----------------------------------|------------------------------------|
| Pulse repetition rate | $f_{rep} = 5$ Hz |
| Beam pulse length | $T_p = 950$ μ s (285 km) |
| No. of bunches per pulse | $n_b = 2820$ |
| Bunch spacing | $\Delta t_b = 337$ ns (101.1 m) |
| Charge per bunch | 3.2 nC ($N_e = 2 \cdot 10^{10}$) |
| RF frequency | $f_{rf} = 1.3$ GHz |
| Number of 9-cell cavities | 21024 |
| No. of 9-cell cavities per module | 12 |
| No. of accelerating modules | 1752 |
| Bunch length at interaction point | $\sigma_z = 0.3$ mm |

Table 1: Some parameters of the beam and TESLA structure

TESLA is of fundamental importance for the future development of particle physics. TESLA X-ray laser laboratory provides unique research possibilities for condensed matter physics, chemistry, material science and for structural biology.

The fundamental difference between TESLA and other linear accelerator designs is the choice of a super-conducting structure. The advantages of super-conducting technology are significant and the machine performance potential is unrivalled by other concepts [3].

Motivation

TESLA consists of 1752 accelerating modules (see table 1). Each TESLA accelerating module has a BPM (Beam Position Monitor) in the middle:

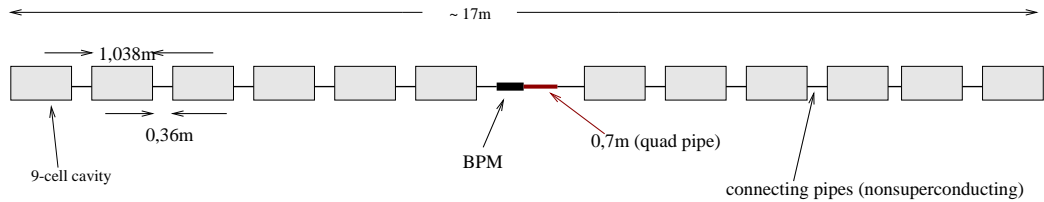


Figure 2: Beam accelerating module

To provide super-conductivity 9-cell Niobium accelerating cavities should be cooled down to 2 K. The Beam-accelerating module (Figure 2) is put in

cryogenic environment.

The fact that a BPM should be in 2K cryogenic environment leads to an extra condition: It is expensive to keep such an environment, and any additional energy dissipation is not desired there.

Electromagnetic fields accompanying the TESLA-beam interact with inhomogeneities of the module and high order modes are excited. These high order modes interact with the walls of the module and energy dissipation takes place. The computations of energy dissipation in the module in case of pill-box cavity BPM from steel showed, that the energy dissipation on the walls of the BPM pick-up station are unacceptable high [4]. The dominant role for these energy dissipations play the interactions between high order modes (excited mostly due to inhomogeneities of 9-cell accelerating cavities) and the walls of the BPM. Hence,

- a new BPM for the TESLA cryomodule with sufficiently less energy dissipation than 1.1 W should be designed. This BPM should have a resolution not worse than 10 μm .

All cavity BPMs suffer from *cross-talk* effect. This effect is characterized by cross-talk isolation value in [dB]. It shows how good the signal corresponding to bunch displacement δx is isolated from the signal corresponding to the bunch displacement δy .

In case of pill-box cavity the cross-talk performance can be unstable. This fact makes the problem more complicated. For example cross-talk isolation could be getting worse after welding the beam-pipe to the cavity. Hence,

- the cross-talk performance in pill-box pick-up stations should be stabilized to its minimal value. In this paper we mark the cross-talk isolation with K.

Summary of achieved results

- A new BPM for the TESLA cryomodule with energy dissipation 2.39 times less than 1.1 W and with 371 nm resolution performance is designed, fabricated and tested.
- Cross-talk problem of pill-box cavity is observed. The solution for minimal and stable cross-talk performance is found.
- A new concept of cavity pill-box BPM electronics is proposed. Here we take the LO reference signal from the pill-box cavity itself. The construction of an extra cavity for the LO reference signal is not necessary any more.

Tools

The computer code GdfidL [5] is used for the prototype simulation and the computation of its parameters.

For laboratory test measurements computer code LabVIEW was used [6].

Perturbational and variational techniques are used to compute theoretically frequency changes in the structure due to small distortions.

A FORTRAN code was used for the processing of the measured data.

Organisation of the manuscript

The problem of energy dissipation in the TESLA accelerating cryomodule is discussed in chapter 1. The energy dissipates because of interactions between non-superconducting parts in the cryomodule and high order mode fields excited by the accelerating structures when the beam flies through. The part of this dissipation on the BPM walls is evaluated. The way to reduce it is proposed.

In chapter 2 operational principle of pickup BPMs is surveyed. BPMs are integrated parts of accelerators. As the name tells us, we need them to measure beam position in the beam-pipe. We need this to bring in opposite directions flying beams into collision at IP (Interaction Point, see figure 1, experimental hall). There are many types of BPMs, and which one to choose depends on the particular task and conditions.

Two different types of BPMs are also discussed in this chapter.

In chapter 3 the cross-talk problem in pill-box cavity BPM is discussed. A new design is invented to get minimal and stable cross-talk between signals corresponding to bunch x and y offset.

In chapter 4 the prototype is presented. This prototype overcomes the problem discussed in chapter 1. It contains also a new design discussed in chapter 3. Test measurements of the cavity and the electronics are presented. As a subsection to this chapter we present the new electronics concept, where the LO signal is taken from the cavity itself.

Further remarks

The obtained results satisfy requirements that we deal with. But there are some remarks worth to mention:

- During this work a new concept of electronics is designed, see subsection

4.3.1. For future steps we are going to test this new electronics.

- At the beginning of the next year the BPM will be tested in Rossendorf on the linear accelerator ELBE with a beam energy from 12 till 40 MeV [7].

Chapter 1

The TESLA cryomodule

The design of the cryomodules has been primarily driven by the need to reduce costs compared to existing superconducting cavity systems. The module described here is based on the 3-rd cryomodule generation of the TESLA Test Facility [8], [9]. Except for the length (≈ 17 m compared to 12 m for a TTF module), only minor modifications of the design have been made.

At present day superconducting cavity systems tend to have many separate cryogenic supply boxes and associated warm-to-cold transitions, which represent a significant fraction of the cost. The concept adopted here is to reduce this number significantly by having a single long continuous string of about 2.5 km - called a cryogenic unit - which is connected to one cryogenic supply box at the beginning and the end of the box. Long modules will be built consisting of twelve 9-cell cavities, a quadrupole, steering coils and a beam position monitor.

Because of cost any additional energy losses are not wanted in cryogenic environment.

The short bunches in TESLA excite HOM's (High Order Mode) in a very wide frequency range which will be absorbed in the structure walls and therefore contribute to the cryogenic losses. Table 1.1 shows the single bunch losses calculated from the monopole short range wake [10], [11], [12].

| | collider operation | FEL operation |
|----------------------|--------------------|---------------|
| total losses | 23.3 W | 14.2W |
| losses above 10 GHz | 12.7 W | 9.4 W |
| losses above 750 GHz | < 0.001 W | 0.5 W |

Table 1.1: Monopole mode single bunch losses in one cryomodule

Most losses occur at lower frequencies where the conductivity of the su-

perconducting surfaces is several orders higher than that of normal conducting walls. Part of this power is extracted by input- and HOM-couplers, but high frequency fields will propagate along the structure and will be reflected at normal and superconducting surfaces [13], [14], [15]. In order to reduce the losses at normal conducting surfaces at 2 K and 4 K, a special HOM absorber is foreseen which operates at 70 K, where the cooling efficiency is much higher.

In table 1.2 we list superconducting and normal conducting parts of the cryomodule:

| | | |
|------------------|------------------------------|------------------------------------|
| 9-cell cavity | length material amount | 1.038m Niobium(supercon.) 12 |
| connecting pipes | length material amount | 0.36m copper 12 |
| BPM | material amount | stainless steel 1 |
| Quad pipe | material amount | copper 1 |

Table 1.2: Elements of TESLA accelerating module

The propagation of these high order wake fields is described by a photon diffusion model [13]. Here the higher order modes (> 50 GHz) are considered as photons¹. The propagation of wake fields through the module is like diffusion of the photons.

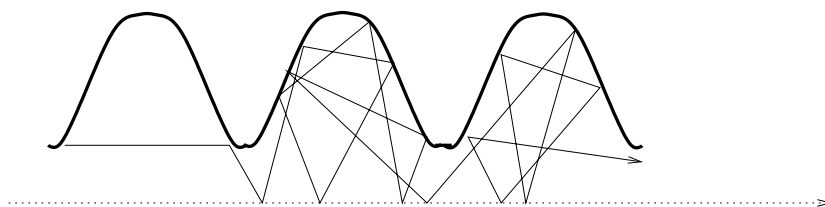


Figure 1.1: Propagation of a photon in a TESLA cavity

¹In case of $5\text{GHz} < f < 50\text{GHz}$ a safety margin is taken into account as the photon model is not appropriate.

Inhomogeneities in the module make photons (wakefields) propagation difficult and complicated (Figure 1.1). They reflect back and forth many times, and as a result, following photon density distribution takes place, see figure 1.2 [4].

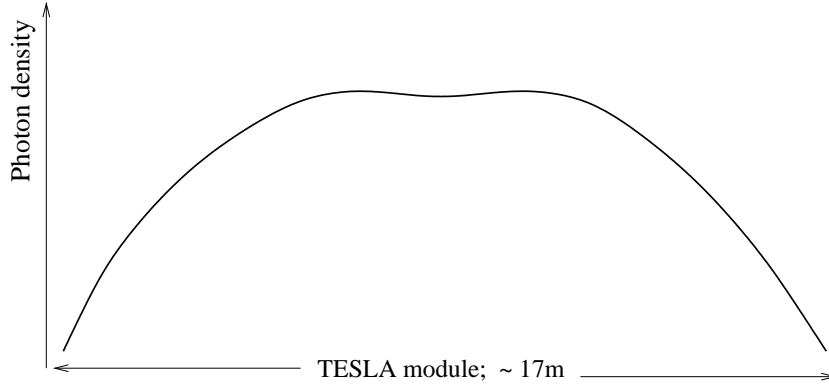


Figure 1.2: Photon density distribution through a TESLA accelerating module

In figure 1.2 we see that photon density tends to have the maximum in the center of the module. It is the region where the BPM is positioned. In further discussions it is assumed that the photon density near the BPM is a constant value independent from the BPM conductivity.

Energy losses in the TESLA accelerating module were computed in DESY-Hamburg [4] and are listed in table 1.3. As a BPM in the middle of the module was taken the pill-box BPM fabricated by Lorentz (from steel, [16]).

| | |
|---|-----------------------|
| Beam losses above 5 GHz: | 17.4 Watt |
| Power to absorber: | 14.9 Watt |
| Dissipation on non-superconducting parts: | 17.4 -14.9 = 2.5 Watt |

Table 1.3: Energy losses in the TESLA accelerating module

The power dissipation in the cryomodule at points $\sigma_{steel}(2K) = 1.88 \cdot 10^6 [\Omega^{-1}m^{-1}]$ and $\sigma \rightarrow \infty$ are computed in DESY [4], see figure 1.3 and the table 1.4.

So, there is a 1.4 Watt amount of power dissipation in the cryomodule which will take place even if the BPM were from the superconducting material. This happens because of other non-superconducting parts in the

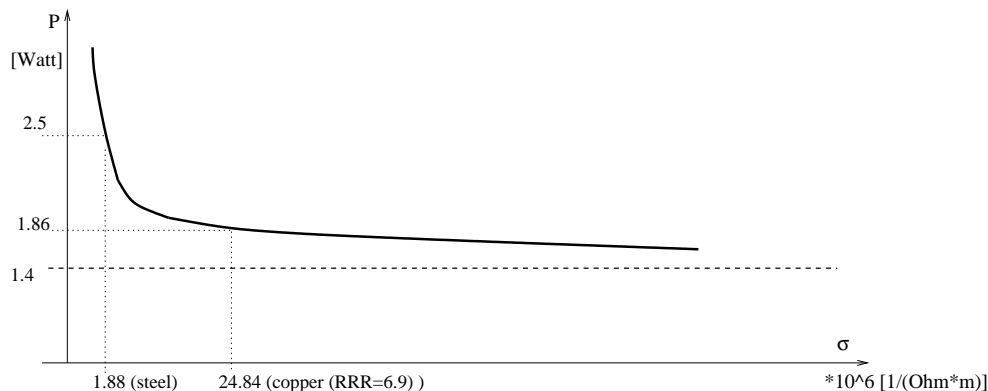


Figure 1.3: Energy loss within the cryomodule as a function of the BPM conductivity

| BPM cond. [$\Omega^{-1}\text{m}^{-1}$] | Diss. in module | on BPM |
|--|--------------------|---------------------|
| $\sigma_{steel}(2K) = 1.88 \cdot 10^6$ | 2.5 Watt | ≈ 1.1 Watt |
| $\sigma \rightarrow \infty$ | ≈ 1.4 Watt | — |
| $\sigma = 24.84 \cdot 10^6$ | 1.86 Watt | ≈ 0.46 Watt |

Table 1.4: Energy dissipation values in the TESLA accelerating module depending on the BPM conductivity

module².

The power dissipation on a metal in cryogenic environment is no longer in inverse proportionality to the square root of the metal conductivity. Because of anomalous skin effect the following proportionality takes place: $P_{2K}(\sigma) \sim \sigma^{-\frac{1}{3}}$ [17]. We can approximate the curve in figure 1.3 as

$$P_{2K}(\sigma) = a\sigma^{-\frac{1}{3}} + b, \quad (1.1)$$

where a and b are some constants. When we put first two values from table 1.4 in equation 1.1 we find $a \approx 135.76$ and $b = 1.4$ W.

- Increasing the conductivity of the BPM is the most promising way to decrease energy dissipation on the BPM walls. So that the task is to build a monitor with significant higher conductivity than steel. For example if we copperplate the inside of the BPM (designed by Lorentz) by copper type

²Note, that we do not discuss here power dissipation (≈ 27.9 mW) caused by the resonating modes of the cavity, as it is negligible compared to the values listed in table 1.4. More detail about power dissipation caused by the resonating modes of the cavity see subsection 4.1.6.

RRR=6.9 (Room Resistivity Ratio; the conductivity in 2 K is 6.9 times higher than in 293 K), which conductivity at 2 K is $\sigma = 24.84 \cdot 10^6 [\Omega^{-1}\text{m}^{-1}]$ there will be 2.39 times less energy dissipation on the BPM walls, see table 1.4. The value 1.86 Watt in the table was computed by equation 1.1.

A new monitor should also provide at least 10 μm beam position resolution for single bunch measurements in a multi-bunch regime of ~ 330 (180)ns bunch spacing.

Chapter 2

Survey of the BPMs

Here we give a general survey of the BPM technique. Operational principles of the different type of BPMs are discussed. For more detailed analysis follow the references in this chapter.

A BPM is a device to detect beam position in accelerators. BPMs are part of the family of Beam Diagnostic Devices. They are our sensing organs to see what is going on with the beam in an accelerator.

Important characteristics of a BPM are position-resolution and time-resolution. Position-resolution of the BPM is the smallest deflection of the beam which a BPM can sense. Time-resolution is the BPM's speed of signal detection. For example, if we want to make bunch to bunch position measurements, time-resolution should be faster than the distance between bunches.

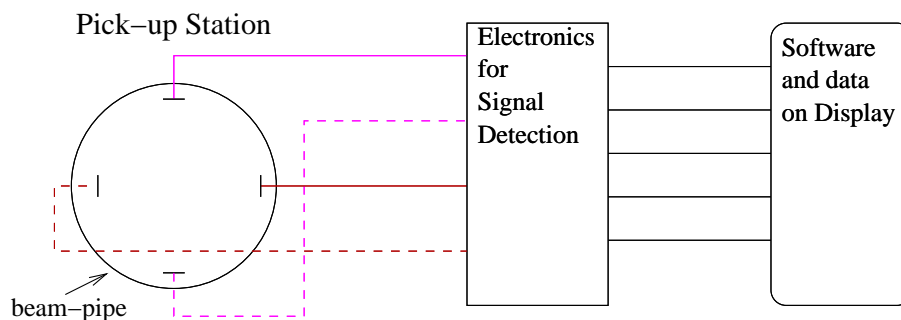


Figure 2.1: BPM architecture

The monitoring process passes the following three stages, (see figure 2.1):

Pick-Up station

Signal detection electronics

Data Processing

The **Pickup station** catches the signal of the displaced beam, then this signal is transferred to the set of **signal detecting electronics** to detect it. Signal detecting electronics extracts the beam position (displacement) information from the signals of the pickup station and down-converts it. This information is then delivered through ADC in a digital form for both horizontal and vertical planes. At the final stage, with the help of software, we see on display two numbers (or graphically), corresponding to beam x and y displacements.

Usually we take the signal from the *pickup station* through four ports. Two of them are for the horizontal plane, and the other two are for the vertical plane.

A single port delivers a signal voltage

$$V_{elec}(\omega, x, y) = s(x, y)Z(\omega)I_{beam}(\omega) \quad (2.1)$$

$V_{elec}(\omega, x, y)$ is proportional to the $I_{beam}(\omega)$ *beam intensity*, and *beam transverse displacement*, covered by the *sensitivity function* $s(x, y)$. Particularly in case of TESLA [3], because of the short bunches, shorter than 1 mm, the frequency spectrum of $I_{beam}(\omega)$ is of no concern; for all BPM designs TESLA-bunches are taken as Dirac impulse excitation signals. The *transfer impedance* $Z(\omega)$ depends on the pickup geometry.

There are many types of BPMs. In the next sections the most often used ones are discussed. There is no universal BPM. Which type to choose depends strongly on the particular task.

2.1 Pickup BPMs

For most cases, the beam energy is much greater than the energy that is coupled away in the pickup signal. That is, the pickup will not significantly decelerate the beam. With this in mind we can treat the beam as a current source. The pickup will intercept some portion of the electromagnetic fields that accompany the beam.

Any charged particle will exhibit an electromagnetic field. When the particle is at rest the field is electric and points radially outward in all directions as shown in figure 2.2a. As a particle moves it has both electric and magnetic fields. A qualitative view of a moving particle's field is shown in figure 2.2b.

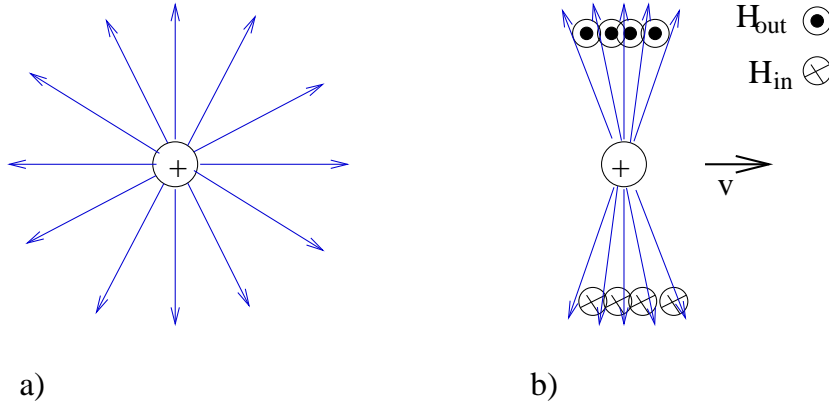


Figure 2.2: a: Electric field of a charged particle at rest. b: Electromagnetic fields of a relativistic charged particle ($\gamma \gg 1$)

As the particle velocity approaches the speed of light or as the kinetic energy of the beam becomes much greater than the particle's rest energy, the direction of the electric field becomes transverse to the direction of motion (TEM) [19].

The limiting case of a TEM pulse for a high energy particle beam electromagnetic field allows one to use Ampere's law for the distribution of image current flowing on the walls of the pipe. The magnitude of the image current is equal to the beam current but has opposite sign. Ampere's law with displacement current is:

$$\oint \vec{H} \cdot d\vec{l} = I_{beam} + \epsilon \frac{\partial}{\partial t} \int \int_{surf} \vec{E} \cdot \vec{z} \cdot dA \quad (2.2)$$

where \vec{z} is a unit vector that runs parallel to the beam and $d\vec{l}$ is a vector that is in a plane normal to the beam direction as shown in figure 2.3,a. Since

the electric field of the TEM wave is perpendicular to the beam direction, the displacement current term on the right side of equation 2.2 is zero. The transverse magnetic field can be found from the solution of the static two dimensional version of Ampere's law

$$\vec{\nabla} \times \vec{H} = \vec{J}_{beam} \quad (2.3)$$

The transverse electric field is equal to the magnetic field multiplied by the wave impedance of free space:

$$\vec{E} = -\sqrt{\frac{\mu_0}{\epsilon_0}} \vec{z} \times \vec{H} \quad (2.4)$$

Since there are no electromagnetic fields in the metal of the beam pipe, an image current density must flow on the surface of the beam pipe to cancel out the magnetic field tangential to the metal surface.

$$\vec{J}_{image} = \vec{n} \times \vec{H} \quad (2.5)$$

where J_{image} has the units of Amperes/meter and \vec{n} is a unit vector that is normal to the beam pipe surface [36].

For a cylindrical beam pipe with the beam current passing through the center of the pipe:

$$J_{image} = -\frac{I_{beam}}{2\pi b} \quad (2.6)$$

If a thin pencil beam passes off center as shown in figure 2.3b, [22]:

$$J_{image}(\phi) = -\frac{I_{beam}}{2\pi b} \left(\frac{b^2 - r^2}{b^2 + r^2 - 2br \cdot \cos(\phi - \theta)} \right) \quad (2.7)$$

If two electrodes are fashioned to intercept only a fraction of the image current as shown in figure 2.3b, the electrode closer to the beam will intercept more image current compared to the further electrode. The difference in intercepted image current between the two electrodes will be proportional to the beam position for small beam displacements. However, for large beam displacements, the difference signal will deviate from being linear with beam position as shown in figure 2.4, [20].

We will define the sensitivity of the electrode as equal to the ratio of captured image current to the total image current.

$$s = \frac{\int J_{image} dw}{I_{beam}}, \quad (2.8)$$

where w is the width of the electrode.

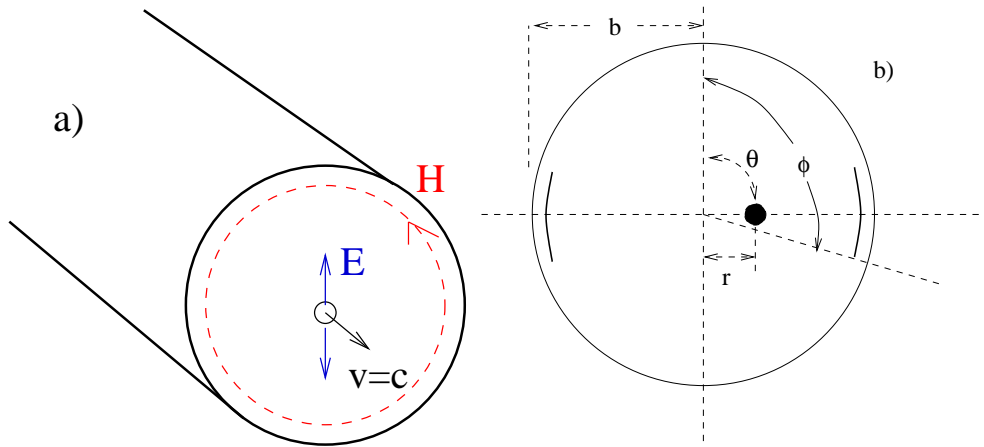


Figure 2.3: a: Beam pipe configuration for application of Faraday's Law. b: Beam going off center through the beam pipe. The dark lines on both sides are the pickup electrodes.

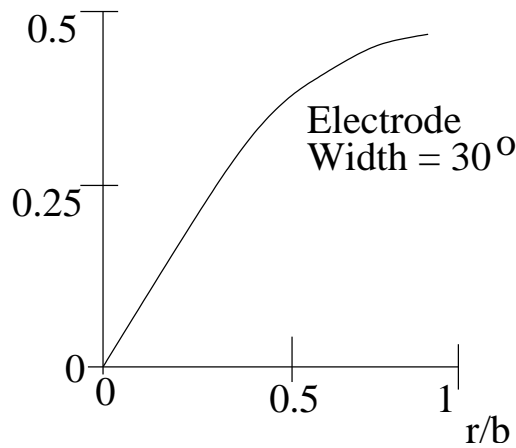


Figure 2.4: Difference in intercepted image current between the two electrodes shown in figure 2.3,b versus actual beam displacement

2.1.1 Stripline BPM

A displaced beam produces non-equal current distribution on stripline electrodes. Comparing this non-equal signal distribution we detect the bunch position.

The electrode of a stripline monitor consists of a transmission-line of length L and width w which is mounted into the beam pipe (Figure 2.5¹)

¹For another strip-line design see [32]

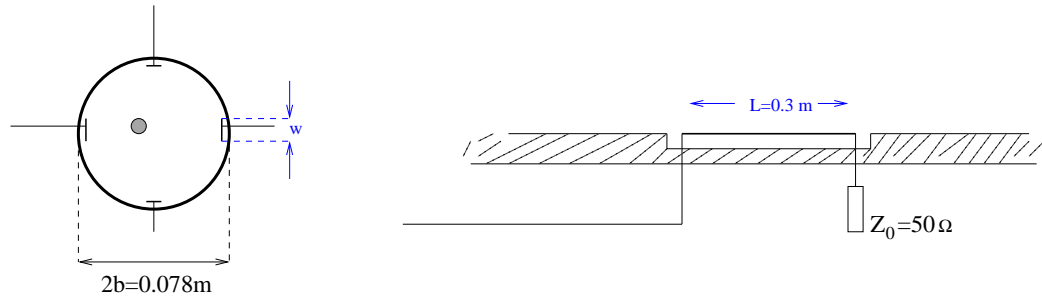


Figure 2.5: Cross-section of a stripline pick-up station and horizontal view of one electrode

and is terminated at both ports in its characteristic impedance Z_0 .

Because the width of the stripline is only a fraction of the beam-pipe circumference, the stripline will not intercept all of the image current. This fraction of image current will travel across the upstream gap as a displacement current. This displacement current will give rise to a voltage pulse on the upstream end of the stripline, see figure 2.6, $t=0$. The magnitude of the pulse is equal to the captured fraction of image current times the characteristic impedance of the stripline. Because the stripline is terminated at the upstream and downstream ends with the same characteristic impedance, the voltage pulse will split into two equal pulses with one of the pulses traveling to the upstream termination and the other pulse traveling to the downstream termination.

The fraction of image current traveling downstream will travel along the top of the stripline until it encounters the downstream gap, figure 2.6, $t=L/c$. At the downstream gap another pulse is created. This pulse is equal to the upstream pulse but has the opposite polarity. This change in polarity is due to the fact that the electric field lines at the downstream gap start on the edge of the stripline and terminate on the ground plane. Whereas at the upstream gap, the electric field lines started at the ground plane and terminated on the upstream edge of the stripline.

The pulse at the downstream gap also splits into two pulses. However, if the velocity of the beam and the phase velocity of the stripline are equal, the pulse that was created at the upstream gap and headed towards the downstream termination will arrive at the downstream gap at the same time the image current is inducing the downstream voltage pulse. Since the pulses heading towards the downstream termination have opposite polarity, these pulses will cancel each other and there will be no energy dissipated in the downstream termination.

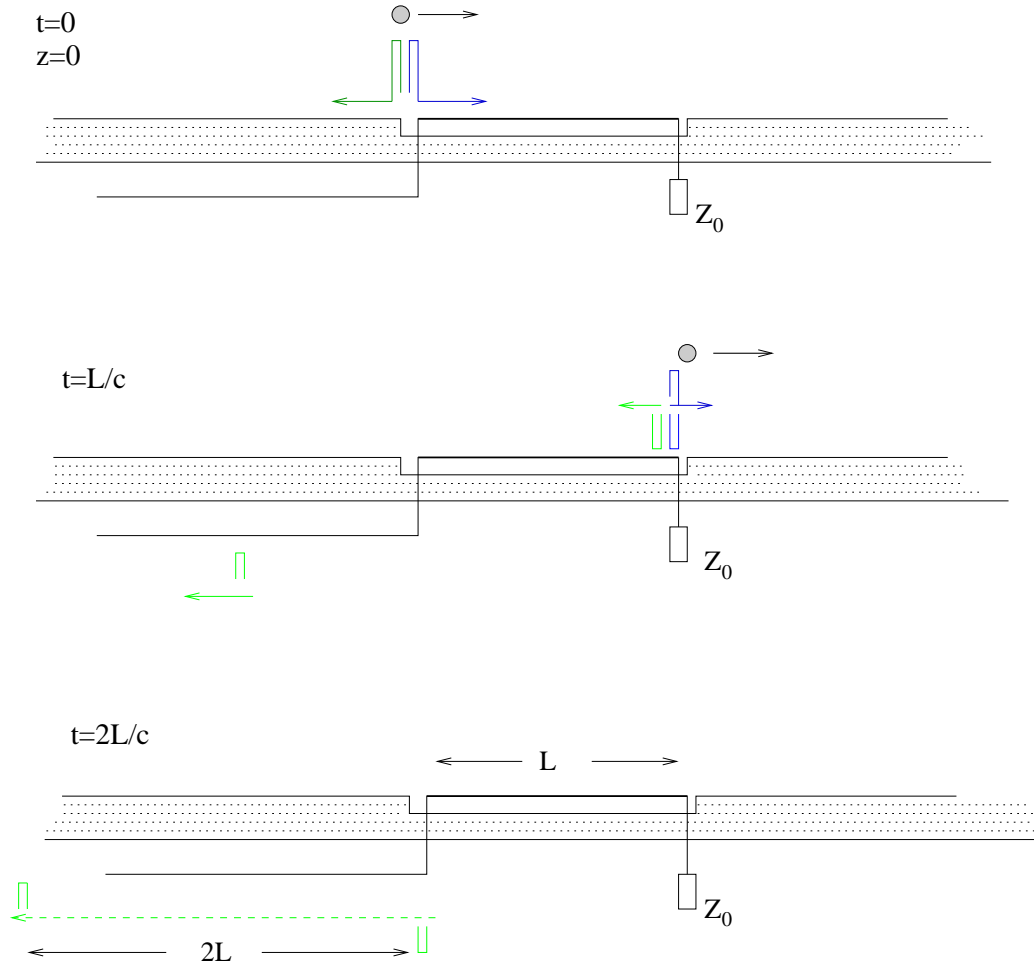


Figure 2.6: Operation principle of the stripline monitor

Voltage corresponding to the bunch offset: At first let us compute by an electrode in figure 2.5 coupled image current corresponding to the TESLA bunch 100 μm offset.

TESLA bunches are short enough to be considered as dirac impulses. The bunch current can be written as

$$I_b = q \cdot c \cdot \delta(z) = 3.2 \cdot 10^{-9} \cdot 3 \cdot 10^8 \cdot \delta(z) = 0.96 \cdot \delta(z) \text{ [C} \cdot \text{s}^{-1}] \quad (2.9)$$

where q is the charge of the bunch and c is velocity of the light. Let us take the width of the stripline electrode to have the maximal opening angle

$$\varphi = \frac{\pi}{2} \quad (2.10)$$

When the bunch has no offset then the coupled image current is

$$I_c = -\frac{I_b}{4} \quad (2.11)$$

Now, if the bunch has r offset the same electrode couples the following image current (see figure 2.3 and equation 2.7):

$$I_c(r) = -\frac{I_b}{2\pi}(b^2 - r^2) \int_{-\frac{\pi}{4}}^{\frac{\pi}{4}} \frac{d\varphi}{b^2 + r^2 - 2br \cdot \cos \varphi} \quad (2.12)$$

In our case $b = 0.039$ m and we look for $r \ll b$, equation 2.12 can be written as

$$I_c(r) \approx -\frac{I_b}{2\pi} \int_{-\frac{\pi}{4}}^{\frac{\pi}{4}} \frac{d\varphi}{1 + \left(\frac{r}{b}\right)^2 - 2\frac{r}{b} \cdot \cos \varphi}, \quad (r \ll b). \quad (2.13)$$

To compute the integral in equation 2.13 we developpe $(1 + \left(\frac{r}{b}\right)^2 - 2\frac{r}{b} \cos \varphi)^{-1}$ in series of $\frac{r}{b}$ at the point $\frac{r}{b} = 0$:

$$\frac{1}{1 + \left(\frac{r}{b}\right)^2 - 2\frac{r}{b} \cdot \cos \varphi} \approx 1 + \left(\frac{1}{1 + \left(\frac{r}{b}\right)^2 - 2\frac{r}{b} \cdot \cos \varphi} \right)'_{\frac{r}{b}=0} \cdot \frac{r}{b} \quad (2.14)$$

There is no need to discuss the terms with higher order because of the condition in equation 2.13, and equation 2.14 becomes

$$\frac{1}{1 + \left(\frac{r}{b}\right)^2 - 2\frac{r}{b} \cdot \cos \varphi} = 1 + 2\frac{r}{b} \cdot \cos \varphi \quad (2.15)$$

Using equation 2.15 the equation 2.13 becomes

$$I_c(r) = -\frac{I_b}{4} - \frac{2I_b}{\sqrt{2}\pi b} r \quad (2.16)$$

The current ΔI corresponding to the bunch offset is the difference between equations 2.16 and 2.11:

$$\Delta I(r) = \frac{2I_b}{\sqrt{2}\pi b} r \quad (2.17)$$

The impulse response is sensed at the upstream termination. It consists of the first pulse created at the upstream gap followed by a pulse in the opposite polarity with a distance twice the length of the stripline, see figure 2.6,

$t=2L/c$, [20]. Hence, using the equations 2.17, 2.9 the signal corresponding to the bunch 100 μm offset can be written as

$$\Delta V(z, r = 0.0001\text{m}) = \frac{Z_0 \Delta I}{2} [\delta(z) - \delta(z - 2L)] \quad (2.18)$$

With the Fourier transformation:

$$\Delta V(z) = \int_{-\infty}^{\infty} \Delta V(k) e^{ikz} dk \quad (2.19)$$

and

$$\Delta V(k) = \frac{1}{2\pi} \int_{-\infty}^{\infty} \Delta V(z) e^{-ikz} dz \quad (2.20)$$

where

$$k = \frac{1}{\lambda} = \frac{\omega}{c} \quad (2.21)$$

equation 2.18 becomes

$$\Delta V(k, r = 0.0001\text{m}) = \frac{Z_0 \cdot \Delta I}{2\pi} \cdot e^{i\pi/2} \cdot e^{-ikL} \sin(kL) \quad [\text{V} \cdot \text{m}] \quad (2.22)$$

The magnitude of the response has a maximum at frequencies where the length is an odd multiple of quarter wavelengths:

$$kL = \frac{\pi}{2}(2n - 1) \quad \text{or} \quad f_0 = \frac{1}{4} \frac{c}{L}(2n - 1) \quad (2.23)$$

where $n=1,2,3,\dots$. The stripline pickup is usually designed to operate in the first lobe ($n=1$). The 3 dB points of this lobe are at:

$$f_{low} = \frac{1}{2} f_0, \quad f_{up} = 3 \cdot f_{low} \quad (2.24)$$

For the electrode in figure 2.5 with $L=0.3$ m the central frequency is

$$f_0 = \frac{c}{4L} = 250 \text{ MHz.} \quad (2.25)$$

Using equations 2.9, 2.17, equation 2.22 and multiplying by

$$k = \frac{\omega}{c} = \frac{\pi}{2L} = 5.2 \quad [\text{m}^{-1}] \quad (2.26)$$

for $r = 0.0001$ m and $b = 0.039$ m we get the magnitude of the voltage

$$\Delta V(r = 0.0001\text{m}) \approx 45.7 \text{ mV}. \quad (2.27)$$

The BW of this frequency according equation 2.24 is

$$BW = 250 \text{ MHz}. \quad (2.28)$$

The thermal noise level is

$$V_N = NF \sqrt{4k_b T \cdot BW \cdot Z_0} \approx 0.113 \text{ mV}. \quad (2.29)$$

where NF is noise factor of the electronics², $k_b = 1.38 \cdot 10^{-23}$ [JK⁻¹] is Boltzmann coefficient. From equations 2.29 and 2.27 we compute the absolute resolution equal to 247 nm.

$$\Delta V(r = 247\text{nm}) = \frac{I_b Z_0}{\sqrt{2\pi^2 b}} r \approx V_N. \quad (2.30)$$

Time-resolution is defined by the bandwidth of the signal

$$\tau = \frac{1}{\pi \cdot BW} \text{ [s]} \quad (2.31)$$

And according equation 2.28 it is

$$\tau = \frac{10^{-6}}{\pi \cdot 250} \approx 1.27 \text{ [ns]} \quad (2.32)$$

The advantages of stripline BPM's are:

- High output levels in the medium RF range (250 ... 500 MHz),
- Simplified read-out electronics: 50 Ω source impedance simplifies input filter.
- High time resolution.
- Stripline BPMs are promising for beam position measurement near the interaction point (IP) of the accelerator. Because they show the direction of the bunch. It means we will not mix bunches flying in opposite directions.

²For comparison we took $NF = 7.5$ as it is for the prototype electronics in chapter 4.

2.2 Cylindrical Pill-box cavity BPM

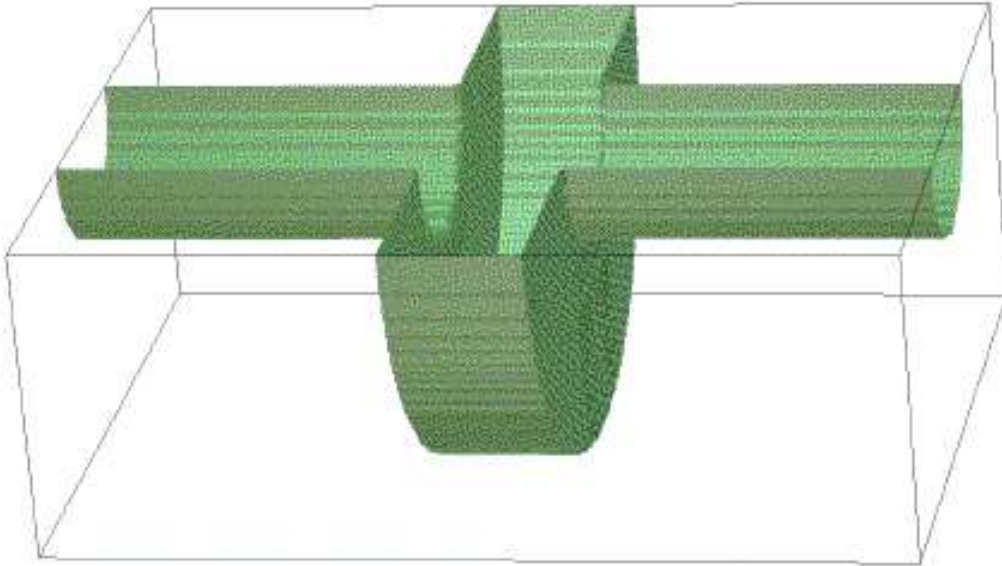


Figure 2.7: Cylindrical pick-up station

The pick-up station of this BPM is a cylindrical cavity, mounted into the beam-pipe. In figure 2.7 the cut of such a structure is shown.

Passing through the cylindrical cavity, a beam excites electro-magnetic field oscillations in the cavity. If the beam was off-centered it excites also dipole modes. The bigger the offset of the beam is the stronger dipole modes are excited.

From all oscillating modes the first dipole TM_{110} -mode is used for beam position monitoring: Figure 2.8. Its signal in the pipe region (for bunch velocity $v \approx c$) has linear dependence from the bunch displacement, figure 2.9 (see also subsection 2.2.3, [27]).

The mode is coupled from the cavity by four symmetrically arranged feedthroughs: two for x position detection and the other two for y position detection.

One of the most important parameters of such BPM is τ : the *damping time*. This is the time after which the excited resonating field is damped by a factor of e . τ should be less than the distance between bunches if we want to make bunch to bunch measurement. The definition of τ is

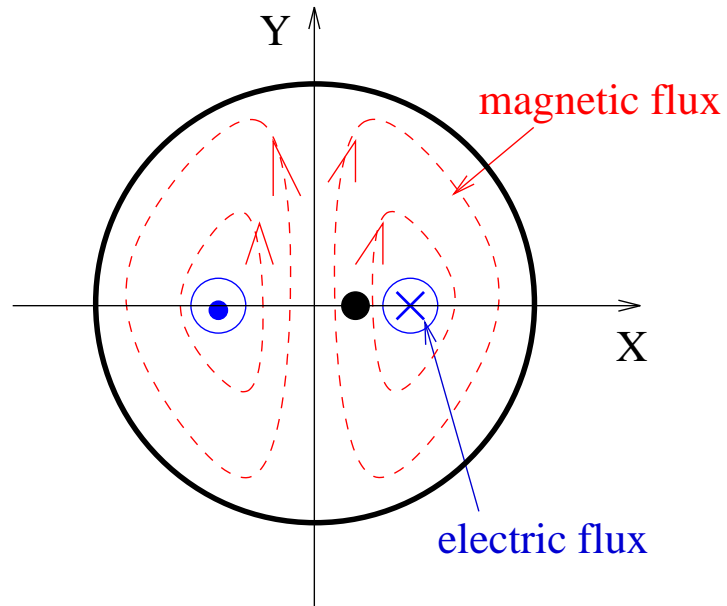


Figure 2.8: TM_{110} -mode pattern in cavity cross-section; the black spot shows the position of the bunch

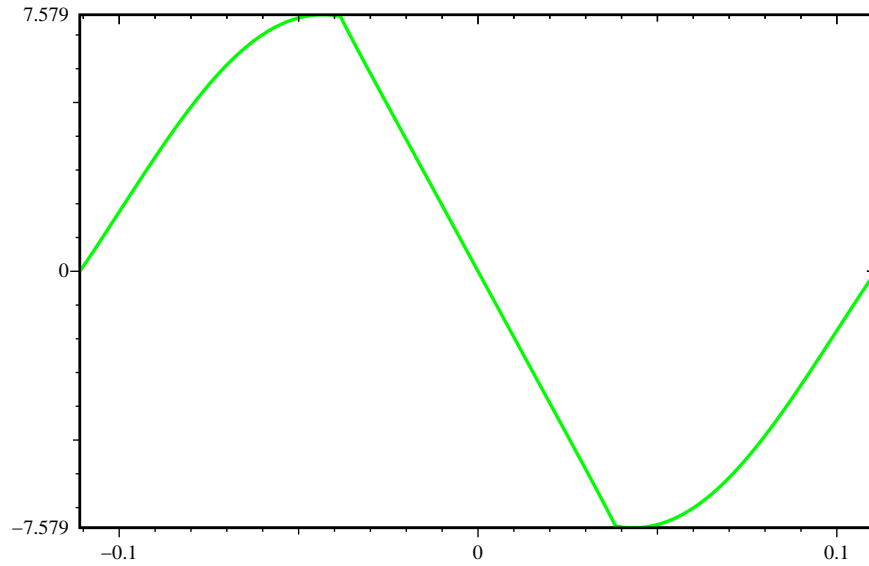


Figure 2.9: Voltage along z axis of the TM_{110} -mode depending on the displacement x [m]

$$\tau = \frac{Q_L}{\pi f} = \frac{1}{\pi \cdot BW}. \quad (2.33)$$

where $f = Q_L \cdot BW$ (BW =Band-Width of the mode). Here Q_L is the loaded quality factor of the cavity for a given frequency f .

$$\frac{1}{Q_L} = \frac{1}{Q_0} + \frac{1}{Q_{ext}}, \quad (2.34)$$

where Q_0 and Q_{ext} are *unloaded* and *external quality factors* of the cavity correspondingly. The unloaded quality factor of some resonating mode depends on the cavity geometry and material:

$$Q_0 = \frac{2\pi f \cdot W}{P_{in}}, \quad (2.35)$$

P_{in} is the energy dissipation in the cavity walls for the mode with frequency f . W is the stored energy in that mode. The external quality factor is connected with the *coupling factor* β by

$$\beta = \frac{P_{out}}{P_{in}} = \frac{Q_0}{Q_{ext}}. \quad (2.36)$$

If we mount a pin-antenna near the the maximum of the electric field ($r_{E_{max}} = 0.481 \cdot r$ for the dipole mode TM_{110} , r is radius of the cylindrical cavity), the following effective voltage will be coupled into $Z = 50\Omega$ coaxial cable [18]:

$$V_{out}^{110}(\delta x) = \pi f_{110} \sqrt{Z \left(\frac{1}{Q_L} - \frac{1}{Q_0} \right) \left(\frac{R_{sh}}{Q} \right)_{110}} \cdot q \quad (2.37)$$

where $\left(\frac{R_{sh}}{Q} \right)_{110}$ is the *shunt impedance* over Q of the TM_{110} -mode depending on the bunch offset δx . In the pipe region the dipole mode voltage has linear dependence (see figure 2.9 and equation 2.122) on the bunch offset δx , hence we can rewrite (2.37) in pipe region as

$$V_{out}^{110}(\delta x) = \pi f_{110} \sqrt{Z \left(\frac{1}{Q_L} - \frac{1}{Q_0} \right) \left(\frac{R_{sh}}{Q} \right)_{110}^{fix} \frac{\delta x}{\delta x_{fix}}} q \quad (2.38)$$

Now $\left(\frac{R_{sh}}{Q} \right)_{110}^{fix}$ is the value of $\left(\frac{R_{sh}}{Q} \right)_{110}$ at some fixed offset δx_{fix} . The shunt impedance over Q defines the strength by which the mode will act on the

charge when it passes through the cavity parallel to the z -axis by some given offset δx :

$$\frac{R_{sh}(\delta x)}{Q} = \frac{V(\delta x) \cdot V^*(\delta x)}{4\pi f \cdot W} \quad (2.39)$$

where $V(\delta x) = \int_{-\infty}^{\infty} E_z(\delta x) e^{i\omega \frac{z}{v}} dz$ is the complex voltage for a given mode, which a charge-particle sees when it flies with speed v along the z -axis with some offset δx , and $V^*(\delta x)$ is the conjugate complex voltage. Shunt impedance over Q of a given mode can be theoretically computed for a cavity without a beam-pipe. In subsection 2.2.1 we compute theoretically the shunt impedances of the first monopole mode TM_{010} , the dipole mode TM_{110} and the second monopole mode TM_{020} of the prototype without the beam-pipe (The prototype is described in chapter 4).

The frequency and strength of the modes depend on the pick-up station geometry. The index of the TM_{110} -dipole mode tells us, that this mode has no oscillation with respect to the z coordinate. The frequencies of TM modes are very sensitive to the radius of the cavity. The smaller the radius the higher is the frequency of the dipole mode, see equation 2.41.

The signal can be coupled out by a pin-antenna (electrical coupling, see figure 2.10,a), by a loop (magnetic coupling, see figure 2.10,b) or by a waveguide (electro-magnetic coupling, see figure 2.10,c).

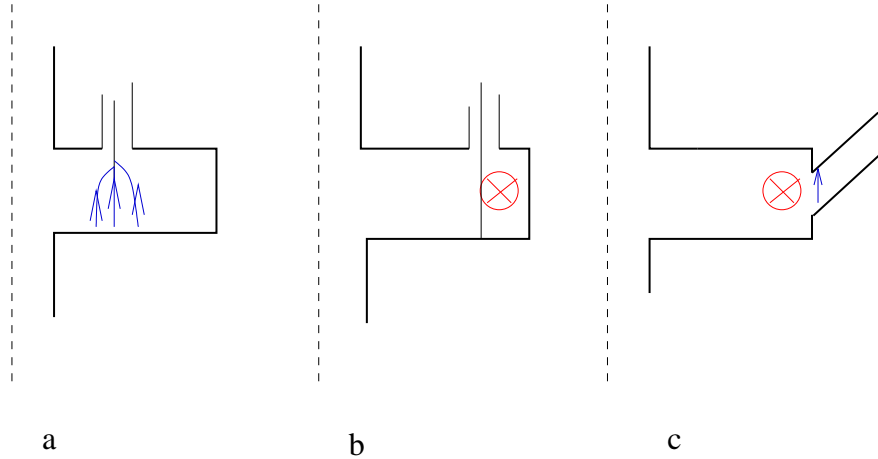


Figure 2.10: a: electric coupling, b: magnetic coupling, c: electro-magnetic coupling

The higher the coupling factor, the more power we take from the cavity. It leads to the lower *loaded quality factor*. Theoretical computations of magnetic

and electric coupling of the prototype without the beam-pipe are listed in subsection 2.2.2.

The electronics of cavity BPMs are typically narrow-band. It takes maximally the signal of the dipole mode and stops impulses on the other resonating frequencies (monopole modes of first and second order, see figure 2.11). Monopole modes are excited much stronger than dipole modes, because their maxima lie on the z axis, close to the bunch trajectory.

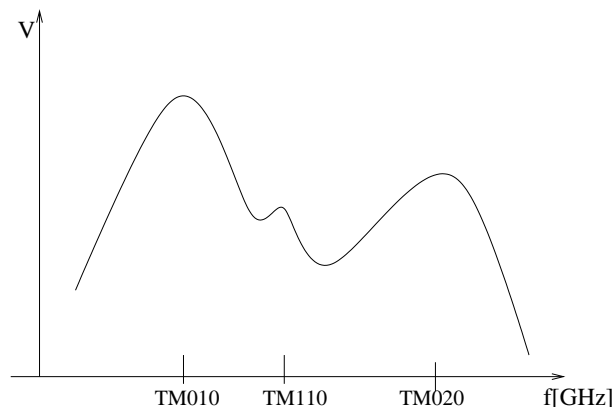


Figure 2.11: Voltages of the first and second monopole modes compared with the TM_{110} dipole mode

- **Pill-box cavity has a high resolution potential.** For example the absolute resolution performance of the prototype, computed in chapter 4, is 78.6 nm.

The absolute resolution performance of such a BPMs can reach even 10 nm values [33]. For comparison see the absolute resolution performance of the stripline BPM, equation 2.30.

- On the other hand **we loose time-resolution.** For example the time resolution of the prototype in chapter 4 is 197.6 ns. Time resolution value is defined according equation 2.33, which can be reduced by reducing Q_L .

For comparison see the time-resolution value of the stripline BPM, equation 2.32.

- Another important advantage of this type BPM is its **radial symmetry.** Radial symmetry makes manufacturing easier and more precise.

2.2.1 Shunt impedances of the pill-box cavity without a beam-pipe

- Shunt impedance over Q of the dipole mode TM_{110} , see figure 2.12.

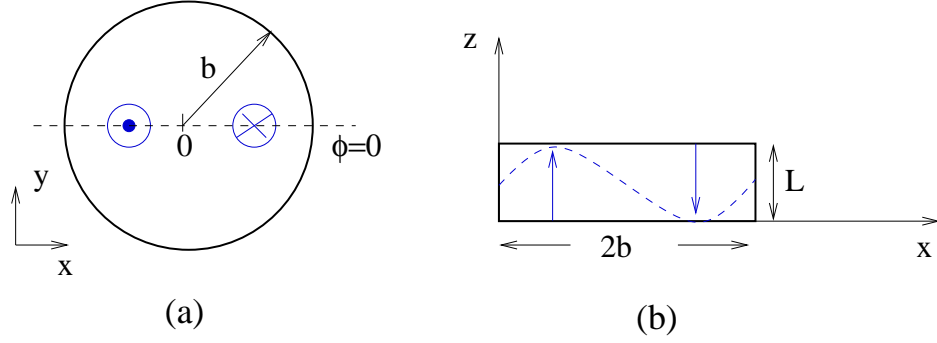


Figure 2.12: a: Cross-section of the cavity without a beam-pipe; b: Electrical field of the dipole mode

The electrical field of the dipole mode can be given as

$$E_z = E_0 \cos \phi \cdot J_1(rk_{110}) \cdot e^{i\omega t}, \quad (2.40)$$

From the boundary condition $E_z(r = b) = 0$ we get

$$J_1(bk_{110}) = 0, \text{ and } k_{110} = 3.83/b = \frac{\omega_{110}}{c}. \quad (2.41)$$

Now when a charged-particle flies with velocity $v \approx c$ through the cavity with some x offset ($\phi = 0$), it sees the following voltage:

$$V(x) = E_0 J_1(xk_{110}) \int_0^L e^{i\omega \frac{z}{c}} dz \quad (2.42)$$

After the integration we get

$$V(x) = E_0 J_1(xk_{110}) LT e^{i\frac{\omega L}{2c}} \quad (2.43)$$

where T is called transit time factor equal to

$$T = \frac{\sin \frac{\omega L}{2c}}{\frac{\omega L}{2c}} \quad (2.44)$$

The stored energy W in that mode is

$$W = \frac{1}{2} \int \epsilon_0 |E_z|^2 \cdot r d\phi \cdot dr \cdot dz \quad (2.45)$$

Using equation 2.40 we get

$$W = \frac{E_0^2 \epsilon_0 L}{2} \int_0^{2\pi} \int_0^b \cos^2 \phi J_1^2(rk_{110}) \cdot r d\phi \cdot dr, \quad (2.46)$$

where

$$\int_0^{2\pi} \cos^2 \phi d\phi = \pi \quad (2.47)$$

and we get

$$W = \frac{E_0^2 \epsilon_0 L \pi}{2} \int_0^b J_1^2(rk_{110}) \cdot r dr, \quad (2.48)$$

here $\epsilon_0 = 8.854 \cdot 10^{-12}$ [F/m] is the permeability of the vacuum. Putting equations 2.48 and 2.43 in equation 2.39 we find

$$\frac{R_{sh}(x)}{Q} \approx \frac{J_1^2(xk_{110})LT^2}{\omega \epsilon_0 \pi M} \quad (2.49)$$

where according to [28]

$$M = \int_0^b J_1^2(rk_{110}) \cdot r dr = \frac{b^2}{2} J_0^2(bk_{110}) \quad (2.50)$$

For example if we take $L = 0.018$ m and $b = 0.111$ m from the cavity discussed in chapter 4 we will get $\omega \approx 10.35 \cdot 10^9$ [Hz], $M \approx 0.001$ [m²], $T \approx 1$ and

$$\frac{R_{sh}(x = 0.001m)}{Q} \approx 0.02[\Omega] \quad (2.51)$$

• **Let us compute shunt impedance over Q of the monopole modes** according equation 2.39. The electric fields of first and second monopole modes are in figures 2.13 and 2.14 respectively.

The electric fields of first and second monopole modes can be given as

$$E_z = E_0 \cdot J_0(rk) e^{i\omega t}, \quad (2.52)$$

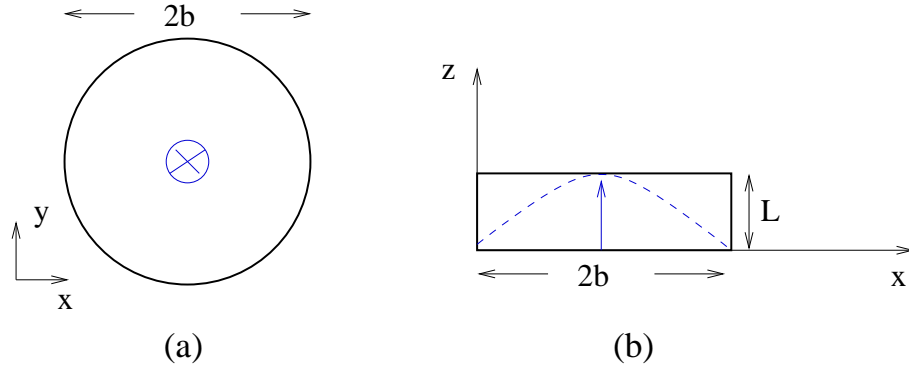


Figure 2.13: a: Cross-section of the cavity without a beam-pipe; b: Electric field of the first monopole mode

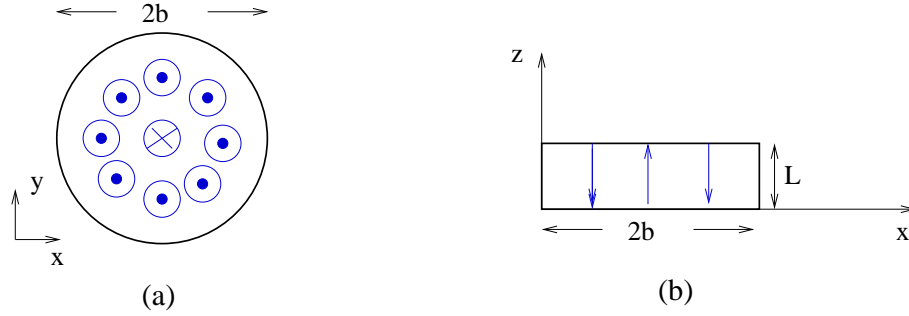


Figure 2.14: a: Cross-section of the cavity without a beam-pipe; b: Maximums of the electric field of the second monopole mode

where k is either k_{010} corresponding to the first monopole mode TM_{010} or k_{020} corresponding to the second monopole mode TM_{020} . With the boundary conditions $E_z(r = b) = 0$

$$J_0(bk) = 0, \quad k = \frac{\omega}{c}. \quad (2.53)$$

The first and second root points ($bk_{010} = 2.405$ and $bk_{020} = 5.52$) of equation 2.53 define the resonating frequencies of first and second monopole modes respectively. In an analogous way of equation 2.43 we find

$$|V(x)|^2 \approx E_0^2 J_0^2(xk) L^2 T^2 \quad (2.54)$$

To compute stored energy we use equations 2.45, 2.52, and we get

$$W = E_0^2 \epsilon_0 L \pi \int_0^b J_0^2(rk) \cdot r dr. \quad (2.55)$$

Here

$$\int_0^b J_0^2(rk) \cdot r dr = \frac{b^2}{2} (J_0^2(bk) + J_1^2(bk)), \quad (2.56)$$

where $J_0^2(bk) = 0$ from boundary conditions and the stored energy is

$$W = E_0^2 \epsilon_0 L \pi \frac{b^2}{2} J_1^2(bk) \quad (2.57)$$

Putting equations 2.57 and 2.54 in equation 2.39 we get

$$\frac{R_{sh}(x)}{Q} \approx \frac{J_0^2(xk)L}{\omega \epsilon_0 \pi b^2 J_1^2(bk)} \quad (2.58)$$

Taking $L = 0.018$ m, $b = 0.111$ m, $k_{010} = 21.6667$, $k_{020} = 49.9$ we get

$$\frac{R_{sh}^{010}(x)}{Q} \approx 33[\Omega] \quad (2.59)$$

and

$$\frac{R_{sh}^{020}(x)}{Q} \approx 33.7[\Omega]. \quad (2.60)$$

2.2.2 Magnetic and electric coupling of the pill-box cavity without a beam-pipe

Magnetic coupling: Let us discuss loop-coupling of the first monopole mode. The magnetic field of the mode is shown in figure 2.15 and can be given as

$$H_\varphi = H_0 J_0'(rk) e^{i\omega t} \quad (2.61)$$

The ratio between the magnetic flux coupled by the loop Φ_{mc} (shown in figure 2.16) and the whole magnetic flux Φ_m is

$$n = \frac{\Phi_{mc}}{\Phi_m} \quad (2.62)$$

where

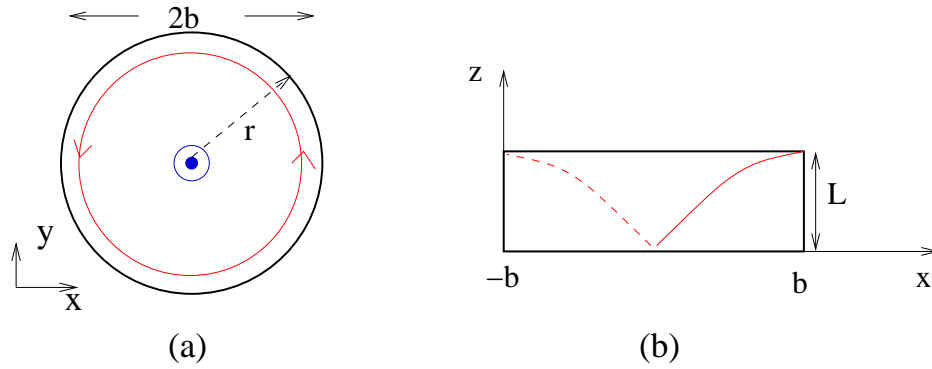


Figure 2.15: a: TM_{010} mode pattern in the cavity without a beam-pipe. Blue point shows the maximum of electric field, red circle shows maximum of magnetic field; b: Magnetic field of the first monopole mode TM_{010}

$$\Phi_{mc} = \mu_0 H_0 L e^{i\omega t} \int_{b-l}^b J'_0(rk) \cdot dr = -\mu_0 H_0 L e^{i\omega t} \int_{b-l}^b J_1(rk) \cdot dr \quad [V \cdot s] \quad (2.63)$$

and

$$\Phi_m = \mu_0 H_0 L e^{i\omega t} \int_0^b J'_0(rk) \cdot dr \quad [V \cdot s] \quad (2.64)$$

where $\mu_0 = 4\pi \cdot 10^{-12} [\frac{Vs}{Am}]$ is the magnetic permeability of the vacuum.

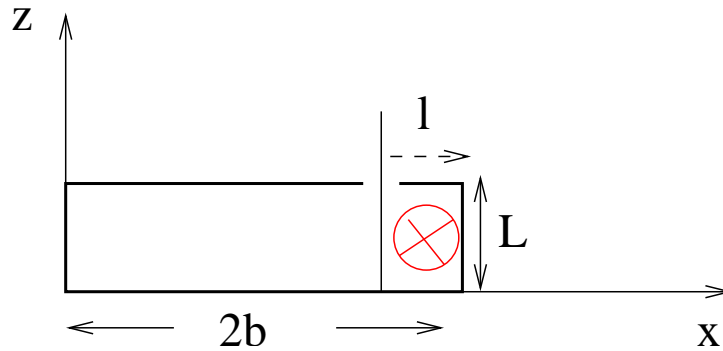


Figure 2.16: The cavity coupled by loop

The coupled voltage is

$$V_c = -\frac{d\Phi_{mc}}{dt} = i\omega\mu_0 H_0 L e^{i\omega t} \int_{b-l}^b J_1(rk) \cdot dr \quad (2.65)$$

where

$$\int_{b-l}^b J_1(rk) \cdot dr = -\frac{1}{k} [J_0(kb) - J_0(k(b-l))] \quad (2.66)$$

The first term in equation 2.66 is zero because of the boundary conditions, and the coupled power into the 50 Ω line is

$$P_c = \frac{V_c^2}{2 \cdot 50\Omega} = -\frac{\omega^2 \mu_0^2 H_0^2 L^2}{k^2 100\Omega} J_0^2(k(b-l)) \quad (2.67)$$

The power dissipated in the cavity is

$$P_{in} = \int \frac{H_\varphi^2}{2\sigma\delta} dF \quad (2.68)$$

where σ is the conductivity of the material, δ is skin depth

$$\delta = \frac{1}{\sqrt{\pi f \mu_0 \sigma}}, \quad (2.69)$$

and dF is the element surface

$$dF = b \cdot d\varphi \cdot dz + 2rd\varphi \cdot dr \quad (2.70)$$

Putting equation 2.70 together with equation 2.61 in equation 2.68 we get

$$P_{in} = P_{in}^{(1)} + P_{in}^{(2)} \quad (2.71)$$

where

$$P_{in}^{(1)} = \frac{\pi b L}{\sigma \delta} H_0^2 J_1^2(bk) \quad (2.72)$$

and

$$P_{in}^{(2)} = \frac{2\pi H_0^2}{\sigma \delta} \int_0^b [J_0'(rk)]^2 r \cdot dr \quad (2.73)$$

where

$$\int_0^b [J_0'(rk)]^2 r \cdot dr = \int_0^b J_1^2(rk) r \cdot dr = \frac{b^2}{2} J_1^2(bk) \quad (2.74)$$

Using equations 2.74, 2.73, 2.72 and 2.71 we get

$$P_{in} = \frac{\pi b H_0^2 J_1^2(bk)}{\sigma \delta} (L + b) \quad (2.75)$$

At the end the β coupling factor is

$$\beta = \frac{P_c}{P_{in}} = \frac{\omega^2 \mu_0^2 L^2 \sigma \delta}{k^2 100 \pi b J_1^2(bk) \cdot (L + b)} J_0^2(k(b - l)) \quad (2.76)$$

For example let us compute β for a cavity with following parameters: $L = 0.018$ m, $l = 0.02$ m, $b = 0.111$ m, $\sigma = 1.33 \cdot 10^6 \Omega^{-1} \text{m}^{-1}$, $f = 1.03$ GHz, $\delta = 0.14 \cdot 10^{-4}$ m, $k = 21.6667$. Putting these parameters in equation 2.76 we get

$$\beta \approx 21 \quad (2.77)$$

This result is tested by GdfidL, see table 2.1.

| | Theor. | GdfidL |
|---------|--------|--------|
| β | 21 | 18 |

Table 2.1: Test of the theoretical computation of the coupling factor

Magnetic coupling of the dipole mode TM_{110} : Magnetic coupling of the dipole mode is going to be computed in the same way as the computation of the magnetic coupling of the monopole mode TM_{110} .

The components of the dipole mode magnetic field are

$$H_{\varphi 110} = -iC \frac{\omega_{110} \epsilon_0}{k_{110}} J_1'(rk_{110}) \cos \varphi \cdot e^{i\omega_{110}t} \quad (2.78)$$

$$H_{r 110} = -iC \frac{\omega_{110} \epsilon_0}{k_{110}^2 r} J_1(rk_{110}) \sin \varphi \cdot e^{i\omega_{110}t} \quad (2.79)$$

where C is a constant value with dimension [V/m].

According figure 2.16 the loop in place $\cos \varphi = 1$ couples following magnetic flux ($H_r = 0$)

$$\Phi_{mc110} = \mu_0 \int_{b-l}^b \int_0^L H_{\varphi110} \cdot dx dz = -\frac{iC\mu_0\omega_{110}\epsilon_0 L}{k_{110}} \cdot e^{i\omega_{110}t} \int_{b-l}^b J_1'(xk_{110}) \cdot dx \quad (2.80)$$

The coupled voltage is

$$V_{c110} = \frac{d\Phi_{mc110}}{dt} = \frac{C\mu_0\omega_{110}^2\epsilon_0 L}{k_{110}} \int_{b-l}^b J_1'(xk_{110}) \cdot dx \quad (2.81)$$

and coupled power is

$$P_{c110} = \frac{V_{c110}^2}{100\Omega} = \frac{C^2\mu_0^2\omega_{110}^4\epsilon_0^2 L^2}{k_{110}^2 100\Omega} \left(\int_{b-l}^b J_1'(xk_{110}) \cdot dx \right)^2 \quad (2.82)$$

The power dissipated in the cavity is

$$P_{in110} = \int \frac{H_{\varphi110}^2 + H_{r110}^2}{2\sigma\delta_{110}} \cdot dF \quad (2.83)$$

Here dF is element surface, see equation 2.70, and we get

$$P_{in110} = P_{in}^{(1)} + P_{in}^{(2)} \quad (2.84)$$

where

$$P_{in}^{(1)} = \frac{b}{2\sigma\delta_{110}} \int (H_{\varphi110}^2(r=b) + H_{r110}^2(r=b)) d\varphi dz \quad (2.85)$$

The second term in integral is zero, see equation 2.41, and we get

$$P_{in}^{(1)} = \frac{bLC^2\omega_{110}^2\epsilon_0^2\pi}{2\sigma\delta_{110}k_{110}^2} J_1'^2(bk_{110}) \quad (2.86)$$

The $P_{in}^{(2)}$ in equation 2.84 is

$$P_{in}^{(2)} = \frac{C^2\omega_{110}^2\epsilon_0^2\pi}{\sigma\delta_{110}k_{110}^2} \left(\int_0^b J_1'^2(rk_{110}) r dr + \frac{1}{k_{110}^2} \int_0^b \frac{J_1^2(rk_{110})}{r} dr \right) \quad (2.87)$$

P_{in110} according equations 2.84, 2.87, 2.86 is

$$P_{in110} = \frac{C^2 \omega_{110}^2 \epsilon_0^2 \pi}{\sigma \delta_{110} k_{110}^2} \left(\frac{bL}{2} J_1^2(bk_{110}) + \int_0^b J_1^2(rk_{110}) r dr + \frac{1}{k_{110}^2} \int_0^b \frac{J_1^2(rk_{110})}{r} dr \right) \quad (2.88)$$

β_{110} coupling factor is

$$\beta_{110} = \frac{\mu_0^2 \omega_{110}^2 L^2 \sigma \delta_{110}}{\pi \cdot 100 \Omega} \frac{\left(\int_{b-l}^b J_1'(xk_{110}) \cdot dx \right)^2}{\frac{bL}{2} J_1^2(bk_{110}) + \int_0^b J_1^2(rk_{110}) r dr + \frac{1}{k_{110}^2} \int_0^b \frac{J_1^2(rk_{110})}{r} dr} \quad (2.89)$$

We have $b = 0.111$ m, $l = 0.02$ m, $k_{110} = 34.5$ and we get

$$\int_{b-l}^b J_1'(xk_{110}) \cdot dx \approx 0.008 \quad (2.90)$$

$$\int_0^b J_1^2(rk_{110}) \cdot r dr \approx 0.00065 \quad (2.91)$$

$$\frac{1}{k_{110}^2} \int_0^b \frac{J_1^2(rk_{110})}{r} dr \approx 0.00035 \quad (2.92)$$

Putting equations 2.90, 2.91, 2.92 in equation 2.89 we get

$$\beta_{110} = 151 \quad (2.93)$$

where $L = 0.018$ m, $\mu_0 = 4\pi \cdot 10^{-7} [\frac{Vs}{Am}]$, $\sigma = 3.6 \cdot 10^6 [\Omega^{-1}m^{-1}]$, $\delta_{110} = 0.07 \cdot 10^{-4}$ [m], $\omega_{110} = 9.48 \cdot 10^9$ [Hz].

The value in equation 2.93 is tested by GdfidL, see table 2.2

| | Theor. | GdfidL |
|---------------|--------|--------|
| β_{110} | 151 | 97 |

Table 2.2: Test of the theoretical computation of the coupling factor of the dipole mode

Electric coupling: Let us discuss the coupling of the first monopole mode. The electric field of the mode is shown in figure 2.13 and is given by equation 2.52. The pin-antenna with length l and diameter d couples the following amount of electric flux from the cavity (see figure 2.17)

$$\Phi_{ec} = \int_0^{2\pi} \int_0^{G(l+d/2)} E_0 \cdot J_0(rk) \cdot e^{i\omega t} \cdot r d\varphi \cdot dr \quad [\text{Vm}] \quad (2.94)$$

with some constant G . The pin-antenna couples more electrical fluxes by increasing either the length or the width of the antenna, see figure 2.17.

The ratio between the electrical flux Φ_{ec} coupled by the pin-antenna and the whole electrical flux in the cavity Φ_e is

$$n = \frac{\Phi_{ec}}{\Phi_e} \quad (2.95)$$

where

$$\Phi_e = \int_0^{2\pi} \int_0^b E_0 \cdot J_0(rk) \cdot e^{i\omega t} \cdot r d\varphi \cdot dr \quad [\text{Vm}] \quad (2.96)$$

The constant G can be defined from the condition that when $l=0$ and $d \rightarrow 2b$ the whole electric flux should be coupled. Putting $l=0$, $d=2b$ in the equation 2.95, from the condition $n=1$ we get

$$G = 1 \quad (2.97)$$

So, putting equations 2.97, 2.96, 2.94 in equation 2.95 we get

$$n = \frac{\int_0^{l+d/2} J_0(rk) \cdot r dr}{\int_0^b J_0(rk) \cdot r dr} \quad (2.98)$$

The coupled electrical flux Φ_{ec} produces surface charge q on the pin-antenna

$$q = \epsilon_0 \Phi_{ec} = \int_0^{2\pi} \int_0^{l+d/2} \epsilon_0 E_0 \cdot J_0(rk) \cdot e^{i\omega t} \cdot r d\varphi \cdot dr \quad [\text{C}] \quad (2.99)$$

The coupled current is

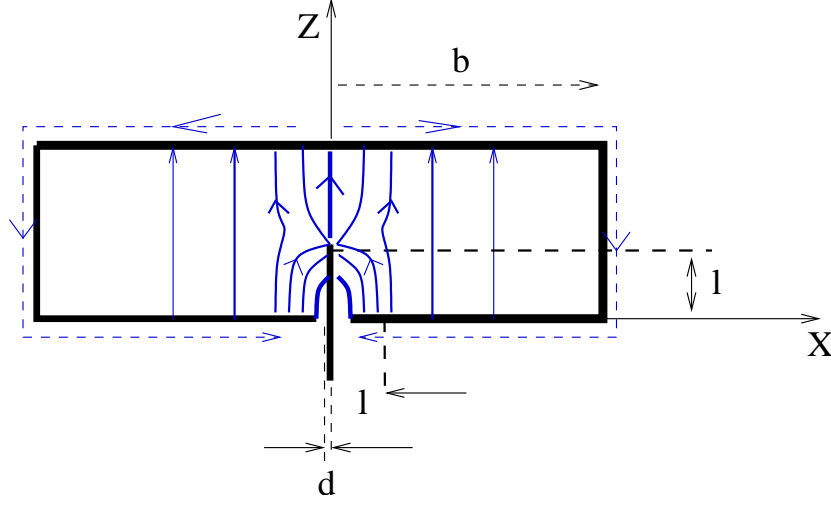


Figure 2.17: The cavity coupled by pin-antenna: The blue full lines are electrical flux, dashed blue lines show wall current of TM_{010} mode inside the cavity with radius b

$$I = \frac{dq}{dt} = i\omega\epsilon_0 2\pi E_0 \int_0^{l+d/2} J_0(r \cdot k) \cdot r dr \quad [A] \quad (2.100)$$

where

$$\int_0^{l+d/2} J_0(r \cdot k) \cdot r dr = \frac{l + d/2}{k} J_1[k(l + \frac{d}{2})] \quad (2.101)$$

So, the coupled power into the 50Ω line is

$$P_c = \frac{I^2 \cdot 50\Omega}{2} = 100\pi^2 \omega^2 \epsilon_0^2 E_0^2 \frac{(l + d/2)^2}{k^2} J_1^2[k(l + \frac{d}{2})] \quad (2.102)$$

To compute the dissipated power in the cavity we use equations 2.68 and 2.75 together with following relation

$$|H_\varphi|^2 = |E_z|^2 \frac{\epsilon_0}{\mu_0} \quad (2.103)$$

and we get

$$P_{in} = \frac{\epsilon_0 \pi b E_0^2 J_1^2(bk)}{\mu_0 \sigma \delta} (L + b) \quad (2.104)$$

At the end the β coupling factor is

$$\beta = \frac{P_c}{P_{in}} = 100\pi\omega^2\epsilon_0\mu_0\sigma\delta \frac{(l + d/2)^2 J_1^2[k(l + \frac{d}{2})]}{bk^2(L + b)J_1^2(bk)} \quad (2.105)$$

Let us use the same example as with magnetic coupling but $l = 9$ mm and $d/2 = 0.9$ mm, and we get

$$\beta \approx 1.1 \quad (2.106)$$

For comparison see table

| | Theor. | GdfidL |
|---------|--------|--------|
| β | 1.1 | 0.7 |

Table 2.3: Test of the theoretical computations of pin-antenna coupling

Electric coupling of the dipole mode TM_{110} : Suppose the coupling pin-antenna is in place $p = 0.068$ m, with length $l = 0.0076$ m, and diameter $d = 0.0018$ m, see figure 2.18.

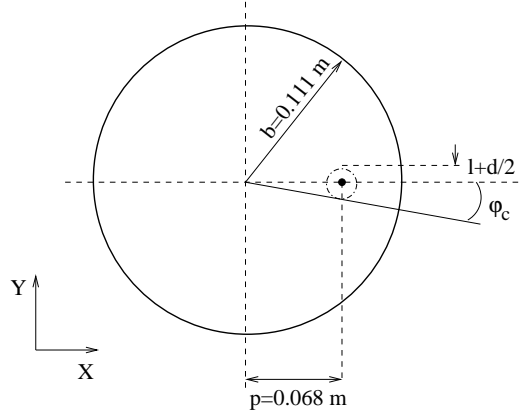


Figure 2.18: The top view on the cavity with the coupling pin-antenna

The coupled electric flux produces surface charge

$$q = \int_{-\varphi_c}^{\varphi_c} \int_{0.068}^{0.076} \epsilon_0 C \cos \varphi J_1(rk_{110}) \cdot e^{i\omega_{110}t} \cdot r d\varphi \cdot dr \quad [\text{C}] \quad (2.107)$$

where $\varphi_c = 0.125$ and C has dimension [V/m].

The coupled current analog to equation 2.100 is

$$I_{110} = 0.25 \cdot i\omega_{110} \int_{0.068}^{0.076} \epsilon_0 C J_1(rk_{110}) \cdot r dr \quad [\text{A}] \quad (2.108)$$

The coupled power into the 50 Ω line is

$$P_{c110} = \frac{I_{110}^2 50\Omega}{2} = 0.25^2 \omega_{110}^2 \epsilon_0^2 C^2 \left(\int_{0.068}^{0.076} J_1(rk_{110}) \cdot r dr \right)^2 \cdot 25\Omega \quad (2.109)$$

In the cavity dissipated power P_{in110} is done by equation 2.88 and the coupling factor β_{110} is

$$\beta_{110} = \frac{P_{c110}}{P_{c110}} = \frac{0.25^2 25\Omega \sigma \delta_{110} k_{110}^2}{\pi} \frac{\left(\int_{0.068}^{0.076} J_1(rk_{110}) \cdot r dr \right)^2}{\frac{bL}{2} J_1^2(bk_{110}) + \int_0^b J_1^2(rk_{110}) r dr + \frac{1}{k_{110}^2} \int_0^b \frac{J_1^2(rk_{110})}{r} dr} \quad (2.110)$$

Here $\sigma = 3.6 \cdot 10^6 \Omega^{-1} m^{-1}$, $\delta_{110} = 0.07 \cdot 10^{-4} \text{ m}$, $k_{110} = 34.5 \text{ m}^{-1}$ and we have

$$\int_{0.068}^{0.076} J_1(rk_{110}) \cdot r dr = 0.0002856 \quad (2.111)$$

Putting equation 2.111 in equation 2.110 and using equations 2.91, 2.92 we get

$$\beta_{110} = 0.88 \quad (2.112)$$

In the table 2.4 we list the value in equation 2.112 and the value computed by the GdfidL

| | Theor. | GdfidL |
|---------------|--------|--------|
| β_{110} | 0.88 | 1 |

Table 2.4: Test of the of theoretical computations of the electric coupling of the dipole mode

where

$$gM(k'_z) = \frac{1}{jk'_z} \left[e^{jk'_z g/2} - e^{-jk'_z g/2} \right] = g \frac{\sin k'_z g/2}{k'_z g/2} \quad (2.119)$$

or

$$A(k'_z) = E_0 g \frac{M}{2\pi J_1(Ka)} \quad (2.120)$$

Particle travels with c_0 along $\rho = \delta$, $\varphi = 0$ and experiences the voltage

$$\begin{aligned} V_z &= \frac{E_0 g}{2\pi} \int_{-\infty}^{\infty} dz e^{j\omega t} \int_{-\infty}^{\infty} M \frac{J_1(K\delta)}{J_1(Ka)} e^{-jk_z z} dk_z = \\ &= \frac{E_0 g}{2\pi} \int_{-\infty}^{\infty} dk_z M \frac{J_1(K\delta)}{J_1(Ka)} \int_{-\infty}^{\infty} e^{j(k-k_z)z} dz \end{aligned} \quad (2.121)$$

Here $\int_{-\infty}^{\infty} e^{j(k-k_z)z} dz = 2\pi \cdot \delta(k - k_z)$, finally we have

$$V_z = E_0 g M(k) \frac{\delta}{a} \quad (2.122)$$

We took into account that $\frac{J_1(K\delta)}{J_1(Ka)} = \frac{\delta}{a}$ for $K \rightarrow 0$.

2.2.4 Damping time of the cavity and the distance between bunches

In case of TESLA the distance between bunches in the beam is $t_b = 337\text{ns}$, see figure 2.20. The cavity characteristic damping time τ is the time after which the mode in the cavity is damped by factor of e :

$$E = E_0 \cdot e^{-\frac{t}{\tau}} \quad (2.123)$$

When the bunch train goes through the cavity, in each period of time t_b the cavity is excited again and again. Within the time t_b , dipole mode do not disappear completely.

Suppose $E_1 = E_0 \cdot \cos \varphi$ is the field of the dipole mode excited by the first bunch, φ is its phase. After the second bunch the field can be given like

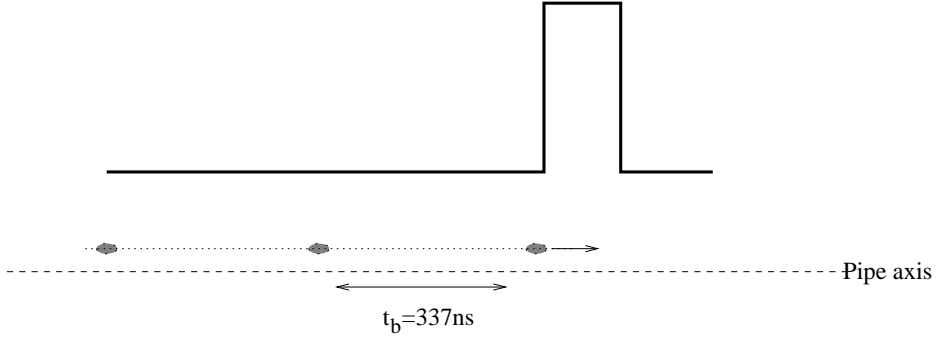


Figure 2.20: TESLA beam

$$E_2 = \left(E_0 + E_0 \cdot e^{-\frac{t_b}{\tau_{110}}} \cdot \cos \varphi' \right) \cos \varphi \quad (2.124)$$

where φ' is the phase of the dipole mode at the time t_b .

For the whole bunch-train this process can be described by the following equation

$$E = E_0 \left(1 + \cos \varphi' e^{-\frac{t_b}{\tau_{110}}} (1 + \cos \varphi' e^{-\frac{t_b}{\tau_{110}}} (1 + \dots)) \cdot \cos \varphi \quad (2.125)$$

Suppose $\cos \varphi' = 1$. This corresponds to $t_b = nT_{110}$ ($n = 0; 1; 2 : \dots$). T_{110} is the period of the dipole mode oscillation. In this case the fields of each excited dipole mode will be added

$$E = E_0 + E_0 e^{-\frac{t_b}{\tau_{110}}} + E_0 e^{-2\frac{t_b}{\tau_{110}}} + E_0 e^{-3\frac{t_b}{\tau_{110}}} + \dots \quad (2.126)$$

Equation (2.126) is a geometrical series like

$$S = a_1 + a_1 q + a_1 q^2 + a_1 q^3 + \dots = \frac{a_1}{1 - q}, \quad \text{if } |q| < 1 \quad (2.127)$$

Now, if we compare equations (2.126) and (2.127) we get

$$q = e^{-\frac{t_b}{\tau_{110}}} < 1 \quad (2.128)$$

hence, (2.126) becomes

$$E = \frac{E_0}{1 - e^{-\frac{t_b}{\tau_{110}}}} \quad (2.129)$$

As an example let us input parameters from Lorenz cavity BPM [16]. So $\tau_{110} = 182.6$ ns and suppose $nT_{110} = t_b = 337$ ns. Putting this in (2.129) we get

$$E = \frac{E_0}{1 - e^{-\frac{337}{182.6}}} \approx \frac{E_0}{0.84} \quad (2.130)$$

For further analysis of pill-box cavity BPM see chapter 4.

2.2.5 Cutoff frequencies of the beam-pipe

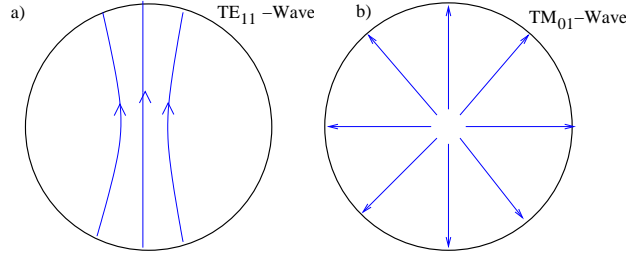


Figure 2.21: a: The cross-section of the beam-pipe with E field of the TE_{11} wave; b: the cross-section of the beam-pipe with E field of the TM_{01} wave

The dipole mode TM_{110} will be coupled away into the beam-pipe if its frequency is higher than the lowest cutoff frequency of the beam-pipe.

The lowest cutoff frequency [37], [38] for a beam-pipe with 78 mm diameter is for the TE_{11} wave (sometimes symbol H_{11}^O is used) and is equal to 2.25 GHz, see figure 2.21,a.

For TM_{mn} (or E_{mn}^O) type waves the lowest cutoff frequency is for the TM_{01} wave and is equal to 2.94 GHz, see figure 2.21,b.

The smaller the radius of the beam-pipe is the higher the cut off frequencies are.

Chapter 3

Cross-talk problem in pill-box cavity BPMs

The cross-talk isolation factor (in this paper marked as K [dB]) is one of the most important parameters of cavity BPMs. It shows how good the signals corresponding to the bunch x and y offsets are isolated from each other.

There is always some coupling between the signals corresponding to the bunch x and y deflections. It means that if the bunch is deflected in x -direction only, we will detect some signal corresponding to an y -deflection, too [34].

In this chapter we analyse in detail this phenomenon: Cross-talk mechanism is illustrated. Solutions of minimal cross-talk performance are given.

At the end of the chapter we apply perturbation theory method. With this method we compute theoretically frequency changes caused by cavity wall perturbation.

3.1 Cavity without coupling antennas

In reality there are always some small distortions of the cavity symmetry due to fabrication tolerances, welding procedure, beam-pipe ellipticity etc. All these distortions together can be treated in a simplified manner by considering the cavity as slightly elliptically deformed.

Because of the ellipticity of the monitor two dipole modes with a small difference in frequencies are excited, with polarizations perpendicular to each other in coincidence with the axes of the ellipse, figure 3.1. This effect was seen by computer simulations.

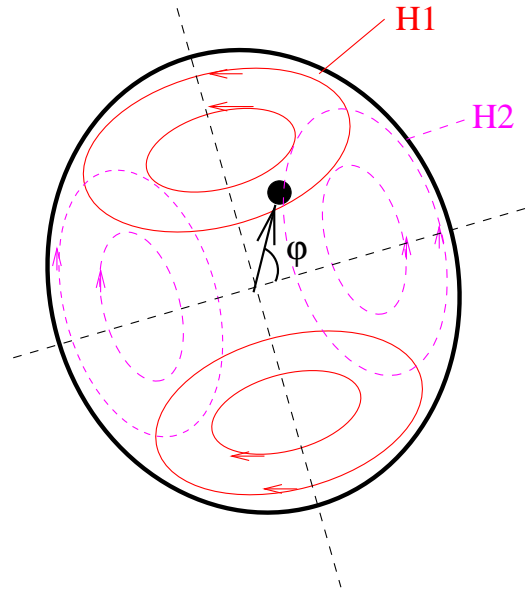


Figure 3.1: The cut of cylindrical cavity with small ellipticity and magnetic fields of two excited dipole modes. Their polarizations are perpendicular to each other. The black spot is at the position of the beam

Now, when the beam goes through the cavity with some displacement two dipole modes are excited with polarizations fixed by the ellipse (see figure 3.1), and the larger the beam displacement the stronger the dipole modes are excited. In dependence of the φ -angle of the displacement one of the two dipole modes will be excited stronger than the other.

The point is that cavity distortions caused by fabrication, welding etc. are out of control. Hence, the orientation of the axis of the ellipse is basically unpredictable.

3.1.1 Cavity with four coupling antennas

Antennas also play a role for dipole mode polarization. When they are perfect symmetrically mounted into the cavity, they force the dipole modes to take one of the two possible polarizations shown in figure 3.2, as simulated by the computer code GdfidL [5].

As mentioned in the previous section, there are always some slight distortions

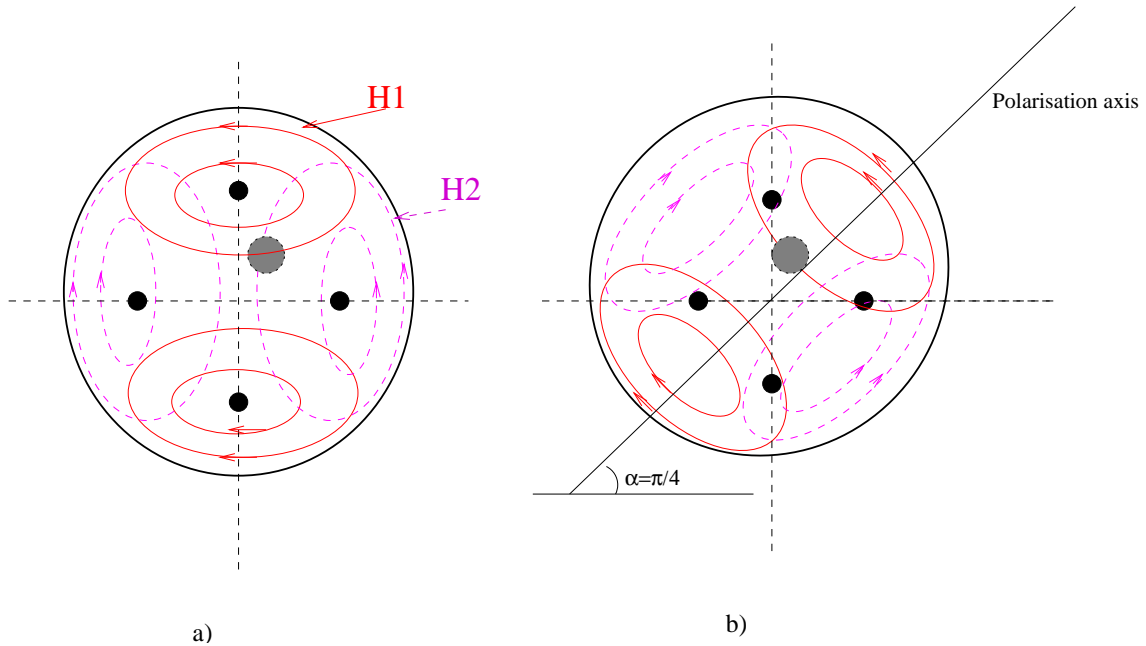


Figure 3.2: The possible polarizations of the dipole modes in a perfectly symmetrical cavity with four antennas. The small four black spots are the coupling antennas, the bigger one is the beam: a) the dipole mode polarizations are matched with coupling antennas axis. b) the dipole mode polarizations and coupling antennas axes have $\pi/4$ mismatch.

of the cavity symmetry, and these distortions decide which case, figure 3.2a or figure 3.2b, will take place. Again, the beam itself plays no role for selecting the dipole mode polarization.

3.1.2 Reality

Suppose we did good computations and want to build a cylindrical cavity pick-up station with *cross-talk* isolation of 30 dB.

It is worth to discuss the following two cases:

- 1) **weak antenna coupling**
- 2) **strong antenna coupling**

In the case of **weak antenna coupling** distortion effects described in section 3.1.1 play the dominant role and effects from the antennas are neglected for dipole mode polarization. It means that the orientation of the polarization

axis is determined by the orientation of the cavity ellipticity, which can be anywhere. As a consequence, we will get a cavity with better or worse cross-talk performance depending on the angle α , see figure 3.3.

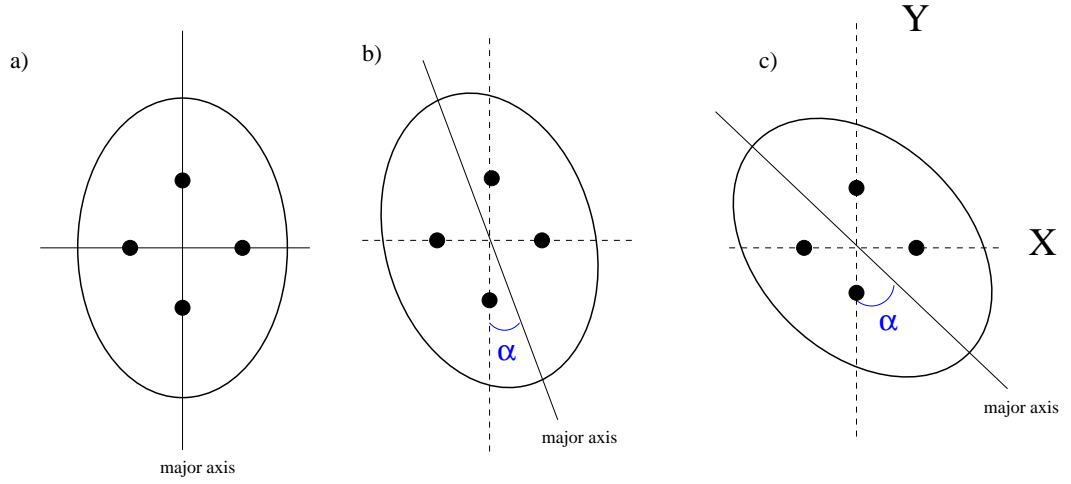


Figure 3.3: Various locations of the major axis of the ellipse.

Let us discuss the general case, second picture in figure 3.3, and the dipole mode corresponding to the major axis of this ellipse. The antenna in y -direction couples the following part from the signal V_{110}^y

$$V_y = V_{110}^y \cdot \cos \alpha \quad (3.1)$$

where V_{110}^y is the amount of the signal which the antenna couples from the mode with polarization exactly in y -direction (see [35]), in other words if $\alpha = 0$. The antenna in the perpendicular x -direction couples the following signal from this mode

$$V_x = V_{110}^y \cdot \sin \alpha \quad (3.2)$$

so that the cross-talk isolation between x - and y -directions in [dB] can be written as

$$Isolation [dB] = 20 \cdot \log \left(\frac{V_y}{V_x} \right) = 20 \cdot \log(\cot \alpha) \quad (3.3)$$

Note that the worst case occurs for $\alpha = 45^\circ$, see figure 3.2,b.

In the case of **strong antenna coupling**, antennas play the main role for fixing the dipole mode polarization. Now we will get either the desired polarization (figure 3.2a) with best isolation or the polarization in figure 3.2b with no isolation, $\alpha = \pi/4$ (equation 3.3).

3.1.3 Solution

In order to overcome the problem of unpredictable polarizations of dipole modes and to fix their orientations in a predetermined way we propose the following modification of the cavity: In x - (or y -) direction we generate a relative strong distortion, stronger than all unpredictable distortions discussed so far, for example, by introducing two stamp-eroded rectangular recesses into the cavity¹, as indicated in figure 3.4.

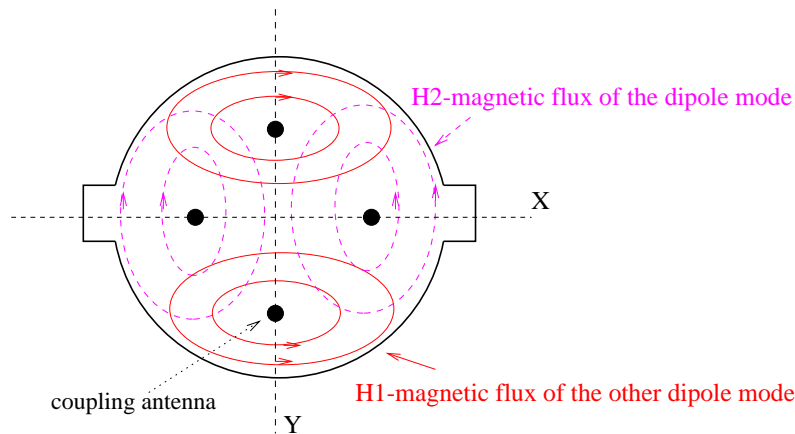


Figure 3.4: Forced ellipticity with desired orientation of the axis

In this way we force the cavity to behave as an ellipse with its major axis in coincidence with one of the antennas axes. Now, neither slight fabrication distortions nor influence of the antennas are strong enough to change this desired polarization of the dipole modes in unacceptably strong manner.

Such a forced polarisation of dipole modes was tested numerically, by GdfidL, see figures 3.5, 3.6.

¹More ellipticity results to bigger difference between the frequencies of the two dipole modes.

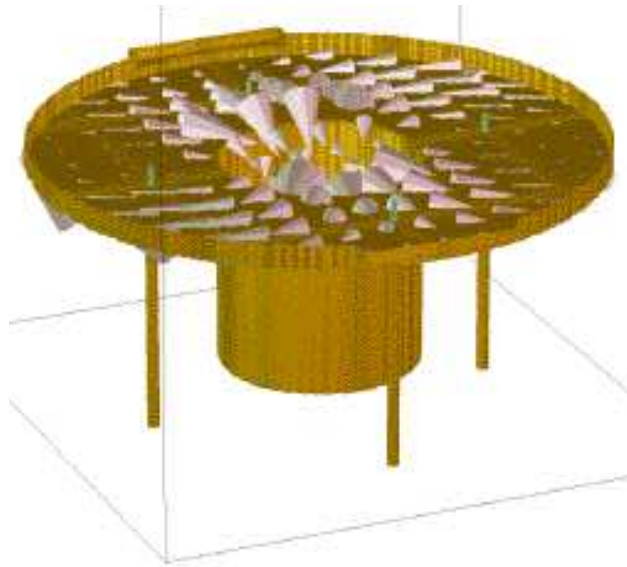


Figure 3.5: The first dipole mode polarized in y direction

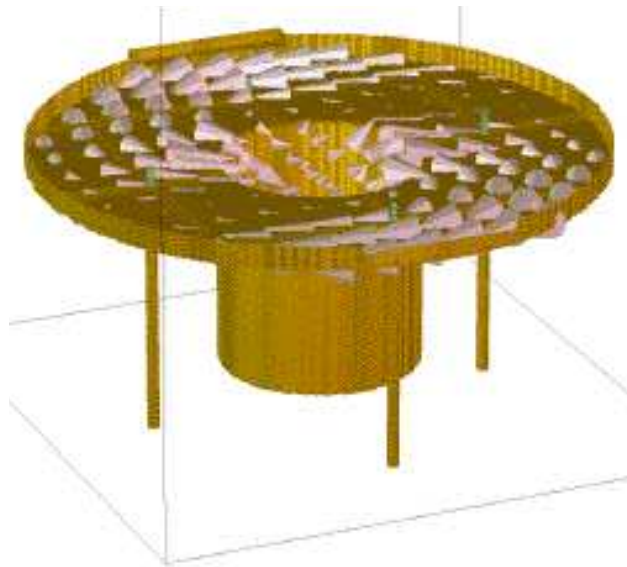


Figure 3.6: The second dipole mode polarized in x polarization

In figures 3.5 and 3.6 we see the magnetic flux of the dipole modes.

This proposal has been applied to a prototype of a new cavity BPM (see figure 4.1) for the TESLA cryomodules [3]. We have introduced two stamp-

eroded rectangular recesses of $64 \times 10 \text{ mm}^2$ with 4 mm depth into the cavity with precision of typically $50 \mu\text{m}$.

In figure 3.7 is the layout of the cross-talk measurement. The realization of cross-talk measurement is described in the next chapter, subsection 4.1.5. Here, in the table below we just list the data of the measurements before and after stamp-eroded rectangular recesses.

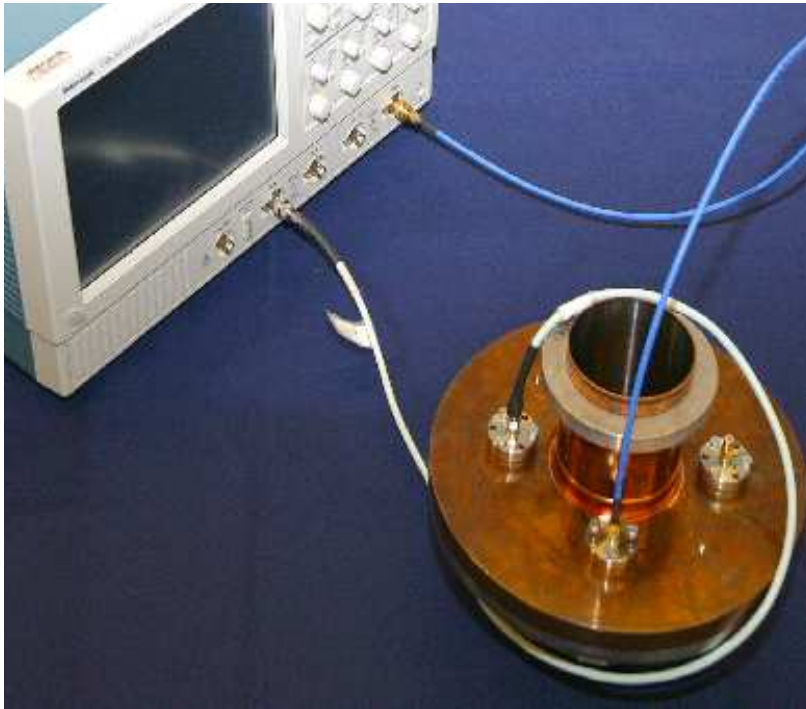


Figure 3.7: Layout of the cross-talk measurement

| | | | | |
|---------------|--------|-------------------|------------------|---------------|
| Cavity Length | 18 mm | | without recesses | with recesses |
| Cavity Radius | 111 mm | Isolation | 0 dB | 24 dB |
| Pipe Radius | 39 mm | $f_{H1} - f_{H2}$ | 300 KHz | 10 MHz |

Table 3.1: Prototype parameters and cross-talk isolation; frequency difference refers to figure 3.2 and figure 3.4, respectively

The cross-talk isolation is improved from 0 dB up to 24 dB. The cross-talk measured by the other ports was about the same.

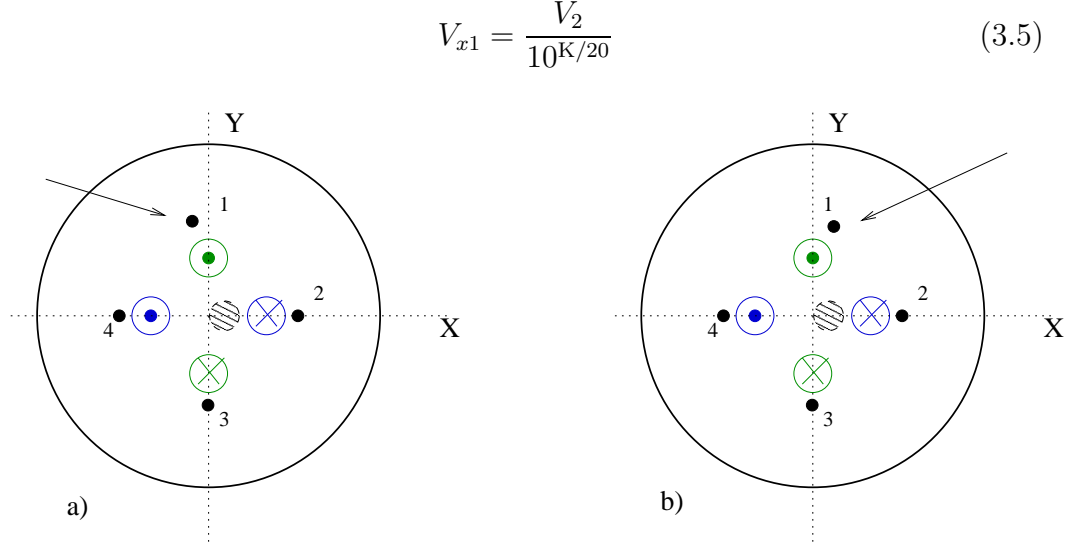


Figure 3.9: The same pill-box cavity as in figure 3.8 but the antenna 1 once shifted to the antenna 4 a), and once it is shifted to the antenna 2 b)

In the general case of an arbitrary off-set position the cross-talk effect for antennas 1 and 2 can be written in the following way

$$\begin{aligned} V'_1 &= V_1 \pm V_{x1} \\ V'_2 &= V_2 \pm V_{y2}, \end{aligned} \quad (3.6)$$

where V'_2 , V'_1 are values with coupling and V_2 , V_1 are the values with no cross-talk, V_{y2} is the coupled voltage from the dipole mode with y polarisation to the antenna 2 and is given analog to equation 3.5. So, using equation 3.5 system equation 3.6 becomes

$$\begin{aligned} V'_1 &= V_1 \pm \frac{V_2}{10^{K/20}} \\ V'_2 &= V_2 \pm \frac{V_1}{10^{K/20}}. \end{aligned} \quad (3.7)$$

For simplicity let us write equation 3.7 as

$$\begin{aligned} V'_1 &= V_1 \pm \frac{V_2}{\sigma} \\ V'_2 &= V_2 \pm \frac{V_1}{\sigma}, \end{aligned} \quad (3.8)$$

where $\sigma = 10^{K/20}$.

We have a system of two equations and two variables V_2 and V_1 . After solving we get

$$\begin{aligned} V_1 &= \frac{V'_1 \mp \frac{V'_2}{\sigma}}{1 - \frac{1}{\sigma^2}} \\ V_2 &= \frac{V'_2 \mp \frac{V'_1}{\sigma}}{1 - \frac{1}{\sigma^2}}. \end{aligned} \quad (3.9)$$

Having the voltages V'_1 and V'_2 with coupling we can use equation 3.9 to evaluate the error caused by the given cross-talk isolation performance.

Note that equations 3.9 are not defined in case when the cavity has no cross-talk isolation performance ($K=0$ dB, and σ becomes 1), which is quite natural.

In praxis when $K > 20$ dB we can approximate 3.9 to

$$\begin{aligned} V_1 &\approx V'_1 \mp \frac{V'_2}{\sigma} \\ V_2 &\approx V'_2 \mp \frac{V'_1}{\sigma}. \end{aligned} \quad (3.10)$$

Case b: Pill-box cavity with obvious ellipticity:

In this case polarizations of the dipole modes are strongly fixed, and by purpose a little bit change of the position of antennas (for example in range of $100 \mu\text{m}$) will not change the polarizations of the dipole modes, see figure 3.10.

Case b gives us the possibility to fix the "±" uncertainty in the system of equations 3.7. This can be achieved when we shift antenna position "a little bit" in our desired way. "A little bit" means bigger than the fabrication tolerances. Let us discuss the following shifts in figure 3.10.

In figure 3.10,a the voltages coupled by the antennas 2 and 4 are

$$\begin{aligned} V'_2 &= V_2 + V_{y2} \\ V'_4 &= V_4 + V_{y4} \end{aligned} \quad (3.11)$$

where V'_2 and V'_4 are the values with coupling, V_2 and V_4 are the values with no cross-talk. $V_{y2} \approx V_{y4}$ are cross-talk contributions from the dipole mode polarized in y direction, and both have the same phase.

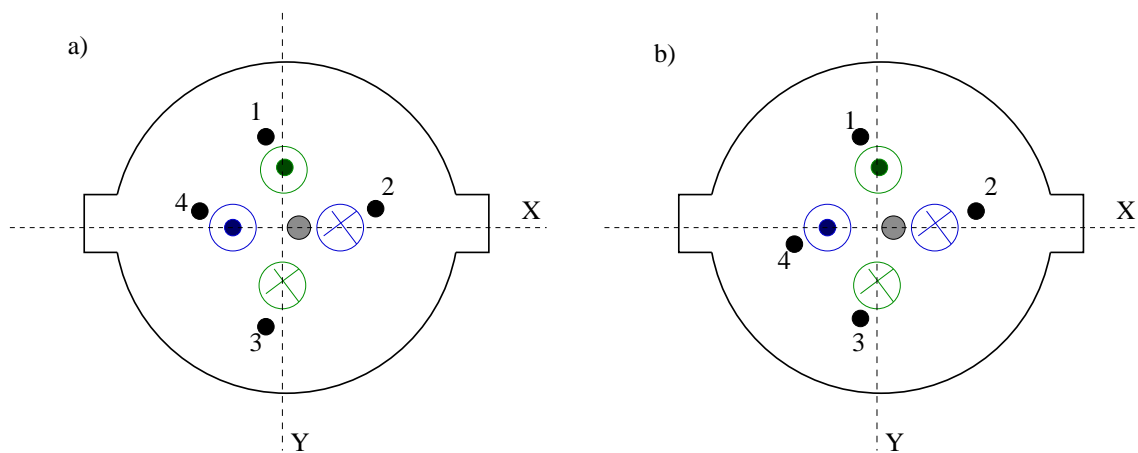


Figure 3.10: By purpose shifted antennas.

To show the advantage of the example of figure 3.10,a, let us look on the hybrids from the electronics, figure 3.11. As we see from the figure 3.11 after the hybrid the cross-talk contribution terms $V_{y2} \approx V_{y4}$ disappear as they were in phase.

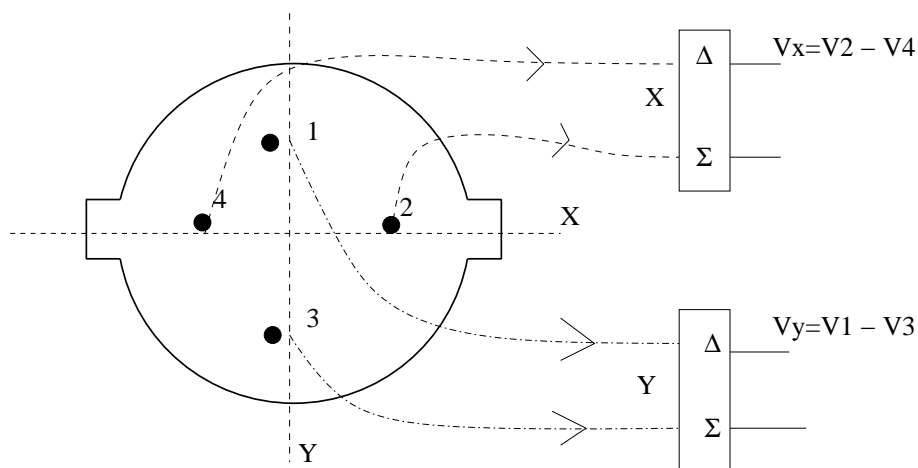


Figure 3.11: The pick-up station together with the hybrids

This is not the case if we had figure 3.10,b:

$$V_2' = V_2 + V_{y2} \quad (3.12)$$

$$V_4' = V_4 - V_{y4}, \quad (3.13)$$

where $|V_{y2}| \approx |V_{y4}|$ (in opposite phase) and after the hybrid $V_x = V_2 - V_4 + 2 \cdot V_{y2}$ we do not get rid of the cross-talk terms.

3.3 Perturbation of cavity walls

The perturbation method is useful to determine characteristic quantities, such as resonant frequencies, impedances, and so on.

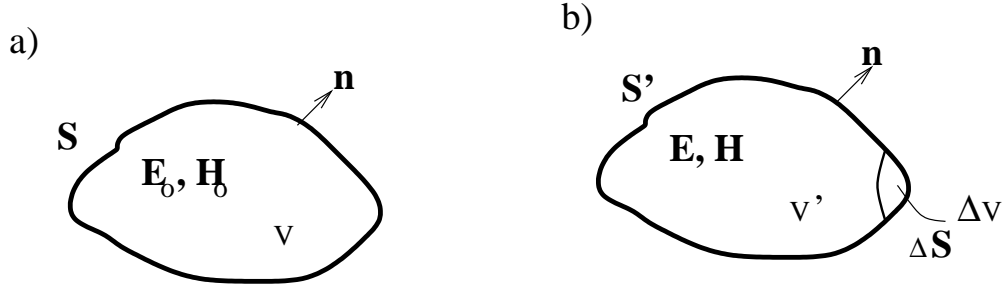


Figure 3.12: a: Original cavity; b: perturbed cavity

Figure 3.12,a represents a resonant cavity formed by a conductor with surface S enclosing the loss-free region V . Figure 3.12,b represents a deformation of the original cavity such that the conductor covers $S' = S - \Delta S$ and encloses $V' = V - \Delta V$.

The change in the resonant frequency due to the change of the cavity wall is determined as in [36]

$$\omega - \omega_0 = \frac{j \oint \mathbf{H} \times \mathbf{E}_0^* \cdot d\mathbf{s}}{\int_{V'} (\epsilon \mathbf{E} \cdot \mathbf{E}_0^* + \mu \mathbf{H} \cdot \mathbf{H}_0^*) dV} \quad (3.14)$$

$\mathbf{E}_0, \mathbf{H}_0, \omega_0$ represent the field and frequency of the original cavity, and let $\mathbf{E}, \mathbf{H}, \omega$ represent the corresponding quantities of the perturbed cavity.

The approximation to be made in equation 3.14 is that of replacing \mathbf{E}, \mathbf{H} by the unperturbed field $\mathbf{E}_0, \mathbf{H}_0$. For small perturbations this is certainly

reasonable in the denominator and should be valid in the numerator if the deformation is shallow and smooth. With this approximation the integral in the numerator of equation (3.14) becomes

$$\oint_{\Delta S} \mathbf{H} \times \mathbf{E}_0^* \cdot d\mathbf{s} \approx \oint_{\Delta S} \mathbf{H}_0 \times \mathbf{E}_0^* \cdot d\mathbf{s} = j\omega_0 \int_{\Delta V} (\epsilon|E_0|^2 - \mu|H_0|^2) \cdot dV \quad (3.15)$$

Substituting this into equation (3.14) we have

$$\frac{\omega - \omega_0}{\omega_0} \approx \frac{\int_{\Delta V} (\mu|H_0|^2 - \epsilon|E_0|^2) \cdot dV}{\int_V (\mu|H_0|^2 + \epsilon|E_0|^2) \cdot dV} \quad (3.16)$$

It is evident from the preceding equations that an *inward* perturbation will *raise* the resonant frequency if it is made at a point of large H , and will *lower* the resonant frequency if it is made at a point of large E . The opposite behavior results from an outward perturbation. It is also evident that the greatest changes in resonant frequency will occur when the perturbation is at a position of maximum E and zero H , or vice versa.

- The dipole mode frequency perturbation of the prototype due to two rectangular recesses (see figure 3.4):

The electro-magnetic fields of the dipole mode TM_{110} are

$$\begin{aligned} E_z &= C \cdot J_1(rk) \cdot \cos \varphi \\ H_\varphi &= -iC \frac{\omega\epsilon_0}{k} \cdot J_1'(rk) \cdot \cos \varphi \\ H_r &= -iC \frac{\omega\epsilon_0}{k^2 r} J_1(rk) \cdot \sin \varphi \end{aligned} \quad (3.17)$$

where C is a constant value with dimension [V/m].

In this particular case the perturbation is in the place of maximum magnetic field H_φ^{max} of the mode ($\varphi = 0$), and equation 3.16 can be written as

$$\frac{f - f_{110}}{f_{110}} \approx \frac{\mu_0 (H_\varphi^{max})^2 \cdot \Delta V}{2 \int_V \epsilon_0 |E_z|^2 dV} = \frac{[J_1'(Rk)]^2 \cdot \Delta V}{\pi R^2 l \cdot J_0(Rk) \cdot J_2(Rk)} \approx \frac{\Delta V}{\pi R^2 l} \quad (3.18)$$

We have also used the condition

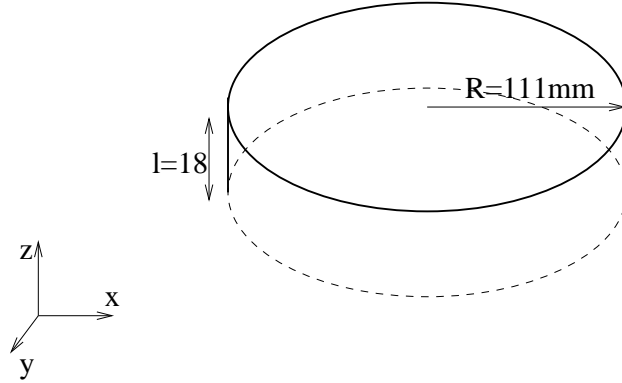


Figure 3.13: Unperturbed pill-box cavity

$$\int_V \mu_0 |H_0|^2 \cdot dV = \int_V \epsilon_0 |E_0|^2 \cdot dV, \quad (dV = r d\varphi \cdot dr \cdot dz) \quad (3.19)$$

which takes place for resonating modes.

$\Delta V = (4\text{mm} \times 64\text{mm} \times 10\text{mm}) \cdot 2 = 5.12 \cdot 10^{-6} \text{ m}^3$ is the change of the volume caused by two rectangular recesses in figure 3.4. $f_{110} = 1.5 \text{ GHz}$, $R = 111 \text{ mm}$, $l = 18 \text{ mm}$ and from equation 3.18 we get

$$\Delta f \approx 11 \text{ [MHz]} \quad (3.20)$$

This computation is compared with the computations done by GdfidL:

| | Pert. theor. | GdfidL |
|------------|--------------|--------|
| Δf | 11 MHz | 8 MHz |

Table 3.2: Δf computed by perturbation theory and GdfidL

- The frequency perturbation due to coupling antennas:

We suppose the antenna is in the place of maximum E field of the dipole mode TM_{110} . Electrical field of the mode TM_{110} is given by equation system 3.17. From equation 3.16 we get

$$\frac{f - f_{110}}{f_{110}} \approx \frac{\epsilon_0 (E^{max})^2 \cdot \Delta V}{2 \int_V \epsilon_0 |E|^2 dV} = \frac{J_1^2(1.8) \cdot \Delta V}{2\pi l \int_0^R J_1^2(r \cdot k_{110}) \cdot r dr} \quad (3.21)$$

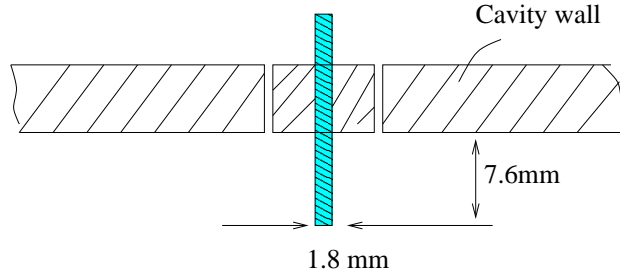


Figure 3.14: The coupling antenna

| | Pert. theor. | Measur. |
|------------|--------------|---------|
| Δf | 297 KHz | 153 KHz |

Table 3.3: Perturbation caused by couplig antennas

Having the dimensions of the coupling antenna (Figure 3.14) we get ΔV

$$\Delta V = 2 \cdot \pi \frac{d^2}{4} \cdot 7.6 = 38.66 \cdot 10^{-9} [m^3]. \quad (3.22)$$

$J_1(1.8) \approx 0.58$ and from equation 3.21

$$\Delta f \approx 297 \text{ [kHz]} \quad (3.23)$$

where according to [28]

$$\int_0^R J_1^2(r \cdot k_{110}) \cdot r dr = -\frac{R^2}{2} J_0(3.83) J_2(3.83) \approx 0.001 \text{ [m}^2\text{]} \quad (3.24)$$

We have tested this value with our prototype. The antenna position of the prototype is a little bit far from the maximum point² of the electrical field of the mode TM_{110} . That is why it was expected to get smaller Δf value as it is in equation 3.23.

The result of the measurement is in table 3.3.

²cavity radius 111 mm, maximum position of E-field 53 mm, antenna position 68 mm

Chapter 4

The Prototype

In this chapter is the whole description of the prototype BPM. The chapter consists of three sections: First section is about the pick-up station. In subsection 4.1.1 we bring the theoretical evaluation of the signals coupled at the dipole mode frequency. Then, we estimate the time- and position-resolution of the prototype. In subsections 4.1.3 and 4.1.4 we illustrate the frequency scan, Q_L and Q_0 measurements of the cavity. In a further subsection of the section 4.1 we illustrate the cross-talk measurement of the cavity.

The electronic circuit is described and tested in the second section.

At the end, in the third section, we perform the complete BPM test.

4.1 The pick-up station of the prototype

| | |
|-----------------------------------|--|
| material | stainless steel (1.4429) |
| shrinkage from 293K to 2K | 0.3 % |
| conductivity(293K) | $1.33 * 10^6 \Omega^{-1} \text{m}^{-1}$ |
| cond.(2K) | $1.88 * 10^6 \Omega^{-1} \text{m}^{-1}$ |
| material | copper (RRR=6.9) |
| conductivity(293K) | $3.569 * 10^6 \Omega^{-1} \text{m}^{-1}$ |
| cond.(2K) | $24.84 * 10^6 \Omega^{-1} \text{m}^{-1}$ |
| Cavity diameter | 222mm (at cryogen 221.3mm) |
| Beam-pipe diameter | 78mm (at cryogen 77.8mm) |
| Cavity length | 18mm (at cryogen 17.9mm) |
| Coupling antenna depth / diameter | 7.6mm / 1.8mm |

Table 4.1: Dimensions of the cavity and material parameters

A cylindrical pill-box cavity prototype is constructed, figure 4.1. The

pick-up station is fabricated from stainless steel. Dimensions and material properties of the structure are listed in table 4.1. The inside of the cavity is copper plated with special copper $RRR=6.9$. RRR means Room Resistivity Ratio. The number 6.9 is the ratio between conductivities at 4 K and room temperature.

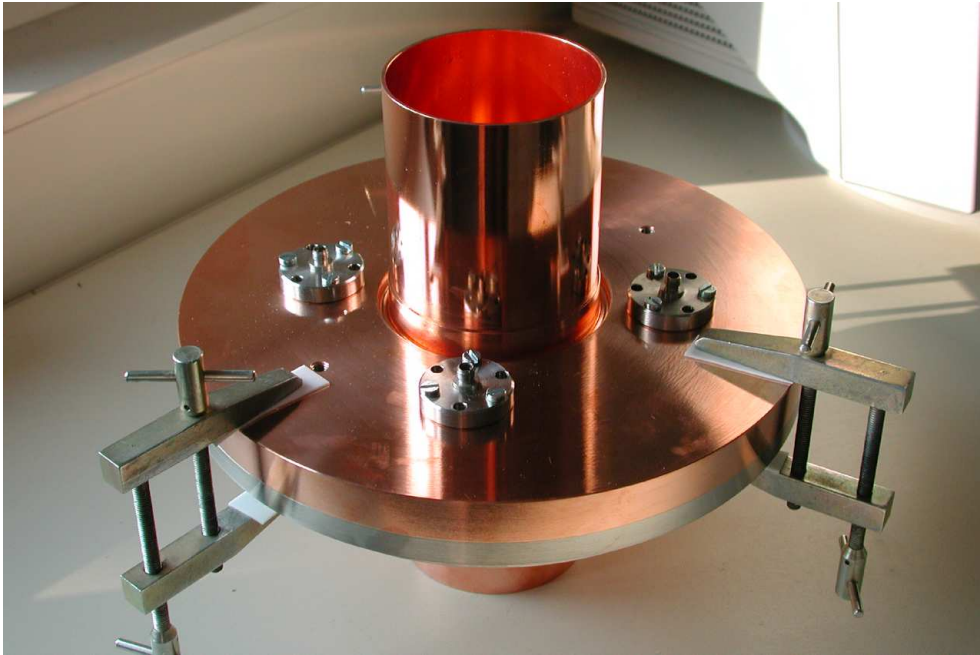


Figure 4.1: Prototype of the pick-up station with four symmetrically arranged feed-throughs

In figure 4.2 we see one of the four signal coupling pin-antennas. They fulfill the conditions of Ultra High Vacuum. The pin-antenna consists of two parts, see figure 4.3. These two parts are welded together. The technical design of the pin-antenna is done in appendix C. The antennas are joined with the cavity by packing material (HELICOFLEX type HN 100) between them.

Figure 4.4 illustrates the copper plating of the cavity. There is a small section free of copper, because the welding technology needs copper free area, at least 6 mm from all sides. The copper plating is realized to reduce 1.1 W energy dissipation on the cavity walls to 0.46 W, see table 1.4. This energy dissipation happens when HOM's excited in accelerating structures of the module move through the module like photons and interact with non-



Figure 4.2: One of the four coupling antennas



Figure 4.3: Two parts of the antenna

superconducting parts (for non-superconducting parts see table 1.2). A path of a photon interactions with the cavity walls is illustrated in figure 4.5. We see that there are much less interactions in the cylindrical surface of the cavity than on other parts. And we expect that the copper-free area in figure 4.4 interacts less with the photons than other parts of the cavity.

The values in table 1.4 do not include dissipation of the energy stored in the resonating modes of the BPM. The calculation of the energy per second stored in the resonating modes of the BPM is illustrated in subsection 4.1.6 and is equal to

$$P = 27.9 \text{ [mW]}. \quad (4.1)$$

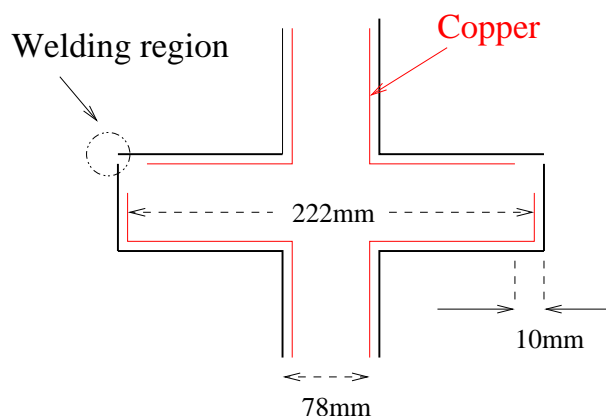


Figure 4.4: The interior of the cavity

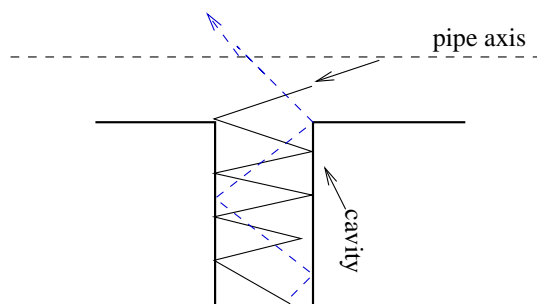


Figure 4.5: Photon (high order mode from the accelerating module) interactions in the cavity

Two rectangular recesses are eroded symmetrically inside the cavity, see figure 4.6. The recesses are done to minimize cross-talk, see chapter 3.

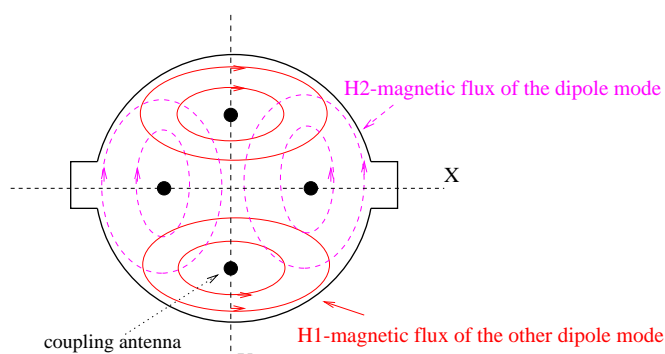


Figure 4.6: Cross-section of the cavity with two rectangular recesses

Fabricational tolerances listed in table 4.2 change the TM_{110} -dipole mode frequencies. Column 3 in table 4.2 shows how sensitive the frequency of the dipole mode (1.5 GHz, on x axis) is to $100 \mu\text{m}$ changes of the cavity radius, length or beam-pipe radius.

| dimension | target [mm] | sensitivity ($\pm 100 \mu\text{m} \Delta$) | tolerances | shrinkage |
|-------------------------|----------------|---|-----------------------|--------------------|
| cavity radius R_{res} | 111 | ∓ 1.247 MHz | $\pm 10 \mu\text{m}$ | $-433 \mu\text{m}$ |
| cavity length l | 18 | ± 0.158 MHz | $\pm 100 \mu\text{m}$ | $-203 \mu\text{m}$ |
| beam pipe radius r | 39 | ∓ 0.305 MHz | $\pm 50 \mu\text{m}$ | $-146 \mu\text{m}$ |

Table 4.2: Sensitivity of the different mechanical parameters

With the help of the column 3 we compute the frequency changes corresponding to the fabricational tolerances listed in the column 4:

$$\Delta f(\delta R_{res}) = \mp 125 \text{ kHz}, \Delta f(\delta l) = \pm 158 \text{ kHz}, \Delta f(\delta r) = \mp 152 \text{ kHz}.$$

This results in the worst case error of ± 435 kHz

To summarize the effect of inaccuracies, we require that our electronics should be capable to handle the signal even if it is 435 kHz off the design frequency.

Column 5 shows shrinkage of the cavity from 293 K to 2 K.

4.1.1 Theoretical evaluation of the signals coupled at the dipole mode frequency

To evaluate the signal of the prototype we need the parameters of first monopole mode TM_{010} , second monopole mode TM_{020} , dipole mode TM_{110}^x with x -polarisation, dipole mode TM_{110}^y with y -polarisation. These parameters are calculated by computer code GdfidL [5] and are listed in table 4.3.

The definitions of the parameters in the table were given in section 2.2. x and y signs above some parameters in the table show that these parameters relate to the dipole mode polarized in x or y direction respectively.

In case of some offset of the TESLA bunch charge ($q=3.2$ nC), the signal which a pin-antenna couples from the cavity at the 1.5 GHz dipole mode frequency is

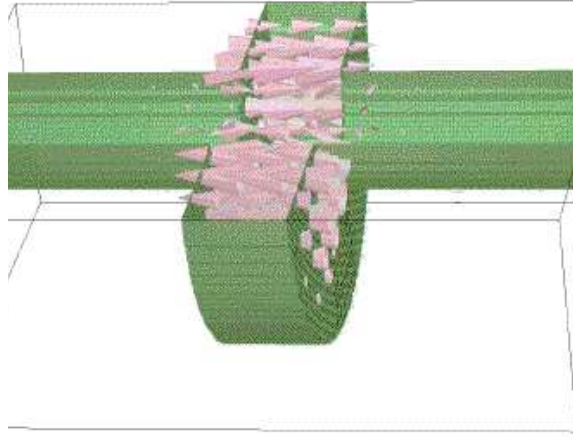
$$V^{out}(1.51 \text{ GHz}) = V_{110}^{out} + V_{010}^{out} + V_{020}^{out} + V_N \quad (4.2)$$

| | | | |
|--|-----------------|-----------------------|--------------------|
| $\frac{\beta_{110}^x/\tau_{110}^x}{\frac{R_{sh}^{110}(1mm)}{Q}}$ | 2.19 / 197.6 ns | | for 2 K (computed) |
| | 0.047 Ω | TM_{110}^x | 1.515 GHz |
| $\frac{\beta_{110}^y/\tau_{110}^y}{\frac{R_{sh}^{110}(1mm)}{Q}}$ | 2.2 / 208.7 ns | Q_0^{110}/Q_L^{110} | 3000 / 940 |
| | 0.047 Ω | TM_{110}^y | 1.525 GHz |
| $\frac{\beta_{010}/\tau_{010}}{\frac{R_{sh}^{010}(1mm)}{Q}}$ | 0.68 / 586.6 ns | Q_0^{110}/Q_L^{110} | 3200 / 990 |
| | 28 Ω | TM_{010} | 1.14 GHz |
| $\frac{\beta_{020}/\tau_{020}}{\frac{R_{sh}^{020}(1mm)}{Q}}$ | 2.2 / 216 ns | Q_0^{010}/Q_L^{010} | 3536 / 2100 |
| | 34.5 Ω | TM_{020} | 2.64 GHz |
| | | Q_0^{020}/Q_L^{020} | 5990 / 1791 |

Table 4.3: Calculated data of the modes of the prototype

The voltages in equation 4.2 are:

- V_{110}^{out} is the coupled voltage of the dipole mode.

Figure 4.7: The electric field of TM_{110} mode calculated by GdfidL

The mode pattern is shown in figure 4.7. Here we see the electric field of the mode TM_{110} .

V_{110}^{out} can be computed using equation (2.37) and the data from table 4.3.

$$V_{110}^{out}(x) = a \cdot x, \quad a = \pi f_{110} \sqrt{Z \left(\frac{1}{Q_L} - \frac{1}{Q_0} \right) \left(\frac{R_{sh}}{Q} \right)_{110}^{fix}} \cdot \frac{q}{x_{fix}} \quad (4.3)$$

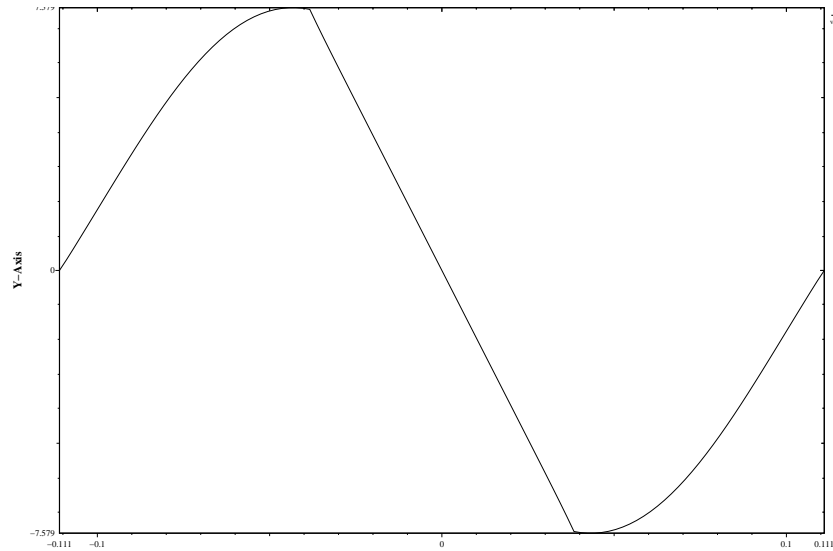


Figure 4.8: The voltage of the TM_{110} mode along the x axis; $(E_z e^{i\omega \frac{z}{c}}$ integrated over z

and is equal to 6.3 mV for $x = 10\mu\text{m}$.

- V_{010}^{out} is the coupled voltage of the common mode at the 1.512 GHz-dipole mode frequency, see chapter 2, figure 2.11.

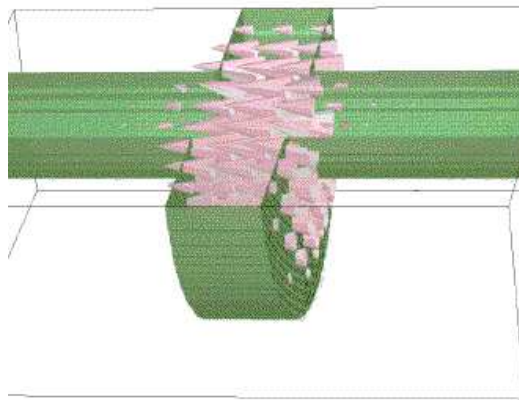


Figure 4.9: The electric field of TM_{010} mode calculated by GdfidL

The mode pattern is shown in figure 4.9.

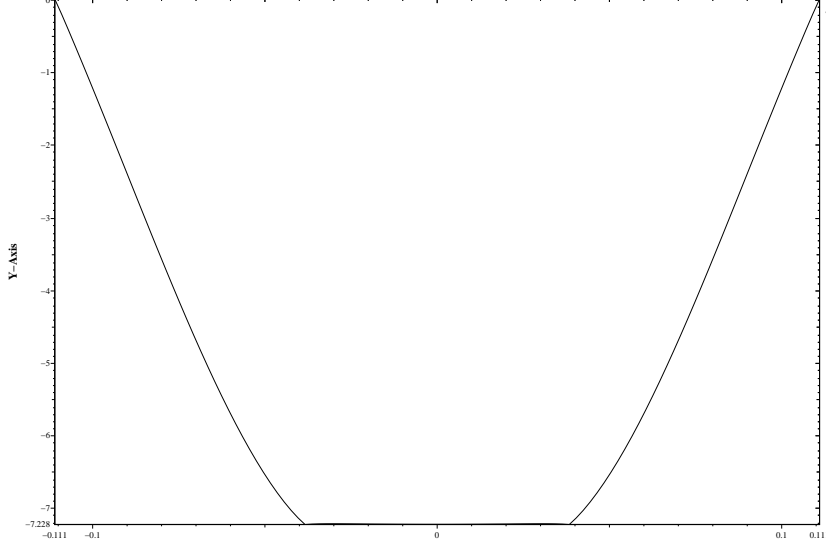


Figure 4.10: The voltage of the TM_{010} mode along the x axis; ($E_z e^{i\omega \frac{z}{c}}$ integrated over z)

V_{010}^{out} can be written as

$$V_{010}^{out} = V_{010}(f_{010}) \cdot h^{010}(f_{110}), \quad (4.4)$$

where $h^{010}(f_{110})$ is the leakage factor of the TM_{010} mode into f_{110} frequency. The leakage factor is derived from an equivalent parallel R, L, C circuit

$$h(f) = \frac{1}{\sqrt{1 + \alpha^2(f)}} \quad (4.5)$$

where $\alpha(f)$ is

$$\alpha(f) = 2Q_L \frac{f - f_0}{f_0}. \quad (4.6)$$

f_0 is the resonant frequency of the monopole mode and Q_L is its loaded quality factor, see figure 4.11. The presentation of the prototype as equivalent R, L, C circuit is correct around the resonant frequency. In subsection 4.1.7 is illustrated how good the equations 4.5 and 4.6 are for frequencies f far from the resonant frequency f_0 .

If we put the data from table 4.3 in equations 4.5, 4.6 for the first monopole mode we get

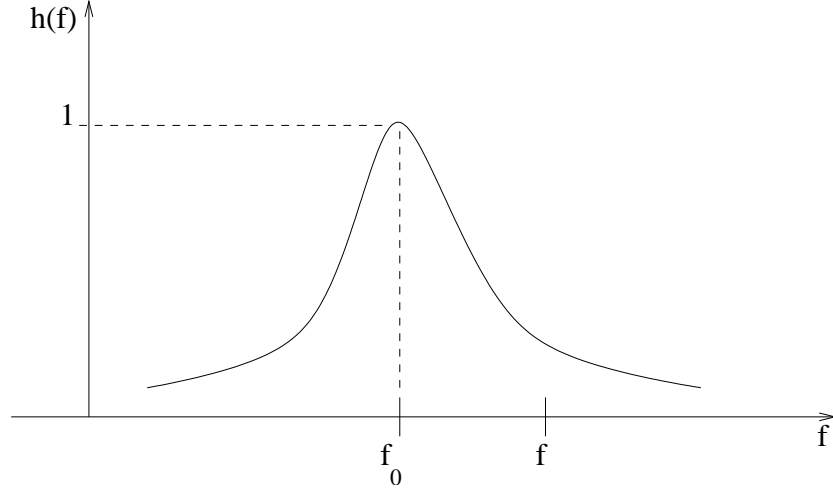


Figure 4.11: Resonant curve of some resonating contour R, L, C with resonant frequency f_0 and quality factor Q

$$h^{010}(f_{110}) = \frac{1}{\sqrt{1 + \alpha_{010}^2}} = 7.3 \cdot 10^{-4}, \quad \alpha_{010} = 2Q_L^{010} \frac{f_{110} - f_{010}}{f_{010}} = 1363 \quad (4.7)$$

$V_{010}(f_{010})$ can be computed by the analogy to equation (2.37) and from the fact that the voltage of the common mode is constant near the pipe-axis, see figure 4.10, and is equal to 5.9 V. Then according to equation (4.4) $V_{010}^{out} = 4.3$ mV.

TM₀₁₀ mode together with TM₀₂₀ mode has high shunt impedance over Q (see table 4.3) and is excited much stronger than the dipole mode. The second monopole mode besides its maximum on the pipe-axis has also a maximum not far from the coupling pin-antenna (see figure 4.13, 68mm is the pin-antenna place). Hence it will be coupled stronger than the first monopole mode.

- V_{020}^{out} is the coupled voltage of the second monopole mode at the dipole mode frequency, see figure 2.11.

The mode pattern is shown in figure 4.12. Here we see the electrical field of the mode TM₀₂₀.

V_{020}^{out} can be written as

$$V_{020}^{out} = V_{020}(f_{020}) \cdot h^{020}(f_{110}) \quad (4.8)$$

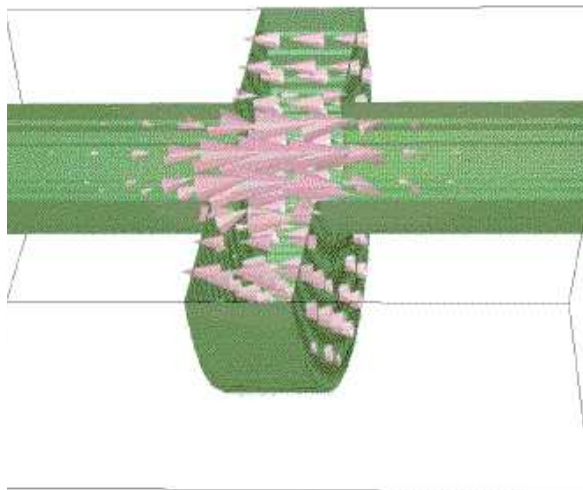


Figure 4.12: The electric field of TM_{020} mode calculated by GdfidL

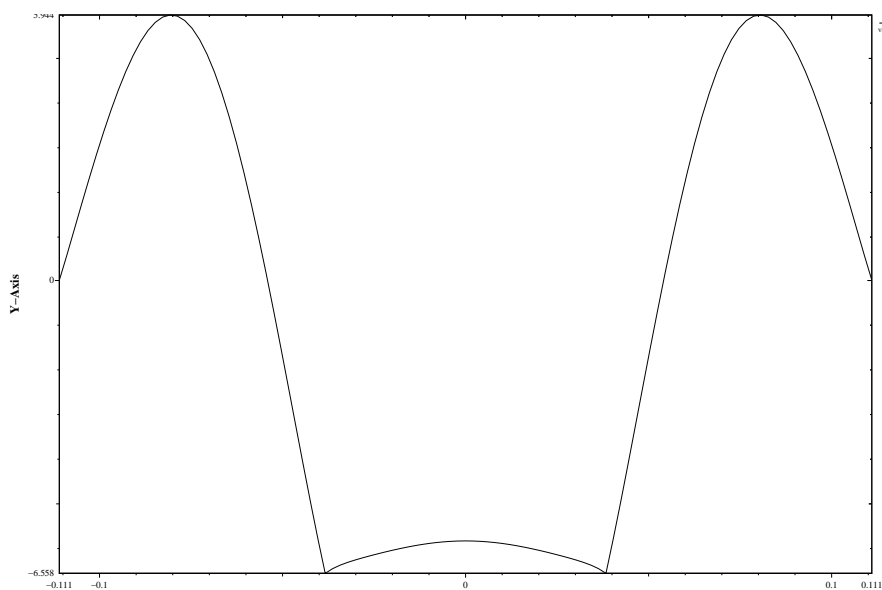


Figure 4.13: The voltage of the TM_{020} mode along the x axis; $(E_z e^{i\omega \frac{z}{c}}$ integrated over z)

where $h^{020}(f_{110})$ is the leakage factor of the TM_{020} mode into f_{110} frequency. $h^{020}(f_{110})$ is defined and computed in the way as $h^{010}(f_{110})$

$$h^{020}(f_{110}) = \frac{1}{\sqrt{1 + \alpha_{020}^2}} = 6.52 \cdot 10^{-4}, \quad \alpha_{020} = 2Q_L^{020} \frac{f_{110} - f_{020}}{f_{020}} = 1533 \quad (4.9)$$

$V_{020}(f_{020})$ is computed by analogy of the equation (2.37) and from the fact that the second monopole mode is assumed constant near the pipe-axis, see figure 4.13. $V_{020}(f_{020})$ is equal to 21.8 V. Then according to equation 4.8 $V_{020}^{out} \approx 13.9$ mV

It is not surprising that we have more contribution into the dipole mode frequency from the second monopole mode than from the first monopole mode. The second monopole mode is coupled much stronger than the first monopole mode.

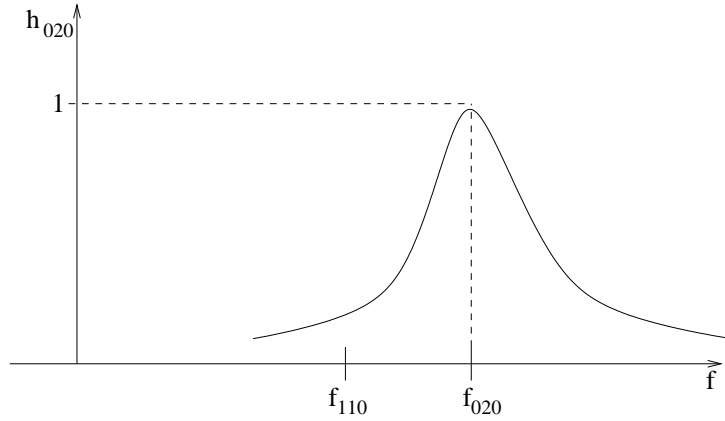


Figure 4.14: Leakage factor of the second monopole mode into the dipole mode frequency

- V_N is noise level:

$$V_N = NF \sqrt{4k_b T \cdot BW \cdot Z} \quad (4.10)$$

where $k_b = 1.38 \cdot 10^{-23}$ J/K is Boltzmann coefficient,

NF is noise factor, and for our electronics, because of the mixer $NF = 7.5$. The other electronics components are passive (see figure 4.26) and have no contribution into the noise factor NF . The parameters of the mixer are listed in the subsection 4.2.1.

The BW is defined by the band pass filter of electronics circuit and is equal to 120 MHz, see filter in subsection 4.2.1.

T is the temperature, and Z is equal to 50Ω .

For room temperature $T = 293$ K, equation 4.10 leads to the noise level of -70 dBm (0.07 mV).

The results of above computed voltages at 1.512 GHz are listed in table 4.4.

| | | |
|-----------------|---------|-----------|
| V_{110}^{out} | 6.3 mV | -31 dBm |
| V_{010}^{out} | 4.3 mV | -33.8 dBm |
| V_{020}^{out} | 13.9 mV | -24.4 dBm |
| V_N | 0.07 mV | -70 dBm |

Table 4.4: Voltages at the dipole mode frequency for a $10 \mu\text{m}$ offset

4.1.2 Estimation of the prototype absolute resolution

Resolution refers to the ability to measure smallest displacement of the bunch, as opposed to a reference position.

In the case of a $10 \mu\text{m}$ bunch offset, the coupled signal at the dipole mode frequency is in table 4.4 (see also equation 4.2). After the 180° hybrid (see figure 4.29) the values listed in table 4.4 is being changed. How strong it will be changed depends on the isolation value of the hybrid.

The test measurement of the hybrid isolation between Δ and Σ ports is realized. For this purpose S_{21} measurement by vector network analyzer is performed. The layout is in figure 4.15¹, frequency range is from 1 GHz to 2 GHz. The input is splitted by an other hybrid with the same parameters and connected to the hybrid input ports. Because of this second hybrid the difference output port is Σ , and the sum output is Δ .

At first the port Σ was measured, the port Δ was terminated by 50Ω load. The result of the measurement is in figure 4.16. Then the port Δ was measured and the port Σ was terminated by 50Ω load. The result of the measurement is in figure 4.17.

Comparing the results we get 18.5 dB isolation at the frequency 1.5 GHz. The voltages at the hybrid inputs are listed in table 4.4. The voltages at the difference output of the hybrid are listed in table 4.5.

¹For more correct measurement a phaseshifter should be included in the layout, but we hadn't any.

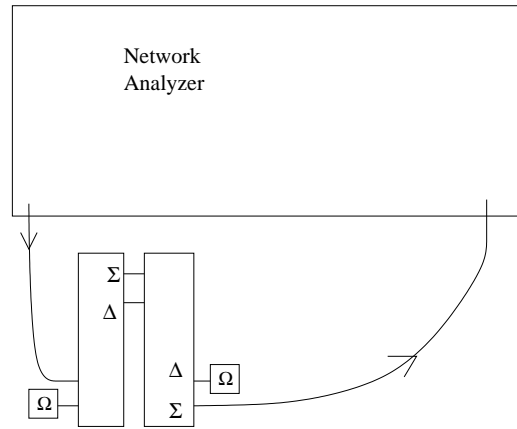
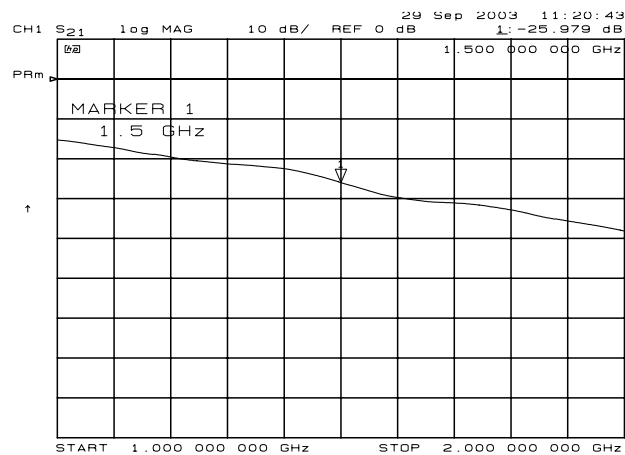


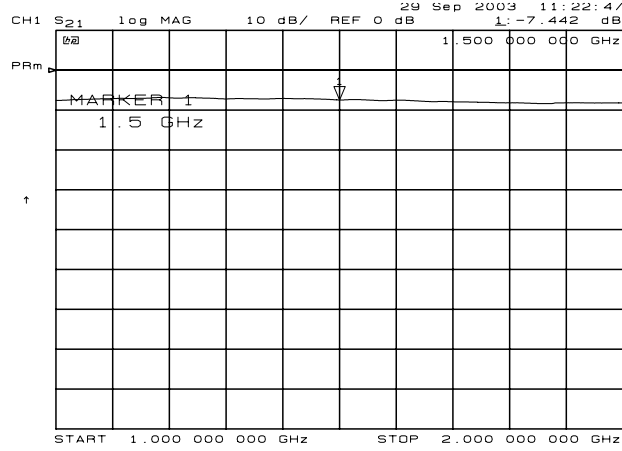
Figure 4.15: Layout of the hybrid test measurement

Figure 4.16: Result of the hybrid Σ port measurement

| | | |
|-----------------|-----------|---------|
| V_{110}^{out} | -28 dBm | 8.9 mV |
| V_{010}^{out} | -49.3 dBm | 0.7 mV |
| V_{020}^{out} | -39.9 dBm | 2.4 mV |
| V_N | -70 dBm | 0.07 mV |

Table 4.5: Voltages at dipole mode frequency 1.5 GHz after the hybrid

After the filter, see figure 4.30 we can write the coupled signal at the dipole mode frequency as

Figure 4.17: Result of the hybrid Δ port measurement

$$V(x) = a \cdot x + b + V_N \quad (4.11)$$

where $a \cdot x = V_{110}^{out}(x)$, a and b are constant values for a given bunch charge. b represents leakages of first and second monopole modes at the dipole mode frequency. The relative displacement of the bunch will be sensed if

$$a \cdot \delta x > V_N \quad (4.12)$$

For a $\delta x = 10 \mu\text{m}$ we have $a \cdot \delta x = 8.9 \text{ mV}$ and $V_N = 0.07 \text{ mV}$, hence the resolution value is 78.6 nm.

Actually the hybrid should guarantee 20 dB (not 18.5 dB) isolation between Δ and Σ ports, which leads to 1.5 dB lower value of b as it is. In this way b can be lowered further if we use a hybrid with higher isolation performance than 20 dB.

The resolution of 78.6 nm could be even further improved if the bandwidth of the bandpass filter were equal to the bandwidth of the signal. The bandwidth of the signal is

$$BW_{signal} = \frac{f_{110}}{Q_L^{110}} = 1.5 \text{ [MHz]}. \quad (4.13)$$

In this way we reduce the thermal noise 8.8 times, hence the resolution performance would be 8.9 nm.

Time-resolution

Time-resolution of the prototype is defined by the damping time τ_{110} of the dipole mode TM_{110} . More detail about damping time τ see in chapter 2, equation 2.33.

For bunch to bunch measurements τ_{110} should be smaller than the distance between the TESLA bunches t_b : $t_b = 337$ ns. Damping times of the dipole modes are listed in table 4.3 and are around 200 ns. So, a bunch to bunch measurement should be possible.

4.1.3 Frequency scan and Q_L measurement of the cavity

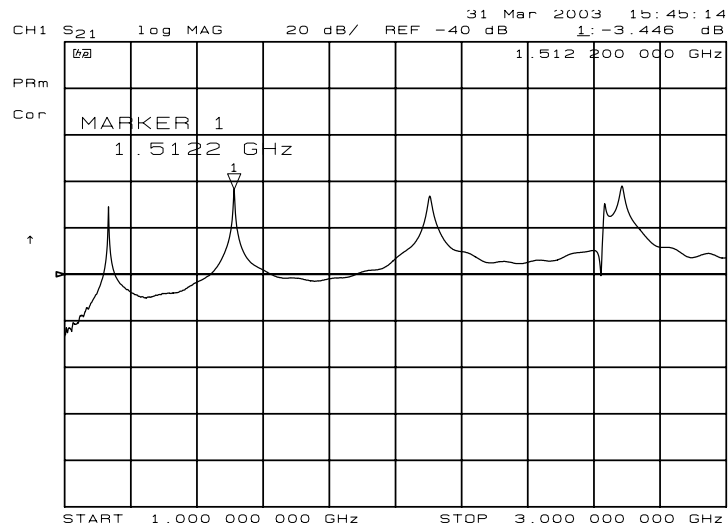


Figure 4.18: Resonating modes

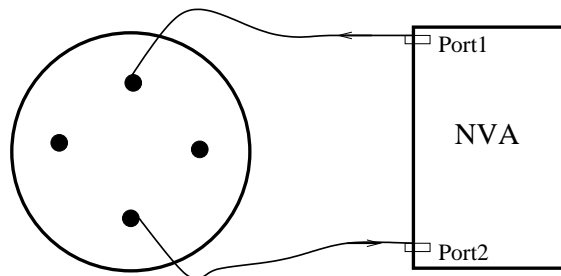


Figure 4.19: Frequency scan measurement

The Q values of a resonant cavity can be determined experimentally in many ways. These can be divided into four groups [39]:

- Transmission method
- Impedance measurement
- Transient decay or the decrement method
- Dynamic methods

The first method was applied. According to the transmission method the cavity with input and output terminals is used as a transmission device, see figure 4.19. The output signal is measured as a function of frequency, resulting in the resonance curve from whose bandwidth the Q value can be computed, see figure 4.18.

So, a S_{21} measurement by a network analyzer has been performed. The frequency range is from 1 GHz to 3 GHz. The reference line is on -40 dB and the scale is 20 dB. The marker shows the 1.5122 GHz dipole mode frequency and its -3.4 dB signal level. The first peak corresponds to the common mode.

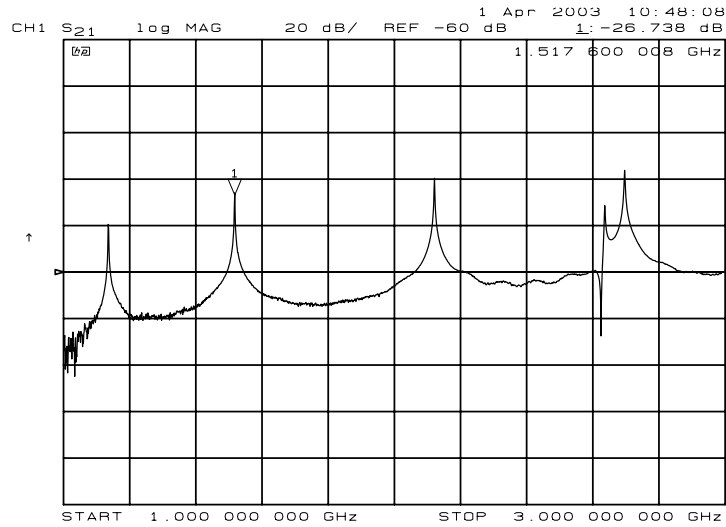
The data are summarized in table 4.6

| | measured(warm) | computed(warm) |
|-------------|----------------|----------------|
| Q_L^{110} | 717 | 700 |
| f_{110}^x | 1.512 GHz | 1.51 GHz |
| Q_L^{110} | 760 | 780 |
| f_{110}^y | 1.522 GHz | 1.522 GHz |
| Q_L^{010} | 1133 | 1136 |
| f_{010} | 1.131 GHz | 1.133 GHz |
| Q_L^{020} | - | 1200 |
| f_{020} | - | 2.63 GHz |

Table 4.6: Data of frequency scan

4.1.4 Q_0 – measurements

In finding the Q_0 the challenge of the procedure described in subsection 4.1.3 lies by reducing the coupling coefficients sufficiently. This is usually done by reducing the coupling between the detector and the cavity until it is found that further reduction in coupling no longer affects the measured resonance curve. Depending upon practical circumstances, this procedure can be either simple or complicated. In our case the coupling system is realized by pin-antennas, and the coupling coefficients can be reduced easily. But if, for example, the coupling were provided by means of an iris, such procedure is generally impractical [39].

Figure 4.20: Q_0 -measurement

This measurement is realized in the same way as in figure 4.19. But now the coupling pin-antenna is 1 mm in the cavity (before it was 7.6 mm). To measure the dipole mode parameters on y -axis the signal is generated and coupled through the pin-antennas in y -direction.

The data are summarized in table 4.7.

| | measured | computed |
|-------------|------------|-----------|
| Q_0^{110} | 1700 | 1520 |
| f_{110}^x | 1.5176 GHz | 1.514 GHz |
| Q_0^{110} | 1850 | 1600 |
| f_{110}^y | 1.527 GHz | 1.525 GHz |
| Q_0^{010} | 2000 | 1700 |
| f_{010} | 1.14 GHz | 1.14 GHz |

Table 4.7: Data of Q_0 -measurement

4.1.5 Cross-talk measurement

Cross-talk isolation measurements were performed as indicated in figure 4.21. At first, we generated and coupled the signal through the pin-antennas in the same direction as in figure 4.21a. The two remaining coupling ports were loaded by 50Ω . Left plot in figure 4.22 shows the result of this measurement. Here signal level is obtained as a function of frequency. Frequency axis starts

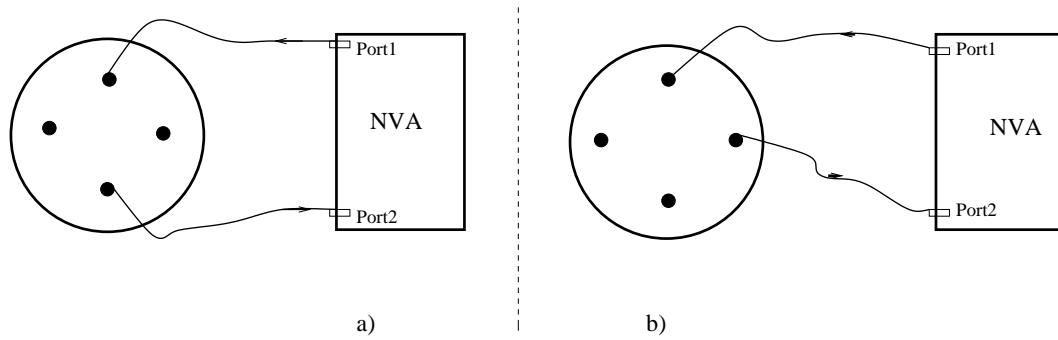


Figure 4.21: Schematic illustration of the cross-talk measurement

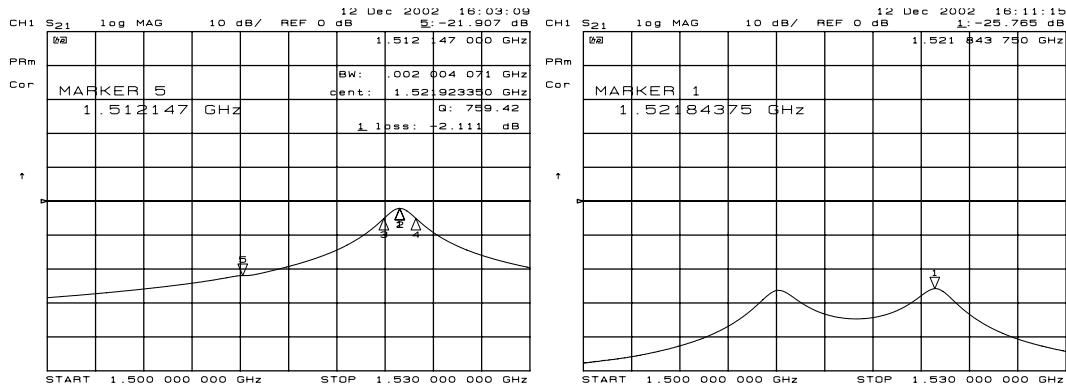


Figure 4.22: Signal level in [dB] against frequency. The signal level is graded by 10 dB. The reference 0 dB-line is the middle one of the plots

by 1.5 GHz and is stopped by 1.53 GHz. A maximum at 1.522 GHz with a level of -1.8 dB is observed.

Next we repeated the measurement using pin-antennas in perpendicular x ; y directions (Figure 4.21b) and obtained the second plot in figure 4.22. Here two maxima are visible. The corresponding signal at the second maximum with the same frequency has a level of -25.8 dB. The first maximum on 1.512 GHz refers to the second dipole mode in perpendicular plane.

The cross-talk isolation value is 24 dB, difference between left and right plots in figure 4.22, at the same 1.522 GHz frequency. The cross-talk measured by the other ports was about the same (0.5 dB maximal difference).

4.1.6 Power dissipation caused by the resonating modes of the BPM

In chapter 1 we have not discussed the power dissipation (≈ 27.9 mW) caused by the resonating modes of the cavity, as it is negligible compared to the values listed in table 1.4. In this subsection we illustrate the computation of above mentioned 27.9 mW power dissipation.

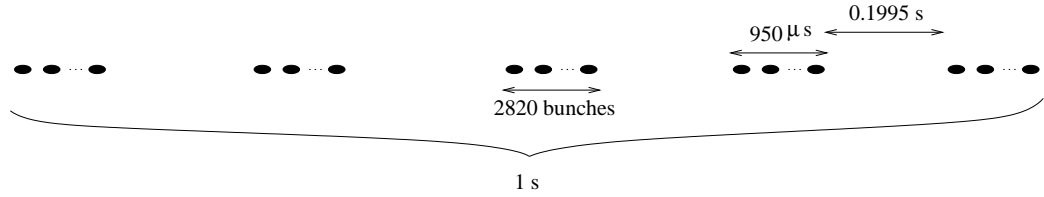


Figure 4.23: Relations between bunches, beams and repetition frequency, see table 1

When a TESLA bunch flies through the BPM it excites resonating modes in the cavity. If the whole stored energy W in the resonating modes of the cavity excited by the TESLA bunch dissipates on the walls then the dissipated power for the TESLA beam with repetition rate of 5 Hz (see figure 4.23) is

$$P = W[J] \cdot 2820 \cdot 5[s^{-1}] = 27.9 \text{ [mWatt]}, \quad (4.14)$$

The number 2820 in equation 4.14 represents the number of bunches in the beam. To calculate W we have supposed that the bunch flies through the cavity with 1mm offset. W was given as

$$W = W_{010} + W_{020} + W_{110}^x + W_{110}^y \quad (4.15)$$

where W_{010} is the stored energy in the first monopole mode, W_{020} - in the second monopole mode, W_{110}^x - in the dipole mode with x polarisation, W_{110}^y - in the dipole mode with y polarisation.

- W_{010} in the mode TM_{010}

Stored energies are computed according to the equation

$$W = \frac{\omega}{4} \frac{R_{sh}}{Q} \cdot q^2 \quad (4.16)$$

and W_{010} is equal to

$$W_{010} = \frac{\omega_{010}}{4} \frac{R_{sh}^{010}}{Q} \cdot q^2 = 513.14 \cdot 10^{-9} \text{ [J]}, \quad (4.17)$$

where $\frac{R_{sh}^{010}}{Q} = 28\Omega$ is the shunt impedance over Q of the mode TM_{010} (for its definition see section 2.2 , equation 2.39), $q = 3.2$ nC is the bunch charge and $\omega_{010} = 2\pi \cdot f_{010}$, where f_{010} is the frequency of the mode. Shunt impedance over Q of these modes and their frequencies are listed in table 4.3.

- W_{020} in the mode TM_{020}

Stored energy W_{020} is computed analog to W_{010} and is equal

$$W_{020} = \frac{\omega_{020}}{4} \frac{R_{sh}^{020}}{Q} \cdot q^2 = 1464.3 \cdot 10^{-9} \text{ [J]}. \quad (4.18)$$

For $\frac{R_{sh}^{020}}{Q}$ and ω_{020} see again table 4.3.

- We can suppose $W_{110}^x \approx W_{110}^y$ and the stored energy W_{110}^x in the dipole mode TM_{110}^x is equal

$$W_{110}^x = \frac{\omega_{110}}{4} \frac{R_{sh}^{110}}{Q} \cdot q^2 = 1.15 \cdot 10^{-9} \text{ [J]}. \quad (4.19)$$

4.1.7 Test of leakage factor

The equations 4.5, 4.6 are correct around the resonance frequency of a given mode, here f_{010} . In this subsection we show how big the error is when according equation 4.5 we look at the leakage of the mode TM_{010} at frequency far from its bandwidth. The center frequency of the mode TM_{010} is $f_{010} = 1.13$ GHz. The bandwidth of this mode is

$$BW_{010} = \frac{f_{010}}{Q_L^{010}} = \frac{1.13[\text{GHz}]}{1133} \approx 1 \text{ MHz} \quad (4.20)$$

Let us look for a leakage of the mode TM_{010} at frequency

$$f_{010} - 40 \cdot BW_{010} = 1.09 \text{ GHz} \quad (4.21)$$

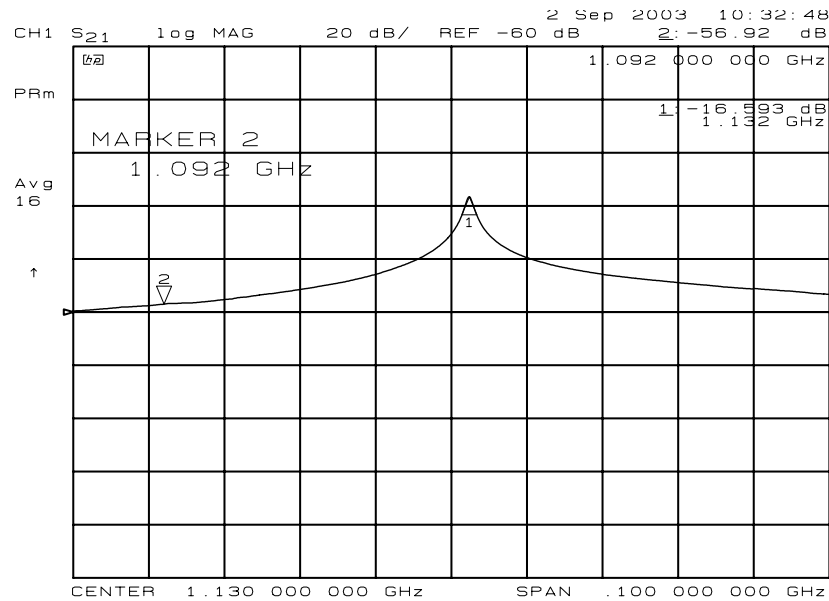
(marker two in figure 4.24).

According equations 4.5, 4.6 the leakage of the mode TM_{010} to the frequency 1.09 GHz is

$$h(1.146\text{GHz}) = \frac{1}{\sqrt{1 + \alpha^2(1.09 \text{ GHz})}} \approx \frac{1}{80} \quad (4.22)$$

where $\alpha(f)$ is

$$\alpha(f) = 2Q_L^{010} \frac{1.09 - f_{010}}{f_{010}} = 2 \cdot 1133 \frac{0.04}{1.13} \approx 80. \quad (4.23)$$

Figure 4.24: Q_0 -measurement

Equation 4.22 means that the signal level at 1.09 GHz should be 80 times lower than at 1.13 GHz.

The results of the measurement in figure 4.24 show the following ratio between signal levels at frequencies 1.13 GHz and 1.09 GHz:

$$\frac{V(1.13)}{V(1.146)} \approx 10^{40/20} = 100 \quad (4.24)$$

Comparing the value 80 from the equation 4.22 with the value 100 from the equation 4.24 we get 20 % error in our computations. In other words the leakage of the monopole modes is expected to be 20 % smaller than it was computed.

4.2 Electronics

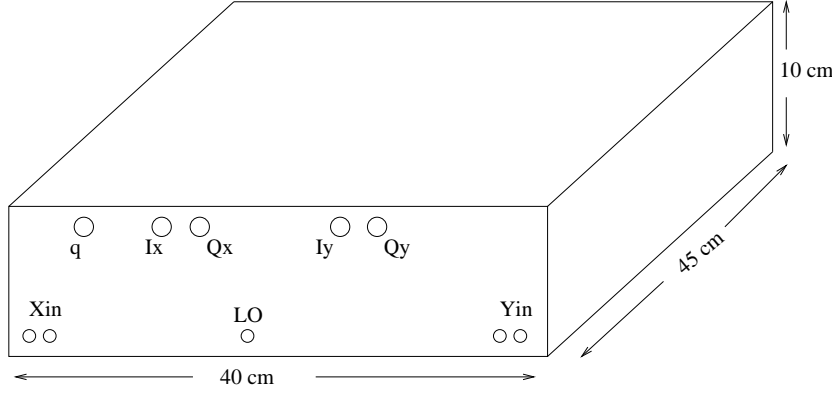


Figure 4.25: Electronics box

At the beginning let us list values of the signals, which should be handled by the electronics:

| | | |
|-------------------------------------|------------------|-------------------|
| bunch distance | 337ns (2.96 MHz) | |
| TM_{110} | 1.515 GHz | |
| TM_{010} | 1.14 GHz | |
| TM_{020} | 2.64 GHz | |
| Bunch charge | 3.2 nC | 0.1 nC |
| $V_{110}^{out}(\delta x = 10\mu m)$ | -31 dBm | -61 dBm (0.19 mV) |
| $V_{010}^{out}(10\mu m)$ | -33.8 dBm | |
| $V_{020}^{out}(10\mu m)$ | -24.4 dBm | |
| $V_{110}^{out}(\delta x = 2.5mm)$ | 17 dBm (1.57 V) | |

Table 4.8: Signals from the pick-up station

Comparing parameters such as *dynamic range*, *signal to noise ratio*, *amount of electrical components* (less components means cheaper electronics system) we have chosen a *homodyne* system for signal detection [41]. In figure 4.26 we show the whole electronics circuit.

The electronics in figure 4.26 at 1.5 GHz is a homodyne receiver, normalized to bunch charge. Its LO signal at 1.5 GHz frequency is taken from the reference cavity.

The principle of I/Q down-conversion method is that the signal is at first divided into two channels and then down-converted by LO signal, which has

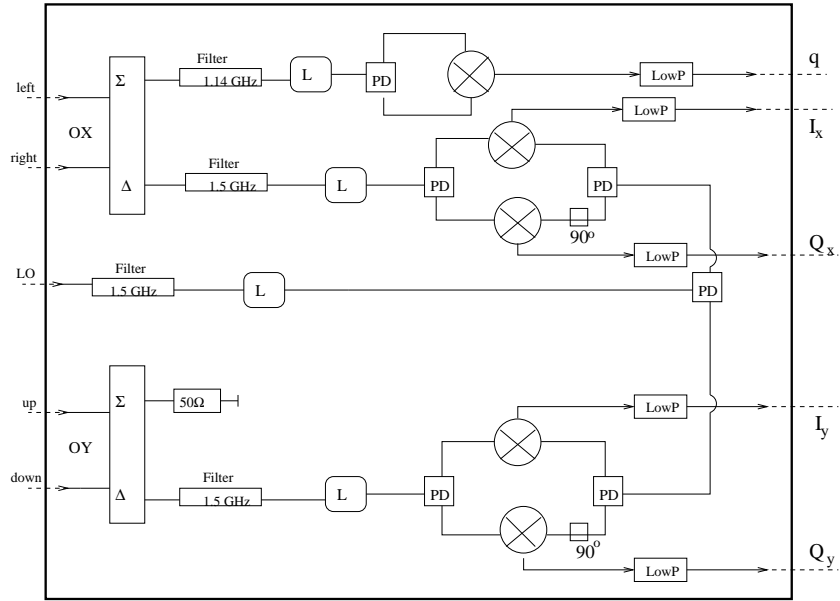


Figure 4.26: The whole electronics circuit for new pill-box BPM; bunch charge and position measurement



Figure 4.27: Photo of the open electronics box

a 90° phase difference in one channel with respect to the other [42], see figure 4.26. The resulting signal is

$$|Signal| = \sqrt{I^2 + Q^2}, \quad \varphi = \arctan \frac{Q}{I} \quad (4.25)$$

One should also take care separately of the signs of Q and I , otherwise we lose half of the information. With the help of I/Q down-conversion there is no need to use a phase-shifter to bring RF and LO signals in phase.

The electronics box has 5 output channels: two for x -position detection; two for y -position detection, and one for charge detection (see also figure 4.27).

4.2.1 Electronics Components

All components are once more tested.

Mixer: DM0052LA2 (PARTZICH)

| | |
|------------------------|-----------------------|
| RF/LO -frequency range | 0.5 - 2 GHz |
| IF -frequency range | DC - 0.5 GHz |
| Nominal LO power | 7 -13 dBm |
| RF/LO isolation | 40/30 dB(typ./min.) |
| RF/IF isolation | 30 dB |
| 1dB comp. point | 3 dBm |
| Conversion loss | 6.5/8.5 dB(nom./max.) |

After the test of 8 mixers (see, figure 4.28), mixers with most equal performances are sorted in pairs. One pair is used for realizing I_x/ Q_x down-conversion (figure 4.26). Another pair is used for realizing y detection.

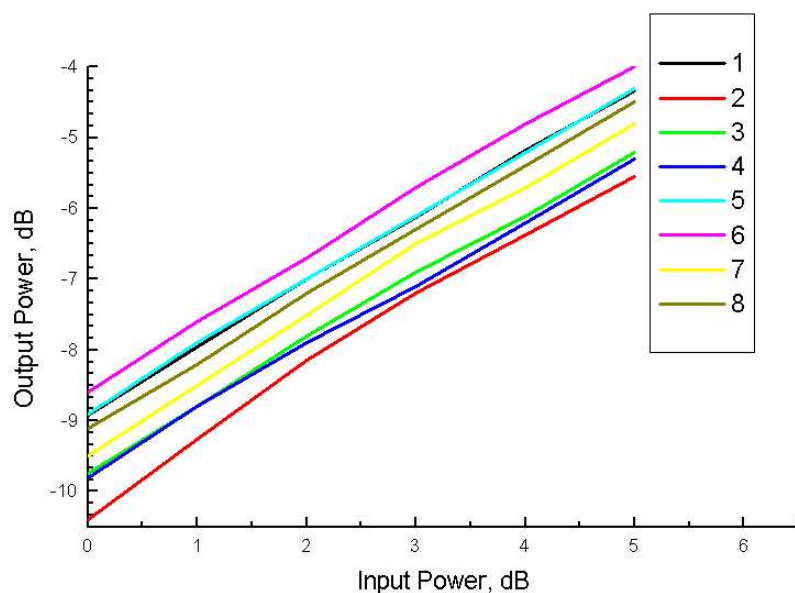


Figure 4.28: Test plot of 8 mixers

Mixer number 2 (red line at the bottom of the figure 4.28) has most different performance. This one is applied in q-channel.

Hybrid: M/A-COM, 2031-6331-00

Frequency range 1 - 2 GHz
 Phase unbalance 4°
 Isolation 20 dB

For each coordinate detection there is a hybrid in the electronics circuit, figure 4.26. With the help of the hybrid we reduce the contribution of monopole modes at the frequency of the dipole mode TM_{110} , which carries information about bunch displacement.

Let us discuss the hybrid for x coordinate detection. The signal coming on each input² of the hybrid in figure 4.29 is given by equation 4.2. The power values of the dipole mode, first monopole mode and second monopole mode corresponding to beam offset of $10 \mu\text{m}$ are in table 4.8.

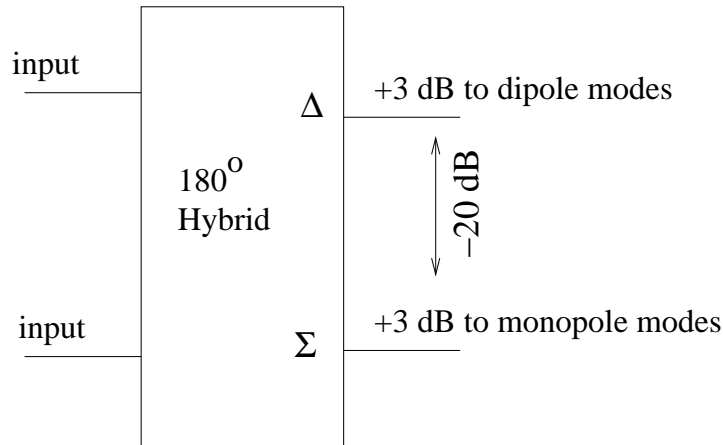


Figure 4.29: 180° hybrid

In table 4.9 we list these values together with the corresponding ones on the hybrid Δ and Σ outputs.

The output Δ is responsible for position detection. We see in the table 4.9 that before the hybrid the highest contribution at the dipole mode frequency is from the second monopole mode and after the hybrid it is from the dipole mode itself.

²Of course there is also power damping in the cables connecting the cavity with the hybrid.

| Power | hybrid inputs | hybrid Δ output | hybrid Σ output |
|-----------|---------------|------------------------|------------------------|
| P_{110} | -31 dBm | -28 dBm | -48 dBm |
| P_{010} | -33.8 dBm | -50.8 | -30.8 dBm |
| P_{020} | -24.4 dBm | -41.4 dBm | 21.4 dBm |

Table 4.9: Power values on the hybrid inputs and outputs at f_{110} **RF Band-select filter:** RLC, BPF-500-1517-120-5-RM

| | |
|----------------|-------------------|
| Insertion loss | -0.8 dB |
| Passband | 1516 ± 62 MHz |
| Attenuation at | |
| $f = 1.14$ GHz | -82 dB |
| $f = 1.3$ GHz | -62 dB |
| $f = 2.64$ GHz | -90 dB |
| VSWR | 1.2 |

The performance of the filter is shown in figure 4.30

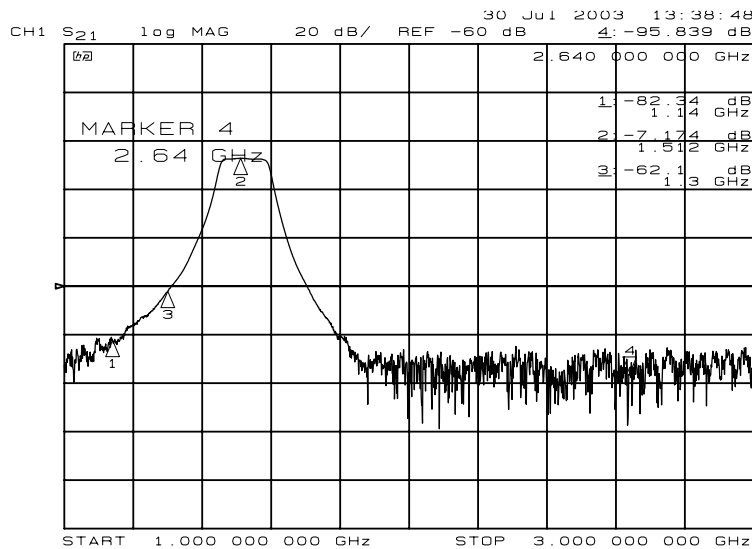


Figure 4.30: Test measurement of the bandpass filter

Limiter: ACC, ACLM-4530

| | |
|----------------------------|-------------|
| Frequency range | 0.5 - 2 GHz |
| Insertion loss | 0.4 dB |
| VSWR max. | 1.5 |
| Max. input power(peak/cw) | 100W/2W |
| Max. flat leakage(peak/cw) | 20dBm/18dBm |

There is a limiter on each detecting channel. It is put only because of safety.

Lowpass Filter: TU-Berlin, EN2

Pass frequency DC - 10 MHz

Gain 1 dB

This lowpass filter is built at TU Berlin [43].

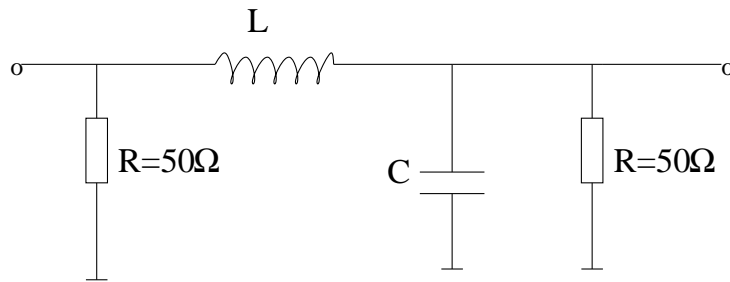


Figure 4.31: Components of the lowpass filter

The lowpass filter is constructed by the help of a resonant circuit R, L, C (see figure 4.31) with $f_0 = 4$ MHz central frequency and $BW = 13$ MHz bandwidth, figure 4.32.

Such a resonant circuit has a Q-value of $Q=f_0/BW = 0.3$, which is defined also as

$$Q = \frac{L \cdot \omega_0}{R} \quad (4.26)$$

and L is

$$L = \frac{Q \cdot R}{\omega_0} = 0.597 \mu\text{H}. \quad (4.27)$$

C is found by resonant condition

$$\omega_0 = \frac{1}{\sqrt{L \cdot C}}, \quad (4.28)$$

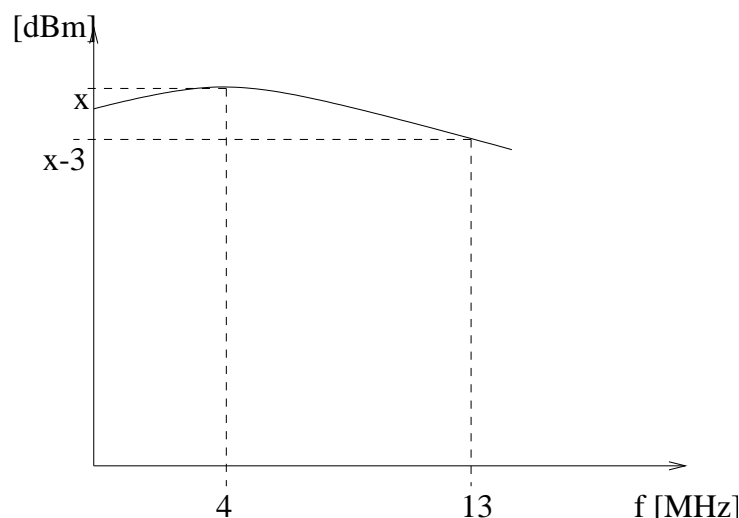


Figure 4.32: Central frequency and band width of the resonating circuit R, L, C

and is equal $C = 2.65$ nF.

The performance of this lowpass filter was good, and it was put into the electronics.

Power Divider: MCLI, PS2-2

| | |
|--------------------------|---------------|
| Frequency range | 1 - 2 GHz |
| Isolation | 20 dB |
| Insertion loss | 0.35 dB |
| VSWR, dB Max. | 1.25:1/1.15:1 |
| Ampl.balance \pm Max. | 0.2 dB |
| Phase balance \pm Max. | 2° |

4.2.2 Electronics test measurements

Each channel is tested separately. For the measurements two signal generators and an oscilloscope were used. The test setup of the measurement is seen in figure 4.33.

A signal diagram of I_x -channel measurement is in figure 4.34. The same type of measurements were performed for different input signals to the mixer LO port: $P_{LO} = 9$ dBm; $P_{LO} = 5.8$ dBm; $P_{LO} = 2.7$ dBm; $P_{LO} = 0.5$ dBm. The best performance of the mixer was observed in case of $P_{LO} = 5.8$ dBm,

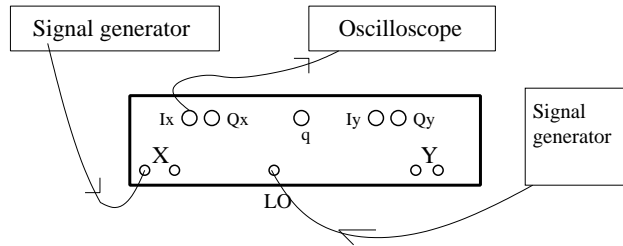


Figure 4.33: Layout of electronics test measurement

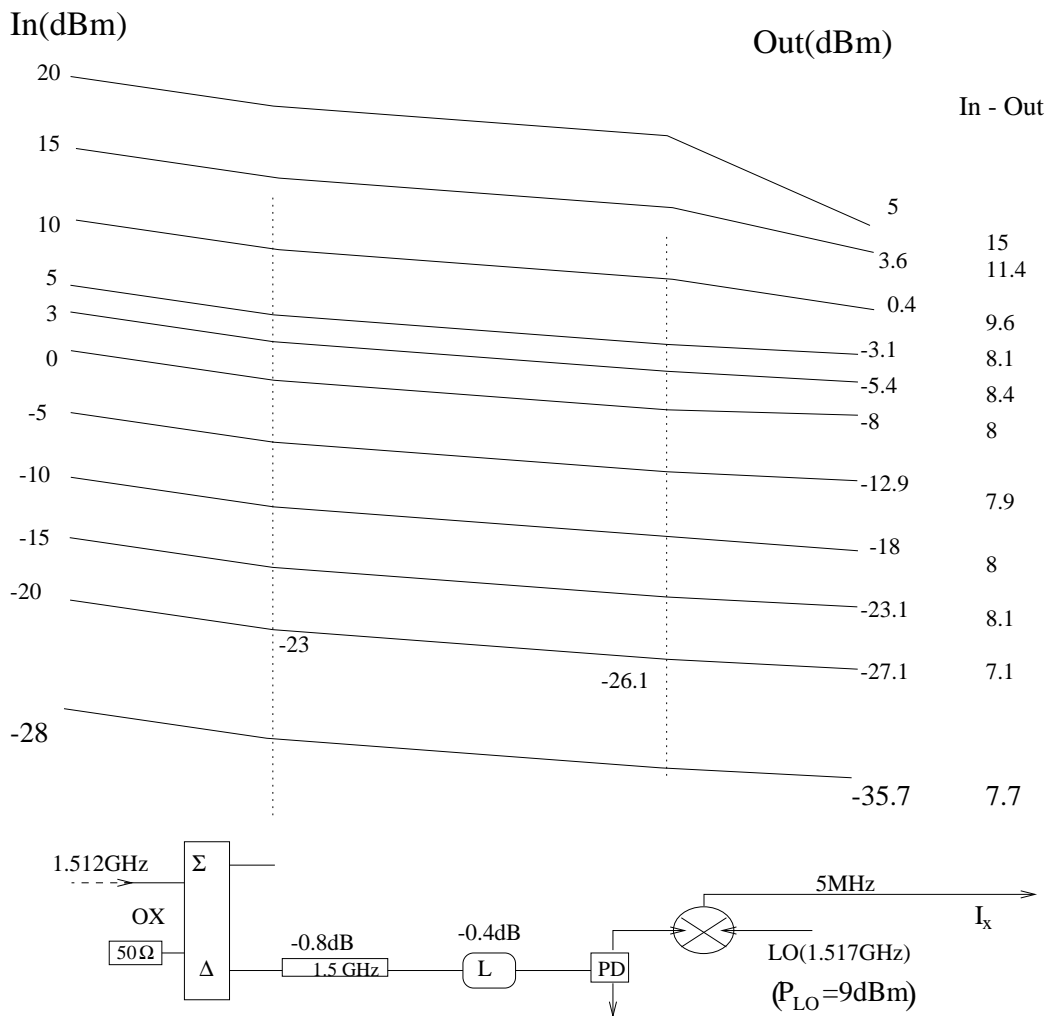


Figure 4.34: Signal diagram of I_x -channel

| | Q_x | I_y | Q_y |
|----------------|---------------|---------------|---------------|
| P_{In} [dBm] | In - Out [dB] | In - Out [dB] | In - Out [dB] |
| 20 | 14.9 | 19.7 | 19.7 |
| 15 | 11.4 | 15 | 15 |
| 10 | 8.7 | 14 | 14 |
| 5 | 7.8 | 13.4 | 13.8 |
| 3 | 7.9 | 13.4 | 13.9 |
| 0 | 7.9 | 13.3 | 13.9 |
| -5 | 7.9 | 13.4 | 13.9 |
| -10 | 8 | 13.6 | 14 |
| -15 | 8.1 | 13.4 | 12.7 |
| -20 | 7.7 | 13.1 | 13.1 |
| -28 | 7.7 | 13.2 | 13.2 |
| -40 | 8.9 | 14.2 | 14.1 |
| -45 | 10 | 14.9 | 15 |

Table 4.10: Results of the electronics channel test measurements

see mixer parameters in subsection 4.2.1.

The results of the other channel measurements are summarized in the table 4.10. We see here that for an RF signal smaller than 10 dBm the electronics shows linear character. The noise level was calculated as

$$V_N = NF \sqrt{4k_b T \cdot BW \cdot Z}, \quad (4.29)$$

and is equal to -70 dBm (see table 4.5). But during the electronics test for input signals smaller than -48 dBm the amplitude of the output signal was not stable any more. -48 dBm (0.89 mV) signal corresponds to the TESLA bunch 1 μm offset.

4.3 Laboratory test of the BPM

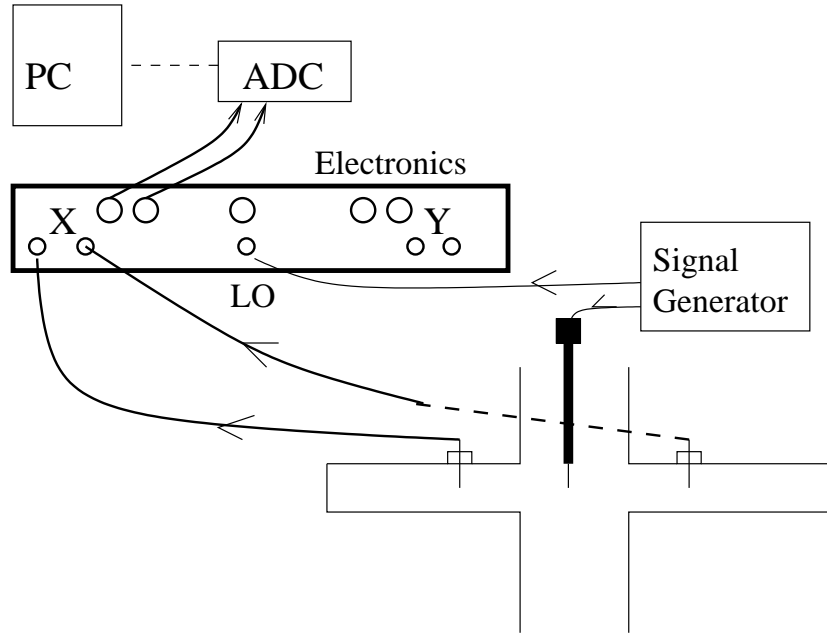


Figure 4.35: Layout of the complete BPM test measurement

The test-measurement was performed at DESY-Zeuthen. The dipole mode of the prototype was generated by a generator through the antenna, see figure 4.35. For the control of test setup the computer code LabVIEW was used. The generator-antenna was moved in steps of $10 \mu\text{m}$ in x -direction (y -direction) in a range of $\pm 1\text{mm}$. Then the signal was coupled through the coupling antennas in x -direction. The other antennas in y -direction were terminated by 50Ω loads.

The generator antenna is a coaxial cable with diameter of 3.7 mm , pin-diameter 0.96 mm . At the end the pin is free with the length $\lambda/10$. λ corresponds to 1.5 GHz frequency.

With the detected I_x, Q_x values (see also figure 4.26) V_x is computed

$$V_x = \sqrt{I_x^2 + Q_x^2}, \quad (4.30)$$

and shown in figure 4.36.

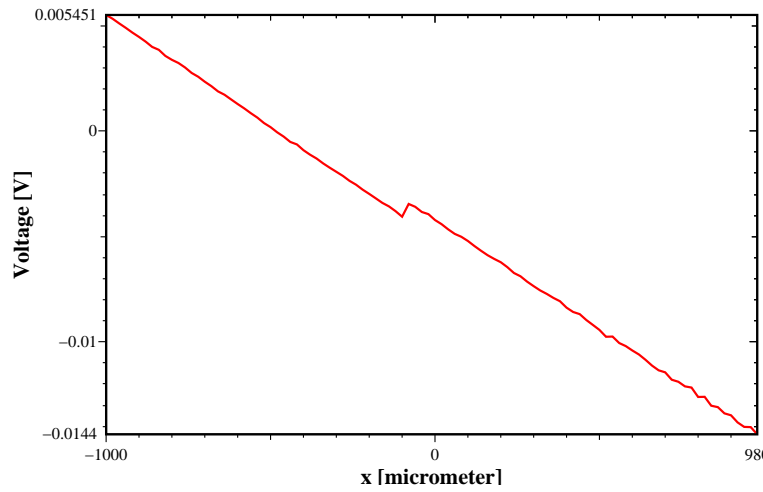


Figure 4.36: Resolution test-measurement with the electronics

In figure 4.37 is the average of the curve in figure 4.36. It is called also sensitivity curve. How sensitive the BPM is depends on the angle of the curve. The bigger the slope, the better the sensitivity is, which leads to better resolution. The equation of curve in figure 4.37 is

$$V(x) = K \cdot x + B. \quad (4.31)$$

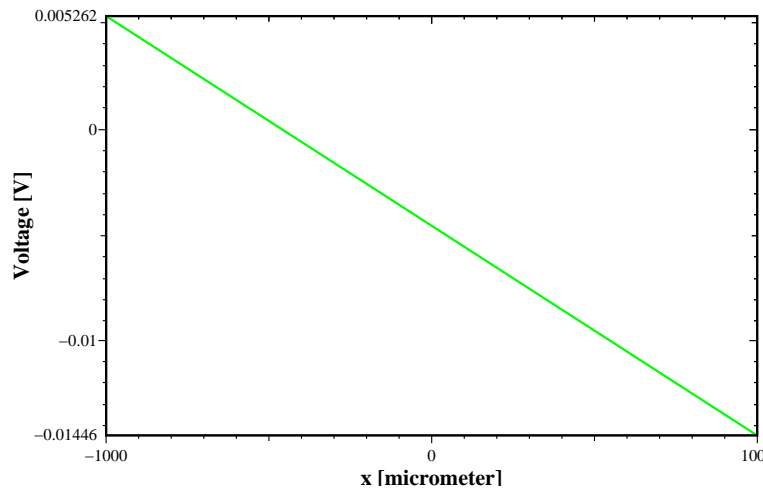


Figure 4.37: The BPM sensitivity

If we have n measured points, then K and B can be given as [40]

$$K = \frac{[x][y] - n[xy]}{[x][x] - n[xx]}, \quad B = \frac{[x][xy] - [y][xx]}{[x][x] - n[xx]} \quad (4.32)$$

where

$$[x] = \sum_{i=1}^n x_i, \quad [y] = \sum_{i=1}^n y_i, \quad [xx] = \sum_{i=1}^n (x_i x_i), \quad [xy] = \sum_{i=1}^n (x_i y_i) \quad (4.33)$$

In our case $K = -0.79576 \cdot 10^{-5}$ and $B = 0.0046$.

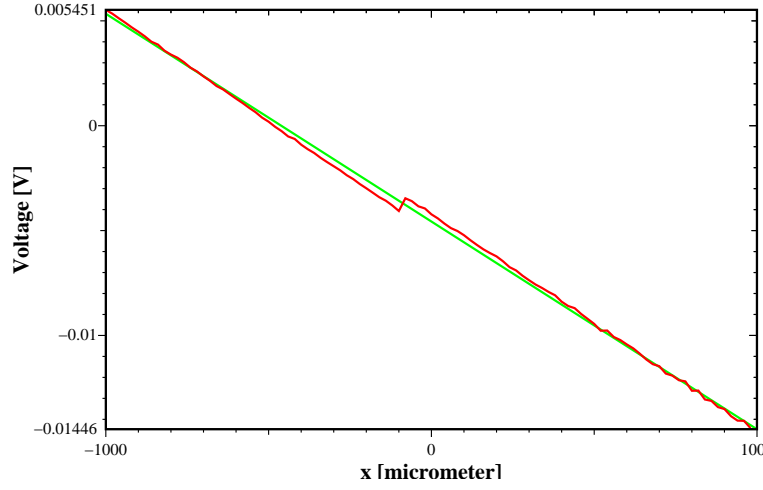


Figure 4.38: Resolution plot of the BPM

In figure 4.38 we put figures 4.36 and 4.37 together. The mismatches of the average curve and the measured points lead to a resolution value of

$$\langle \Delta x \rangle = 41.8 \mu\text{m}, \quad (4.34)$$

defined as

$$\langle \Delta x \rangle = \sqrt{\langle \Delta x^2 \rangle}, \quad \langle \Delta x^2 \rangle = \frac{\sum_{i=1}^n (V_i^{aver.} - V_i^{meas.})^2}{K^2} / n \quad (4.35)$$

Here, $V_i^{meas.}$ is the measurement at point x_i , and $V_i^{aver.}$ is the corresponding one on the average curve.

In real conditions a change of the bunch position by $10 \mu\text{m}$ corresponds to a voltage change $\delta V_{real} = 8.9 \text{ mV}$ (see table 4.5). Taking the curve in

figure 4.37 a change of x by $10 \mu\text{m}$ leads to $\delta V_{test} = 0.079 \text{ mV}$. And when we compare δV_{real} and δV_{test} we get

$$\frac{\delta V_{real}}{V_{test}} \approx 112.6 \quad (4.36)$$

Hence, when we extrapolate the test value of the resolution $\langle \Delta x \rangle = 41.8 \mu\text{m}$ to the real conditions we expect a 112.6 times better resolution equal to 371 nm .

4.3.1 Alternative electronics

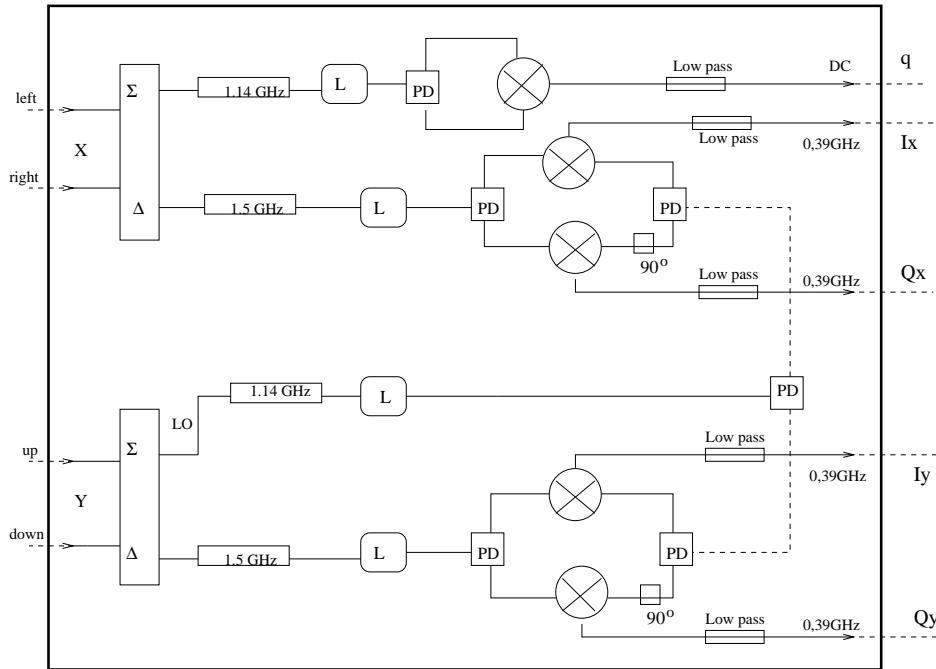


Figure 4.39: Alternative electronics box

We offer an alternative solution for the electronics, shown in figure 4.26. Here as a reference signal we use the Σ -port of the hybrid for y -detection, see figure 4.39.

This is possible, since the signal on fundamental mode frequency is constant near the pipe-axis, see figure 4.10. That is why it is useful to use this electronics construction. The IF signal will be at 0.4 GHz frequency. This can be digitized either directly by an expensive ADC or with the help of a

logarithmic detector. In the last case we would detect a decaying signal, see figure 4.40.

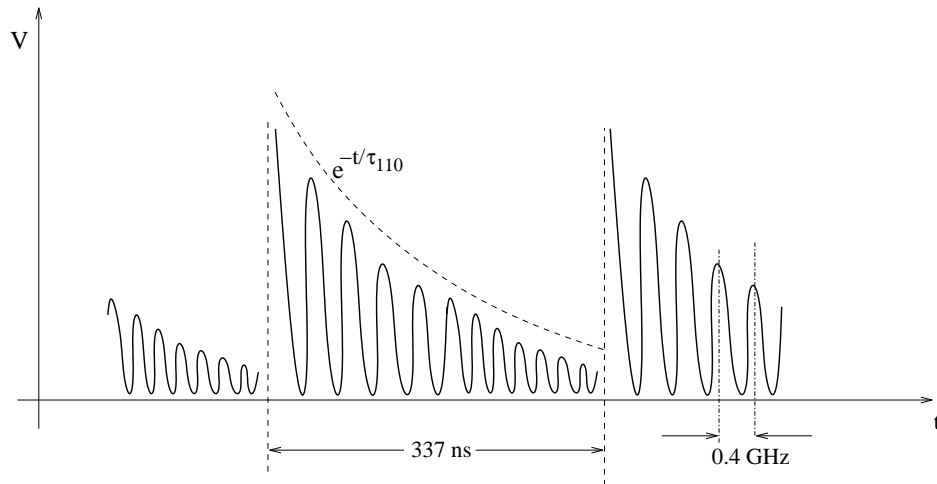


Figure 4.40: The signal after the down-conversion

Depending on the success of the electronics one can economize an extra cavity for the reference signal.

Summary

The future 33 km long e^+e^- linear collider TESLA has a fundamental importance for particle physics, condensed matter physics, chemistry, material science and biology. TESLA needs a lot of Beam-Position-Monitors (BPMs) to keep the position of the beam under control. A big amount of these BPMs (1752 BPMs) should be situated at 2 K cryogenic environment.

These BPMs should fulfill the following demands:

- The first demand follows from the big number of such BPMs (1752). **The design and fabrication of the BPM should be possibly simple.**
- The second demand follows from the 2 K cryogenic environment. It is expensive, to keep such an environment and any additional energy dissipations there are not desired. Energy dissipation of 2.5 Watt per cryomodule was computed in DESY-Hamburg, where 1.1 Watt is due to the BPM. So, the next demand is, that **there should be considerably less than 1.1 Watt energy dissipation on the BPM per cryomodule.**
- The third demand is the resolution: **The position-resolution of the BPM should not be worse than 10 μm .**
- There is always some cross-talk in BPMs, which couples the horizontal and vertical signals. And the next demand is that: **the cross-talk should be small and stable.**

Two different types of BPMs were discussed. As a prototype we chose a pill-box cavity. The inside of the prototype is copper-plated, which reduces the energy dissipations from 1.1 W to 0.46 W. We also took care, that the resonating modes of the cavity were damped fast enough, in order to realize bunch to bunch measurements.

According to theoretical computations the absolute resolution of the BPM is 78.6 nm. The interpretation of laboratory measurements showed the resolution of 371 nm.

The design of the cavity is not complicated. Radial symmetry of the cavity makes its fabrication easier and more precise. The cross-talk is minimized and stabilized by introducing two stamp-eroded rectangular recesses into the cavity.

During the work a new idea for the electronics is born. The electronics is built but not tested yet. In case of success there would be no need to build an extra cavity for the reference signal.

In the winter of 2003/2004 we are going to test the prototype once more under real conditions on ELBE linear accelerator in Rossendorf.

Acknowledgments

First of all, I wish to express my gratitude to my supervisor Prof. Dr. H. Henke and co-supervisor Dr. H. J. Schreiber for this theme, support, and discussions.

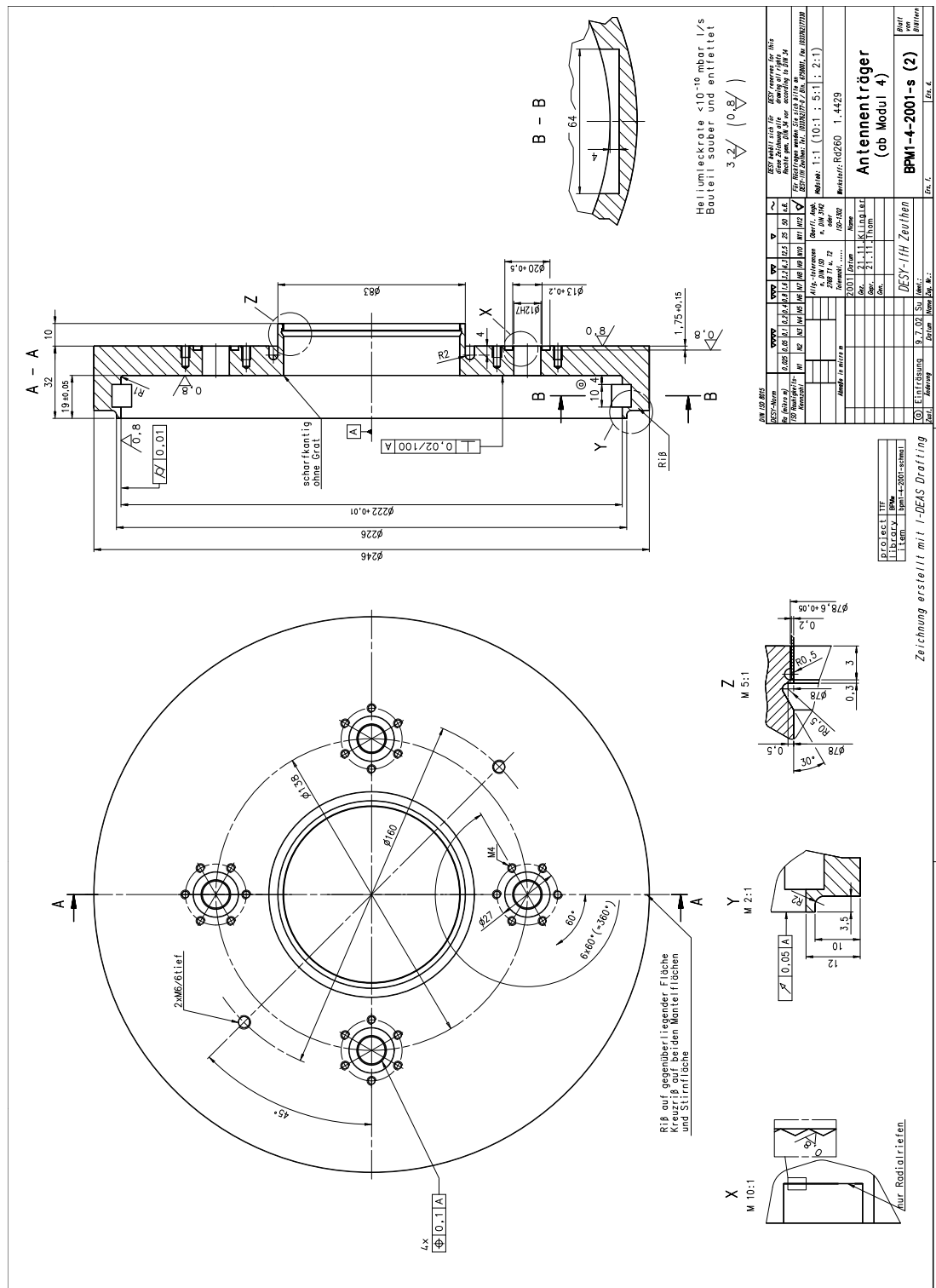
I am much in debt to my colleagues of the department Theoretical Elektrotechnik, TU-Berlin and DESY-Zeuthen, TESLA project for my participations at workshops and conferences.

I would like to say thank you to A. Liapine and Dr. M. Filtz for their constructive discussions; Dr. W. Bruns for his clear explanation of GdfidL.

Also I would like to mention J. Krueger, the co-ordinator of DESY-Zeuthen workstation, and Dr. F. Tonisch for their professionalism and careful attitude; A. Blednykh, who was in the same office with me and I have shared a lot of questions with him.

A specific appreciation to my friends and my family.

Appendix A: Technical design of the cavity; part I



Appendix D: The prototype cavity simulating GdfidL code

```
define(RR, 105e-3)
define(INF, 10000)
define(R0, 111e-3)
define(L, 18e-3)
define(a, 38.88e-3)
define(Copper, 4)
    define(ALength, 9e-3)
    define(ADiameter, 1.8e-3)
    define(AOuterDiameter, 4.32e-3)
    define(APosition, 68e-3)

-general
    scratchbase= /scr/sava1231
    outfile= /homeall/s/sava1231/resultfile

-mesh
    spacing= eval(R0/113/2)
    graded= yes, dmaxgraded= eval(R0/113)

    zfixed(2, -L/2, L/2)
    zfixed(2, -3e-3, 3e-3)
    xfixed(2, -R0 -3e-3, R0 +3e-3)

    yfixed(2, -AOuterDiameter/2, -ADiameter/2)
    yfixed(2, -ADiameter/2, 0)
    xfixed(2, -APosition - AOuterDiameter/2, -APosition - ADiameter/2)
    xfixed(2, -APosition + ADiameter/2, -APosition + AOuterDiameter/2)

    xfixed(2, -AOuterDiameter/2, -ADiameter/2 )
    xfixed(2, -ADiameter/2, 0 )
    yfixed(2, -APosition -AOuterDiameter/2, -APosition -ADiameter/2 )
    yfixed(2, -APosition +ADiameter/2 , -APosition +AOuterDiameter/2 )

    pxlow= -R0 -2e-3, pxhigh= 0
    pylow= -R0, pyhigh= 0
    pzlow= -4.5*L, pzhigh= 0 (or 4.5*L)

    cxlow= ele, cxhigh= mag
    cylow= ele, cyhigh= mag (or elec)
    czlow= elec, czhigh= elec

-material
    material= 4 (copper at 4K)
    type= electric
```

```
kappa=24.84e6
-material
  material= 3 (steel at 4K)
  type= electric
  kappa= 1.88e6
-brick (fill the 'universe' with metal)
  material = 3
  xlow = -INF, xhigh = INF
  ylow = -INF, yhigh = INF
  zlow = -INF, zhigh = INF
  doit
-gccylinder (Copper plateing)
  material = 4
  radius = RR
  length = INF
  origin = (0, 0, -INF/2)
  direction = (0, 0, 1)
  doit
-gccylinder (carve out the main cavity)
  material= 0
  radius= R0
  length= L
  origin= (0, 0, -L/2)
  direction= (0, 0, 1)
  doit
-gccylinder (eliptical teil)
  material = 0
  radius= a
  length= 6e-3
  origin= (-R0 + a -2e-3, 0, -3e-3)
  direction= (0, 0, 1)
  doit
-gccylinder
  material = 0
  radius= a
  length= 6e-3
  origin= (R0 - a +3e-3, 0, -3e-3)
  direction= (0, 0, 1)
```

```
doit
-gccylinder (carve out the beam-pipe)
  material= 0
  radius= a
  length= 8*L
  origin= (0, 0, 4*L)
  direction= (0, 0, -1)
doit

-gccylinder (Carve out the 1-st antenna)
  material= 0
  radius= AOuterDiameter/2
  length= INF
  origin= ( -APosition, 0, 0 )
  direction= ( 0, 0, -1)
doit

-gccylinder
  material=3
  radius= ADiameter/2
  length= INF
  origin= ( -APosition, 0, -L/2+ALength )
  direction= ( 0, 0, -1)
doit

-gccylinder (Carve out the 2-nd antenna)
  material= 0
  radius= AOuterDiameter/2
  length= INF
  origin= ( APosition, 0, 0 )
  direction= ( 0, 0, -1)
doit

-gccylinder
  material=3
  radius= ADiameter/2
  length= INF
  origin= ( APosition, 0, -L/2+ALength )
  direction= ( 0, 0, -1)
doit

-gccylinder (Carve out the 3-rd antenna)
  material= 0
```

```
radius= AOuterDiameter/2
length= INF
origin= ( 0, -APosition, 0)
direction= ( 0, 0, -1)
doit

-gccylinder
material=3
radius= ADiameter/2
length= INF
origin= ( 0, -APosition, -L/2+ALength )
direction= ( 0, 0, -1)
doit

-gccylinder (Carve out the 4-th antenna)
material= 0
radius= AOuterDiameter/2
length= INF
origin= ( 0, APosition, 0)
direction= ( 0, 0, -1)
doit

-gccylinder
material=3
radius= ADiameter/2
length= INF
origin= ( 0, APosition, -L/2+ALength )
direction= ( 0, 0, -1)
doit

-volumeplot
doit

-eigenvalues
estimation= 4e9
solutions= 23
doit
```

Bibliography

- [1] K. WILLE, *Physik der Teilchenbeschleuniger und Synchrotronstrahlungsquellen*, B.G. Teubner, Stuttgart, 1992
- [2] <http://www.slac.stanford.edu/>
- [3] TESLA TECHNICAL DESIGN REPORT, DESY 2001-011, ECFA, 2001-209, hep-ph/0106315
- [4] M. DOHLUS, private communication, dohlus@mail.desy.de, DESY 2001
- [5] W. BRUNS, <http://www.gdfidl.de>
- [6] LABVIEW, <http://www.labview.com>
- [7] <http://www.fz-rossendorf.de/ELBE/de>
- [8] J. G. WEISEND II, R. BANDELMANN, D. BARNI, M. BONEZZI, G. GRYGIEL, R. LANGE, C. PAGANI, B. PETERSEN, P. PIERINI, D. SELLMANN, S. WOLFF, *The TESLA Test Facility (TTF) Cryomodule: A Summary of Work to Date*, Proc. CEC/ICMC 1999, Montreal 1999, published in *Advances in Cryogenic Engineering*, 5A (2000) 825
- [9] C. PAGANI, D. BARNI, M. BONEZZI, J. G. WEISEND II, *Further improvements of the TESLA Test Facility (TTF) Cryostat in view of the TESLA Collider*, Proc. CEC/ICMC 1999, Montreal 1999, published in *Advances in Cryogenic Engineering* 45A (2000) 939
- [10] A. NOVOKHATSKI, M. TIMM AND T. WEILAND, *Single Bunch Energy Spread in the TESLA Cryomodule*, DESY TESLA-93-11, 1993
- [11] A. NOVOKHATSKI, M. TIMM AND T. WEILAND, *Transition Dynamics of the Wake Fields of Ultra Short Bunches*, DESY TESLA-00-03, 2000
- [12] A. JOESTINGMEIER, M. DOHLUS, M. WENDT, C. CRAMER, *theoretical and Practical Investigations Concerning the Design of a HOM Broad-band Absorber for TESLA*, DESY TESLA-00-10, 2000

- [13] A. JOESTINGMEIER, M. DOHLUS, C. CRAMER, *Photon diffusion model for TTF-2*. DESY TESLA-00-11, 2000
- [14] M. DOHLUS, H. P. WEDEKIND AND K. ZAPFE, *Wakefield Induced Losses in the Manual Valves of the TESLA Cryomodule*, DESY TESLA-00-39, 2000
- [15] R. BRINKMANN, M. DOHLUS, D. TRINES, A. NOVOKHATSKI, M. TIMM, T. WEILAN D, P. HUWLSMANN, C. RIECK, K. SCHARNBERG, P. SCHMUESER, *THz Wakefields and Their Effect on the Superconducting Cavities in TESLA*, Proc. 7-th EPAC, Vienna 2000, p 2028
- [16] R. LORENZ, *Strahllage-Monitore fuer Lineare Collider*, DISSERTATION, Berlin 1995
- [17] CERN ACCELERATING SCHOOL, *RF ENGINEERING FOR PARTICLE ACCELERATORS*, CERN 92-03, 11 June 1992 Vol. II, p. 319
- [18] A. LIAPINE. *Beam Position Monitor for the TESLA Energy spectrometer*, EPAC 2002, Paris, 2002
- [19] J. D. JACKSON, *Classical Electrodynamics*, (John Wiley and Sons, Inc. 1962), Ch. 11, pp. 555
- [20] D. P. MCGINNIS, *The Design of Beam Pickup and Kickers*, Fermi National Laboratory
- [21] MILTON ABRAMOWITZ AND IRENA STEGUN, "HANDBOOK OF MATHEMATICAL FUNCTIONS", New York
- [22] R. E. SCHAFER, *Beam Position Monitoring*, in AIP Conference Proceedings on Accelerator Instrumentation (AIP, Upton, NY 1989) pp. 26-55
- [23] W. H. HAYT, JR. AND J. E. KEMMERLY, *Engineering Circuit Analysis*, (McGraw-Hill, 1978), Ch. 19, pp. 664-668
- [24] H. MEINKE, F. GRUNDLACH, *Taschenbuch der Hochfrequenztechnik*, Springer (1968) 309, 281
- [25] CERN ACCELERATOR SCHOOL. *Fifth General Accelerator Physics Course*. Vol. II, p. 571. 1994, GENEVA
- [26] J. CUPERUS *MONITORING OF PARTICLE BEAMS AT HIGH FREQUENCIES*, CERN - Geneva

- [27] H. HENKE, henke@tetibm1.ee.tu-berlin.de, *TU-Berlin*, August 2001
- [28] I. S. GRADSHTEYN, I. M. RYZHIK, "TABLE OF INTEGRALS SERIES AND PRODUCTS", New York and London, 1965
- [29] R. LORENZ, *Cavity Beam Position Monitors*, Beam Instrumentation Workshop'98, SLAC, Stanford, 1998
www.slac.stanford.edu/pubs/confproc/biw98/lorenz1.pdf
- [30] W.W. HANSEN, *On the Resonant Frequency of Closed Concentric Lines*, Journal of Applied Physics, Vol.10 (1939) 38
- [31] M. WENDT, C. MAGNE, *BPMs for the Tesla Accelerator Complex*. DESY, 2000
- [32] P. EVTUSHENKO, A. BUECHNER, H. BUETTIG, P MICHEL, R.SCHURIG, B. WUSTMANN, Stripline Beam Position Monitor for ELBE, FZR, Germany K. Jordan, TJNAF, USA
- [33] [HTTP://WWW-JLC.KEK.JP/](http://WWW-JLC.KEK.JP/)
- [34] V. SARGSYAN, *Cross-Talk Problem in Pill-Box Cavity*, TESLA 2003-01, DESY, January 2003
- [35] V. SARGSYAN AND A. LIAPINE, *Beam Position Monitors (in preparation)*.
- [36] ROGER F. HARRINGTON, *Time-Harmonic Electromagnetic Fields*, New York-Toronto-London 1961.
- [37] N. MARRCUVITZ, *Waveguide Handbook*, Radiation Laboratory Series, 10. 1951.
- [38] O.S. MILOVANOV, N.P. SOBENIN, *Ultrahigh Frequency Technics*, Atomizdat, Moscow 1951 (in Russian).
- [39] EDWARD L. GINZTON, W. W. HANSEN, *Microwave Measurements*, NY 1957
- [40] DR. RER. NAT. HABIL. H. HÄNSEL, *GRUNDZÜGE DER FEHLER-RECHNUNG*, DVW, Berlin 1965
- [41] A.LIAPINE, V.SARGSYAN. *Survey of RF Receiving Techniques*, TET-Note TU-Berlin, Feb-2002

- [42] ASAD A. ABIDI *Direct-Conversion Radio Transceivers for Digital Communications*,
- [43] R. SCHROEDER, private communication, schroeder@tetibm1.ee.tu-berlin.de, *TU-Berlin, EN2*, Berlin 2002